AD-A273 744

|||||||||||||

∂

S DTIC
ELECTE
DEC 16 1993
A

OFF-DESIGN PERFORMANCE OF CRENULATED
BLADES IN A LINEAR COMPRESSOR CASCADE

THESIS

Michael J. Costello, Captain, USAF

AFIT/GAE/ENY/93D-9

93-30480
||||||||||||||||

93 12 15096

Best Available Copy

OFF-DESIGN PERFORMANCE OF CRENULATED

BLADES IN A LINEAR COMPRESSOR CASCADE

THESIS

Presented to the Faculty of the Graduate School of Engineering

of the Air Force Institute of Technology

Air University

In Partial Fulfillment of the

Requirements for the Degree of

Master of Science in Aeronautical Engineering

MICHAEL J. COSTELLO

Captain, USAF

December 1993

Accesion For	
NTIS CRA&I	☑
DTIC TAB	☐
Unannounced	☐
Justification	
By	
Distribution /	
Availability Codes	
Dist	Avail and / or Special
A-1	

Approved for public release; distribution unlimited

Acknowledgments

The completion of this project would not have been possible without the assistance that I have received from others. Although there is not enough space on a page to include all of the people who offered their assistance, I would like to acknowledge those who were most directly involved. I would like to thank my advisor, Dr William C. Elrod, for the countless contributions that he made to this study. Dr Elrod's advice helped me overcome many obstacles during the course of this research. I would also like to thank Dr Paul I. King and Dr Milton E. Franke for their contributions. As members of the thesis committee, they too provided advice which proved to be invaluable.

The AFIT Model Shop was instrumental in the completion of this project. I would like to thank Mr John Brohas for his skillful dedication to the fabrication of our newly-designed test section. I would also like to thank Mr David Driscoll, Mr Timothy Hancock, and Mr Ronald Ruley. Their response to my panic-stricken requests for new compressor blades or a new pressure rake was immediate and sincerely appreciated.

The AFIT lab technicians also contributed in many ways to this project. I would like to thank Mr Jay Anderson for his efforts to help develop the software which was essential to the completion of this project. I also owe thanks to Mr Daniel Rioux, Mr Andrew Pitts, and Mr Mark Derriso. They ensured that I had plenty of air, a table full of tools and instruments, and that I knew how to use them.

Finally, I would like to thank my research partner, Capt William L. Spacy II. Without his teamwork, there would be no results. Capt Spacy overhauled much of the instrumentation hardware and helped take hundreds of hours of around-the-clock data to complete this project. Also, I would like to acknowledge Capt Spacy as co-author of Chapter IV, and Appendices A and C of this document.

<div align="right">Michael J. Costello</div>

Table of Contents

List of Figures

List of Tables

List of Symbols

Symbol

AFIT	Air Force Institute of Technology
AR	blade aspect ratio
ASME	American Society of Mechanical Engineers
AVDR	axial velocity density ratio
DF	diffusion factor
DF_{st}	diffusion factor for straight trailing edge blade
IHPTET	Integrated High Performance Turbine Engine Technology Initiative
SSE	sum squared error over hot-film probe calibration range
TE	trailing edge
WVD	wake velocity deficit (%)
WVD_{st}	wake velocity deficit for straight trailing edge blade (%)

A	a general quantity, also hot-film sensor calibration constant
$\tilde{A}$	mass averaged general quantity
b	temperature loading factor
B	hot-film sensor calibration constant
c	blade chord (cm)
C	hot-film sensor calibration constant
C_p	static pressure coefficient
d_s	hot-film sensor diameter (m)
i	incidence angle (deg)
i*	nominal incidence angle (deg)
j	index for individual data point in the sample set
k	cooling ratio of hot-film sensor

l^+	spanwise maximum of measurement plane (cm)
l^-	spanwise minimum of measurement plane (cm)
L	number of samples for each data point
n	number of data points in the sample set
Nu	Nusselt number
p	static pressure on blade surface, also static pressure at cascade exit (Pa)
p_1	static pressure at cascade inlet (Pa)
P_{o1}	total pressure at cascade inlet (Pa)
P_{o2}	total pressure at cascade exit (Pa)
P_{tnk}	stilling chamber static pressure (Pa)
PR_{PS}	blade pressure surface pressure ratio
PR_{SS}	blade suction surface pressure ratio
R	gas constant (J/kg·K)
Re	Reynolds number
s	blade spacing (cm)
s^+	pitchwise maximum of measurement plane (cm)
s^-	pitchwise minimum of measurement plane (cm)
T	static temperature of fluid about hot-film sensor (K)
T_1	cascade inlet static temperature (K)
T_r	Eckert reference temperature (K)
T_{tnk}	stilling chamber total temperature (K)
Tu	outlet turbulence intensity (%)
V	actual fluid velocity about hot-film sensor (m/s)
V_1	velocity at cascade inlet (m/s)
$\bar{V}_2$	mass averaged velocity at cascade exit (m/s)
V_{eff}	effective velocity (m/s)

V_{x_1}	axial velocity at cascade inlet (m/s)
V_{x_2}	axial velocity at cascade exit (m/s)
V_∞	freestream velocity at cascade exit (m/s)
x	axial coordinate (cm)
y	pitchwise coordinate (cm)
z	spanwise coordinate (cm)

Greek Symbol

α	angle between sensor axis and actual fluid velocity (deg)
α_1	air inlet angle = throat angle (deg)
α'_1	blade inlet angle (deg)
α_2	air outlet angle (deg)
α'_2	blades outlet angle (deg)
δ	deviation (deg)
δ_{st}	deviation for straight trailing edge blade (deg)
Δ	difference between crenulated blade and straight trailing edge blade
ε	deflection (deg), also net error due to component accuracies
ε_{st}	deflection for straight trailing edge blade (deg)
ε^*	nominal deflection (deg)
ϕ_1	angle between tangent and chord of circular arc at leading edge (deg)
ϕ_2	angle between tangent and chord of circular arc at trailing edge (deg)
γ	ratio of specific heats
μ	viscosity (N·s/m^2)
$\overline{v}_x$	mean x-component of velocity fluctuations (m/s)
$\overline{v}_y$	mean y-component of velocity fluctuations (m/s)
θ	blade camber angle (deg)

ρ_1	density at cascade inlet (kg/m^3)
ρ_2	density at cascade exit (kg/m^3)
σ^2	outlet velocity variance (%)
$\tilde{\sigma}^2$	mass weighted outlet velocity variance (%)
$\tilde{\sigma}^2{}_{st}$	mass weighted outlet velocity variance for straight trailing edge blade (%)
ϖ	total pressure loss coefficient
ζ	stagger angle (deg)

AFIT/GAE/ENY/93D-9

Abstract

The effects of using compressor blades with a crenulated (notched) trailing edge in a low aspect ratio ($AR = 1$) linear compressor cascade at four incidence angles (-1.08 deg, +4.49 deg, +9.32 deg, and +12.44 deg) were investigated. Blade performance and wake mixing characteristics for crenulated blades were compared with similar data for blades with a straight trailing edge. A seven-bladed cascade was operated with a flow Mach number of 0.4 and a blade chord Reynolds number of 4.1 $(10)^5$. The diffusion factor ranged from 0.22 to 0.42 and strong three-dimensional flow effects were present. Total pressure losses were measured with a total pressure rake. Velocities and flow angles were measured using hot-film anemometry. Crenulated blades were found to enhance wake mixing from 20 to 50 percent depending on blade loading and downstream location. Crenulated blades were also found to reduce flow deflection by 1.9 deg at the lowest incidence and by 3.7 deg at the highest incidence. At the highest blade loading, crenulations were found to reduce total pressure losses by 20 percent and inhibit large scale flow degradation and vortex breakdown. At mild blade loadings, negligible differences in losses were observed.

OFF-DESIGN PERFORMANCE OF CRENULATED

BLADES IN A LINEAR COMPRESSOR CASCADE

I. Introduction

Background

During the past century, the gas turbine engine has evolved from an inefficient machine of little practicality to become a very reliable, efficient means of converting energy which has many industrial and aeronautical applications. As the evolution of the gas turbine continues, improving gas turbine efficiency continues to be a worthy goal of aircraft propulsion research. For example, the Integrated High Performance Turbine Engine Technology Initiative (IHPTET, a cooperative effort between the Department of Defense, the National Aeronautics and Space Administration, and the aeropropulsion industry) is striving to double the aircraft turbine engine propulsion capability by the year 2000. To achieve its overall goal, this initiative relies on the cumulative success of numerous research efforts which are focused on individual gas turbine engine components.

Improved efficiency of gas turbine engines corresponds to increased aircraft engine capability (thrust), fuel savings, or weight savings, depending on the priorities for the specific application. The efficiency of a gas turbine is directly related to the efficiency of each of its components. Gas turbine engines have three primary components: a compressor, a combustor, and a turbine. The primary function of each component (respectively) is to compress, heat, and expand the flow. While satisfying its primary function, each component adversely imparts losses to the flow which degrade the overall performance of the engine. Aerodynamic losses imparted to the flow in the compressor is the focus of this investigation.

Axial flow compressors are commonly used in aircraft engines. In general, viscous effects are a major source of losses in axial compressors. These losses are largely caused by the boundary layers that develop on compressor blades.

Problem Statement

Boundary layers develop on the pressure surface and the suction surface of compressor blades and merge at the trailing edges to create wakes which trail downstream of the blades. These wakes are characterized by a defect in velocity and total pressure. A schematic of the development of blade wakes is shown in Figure 1. The mixing of these wakes is a source of flow losses. Wennerstrom (1982) proposed that compressor blades with crenulated trailing edges may enhance (i.e., accelerate) the wake mixing process--which would effectively reduce the required length and weight of an axial flow compressor by one or more rows of blades. The introduction of crenulations to a blade trailing edge serves to generate vortices which trail downstream of the blade as shown in Figure 2. It is these crenulation induced vortices which are the physical mechanism which is thought to enhance the mixing process. With this improvement, it is thought that a corresponding improvement in gas turbine efficiency may be realized.

Summary of Previous Research

Wennerstrom's proposal was investigated by Veesart et al. (1990), and by DeCook et al. (1993). Both investigators found (among other findings) that the crenulated blades did indeed cause enhanced wake mixing and lower wake losses than the same blades without crenulations. These investigations were performed at a single incidence angle using a linear compressor cascade. The linear compressor cascade is a simplified model of an axial flow compressor blade row, and is used to conduct experimental aerodynamic research. This simplification permits relatively inexpensive research to yield practical

results which can be extrapolated and applied to the more complex flow regimes in axial flow compressors.

Motivation

It is common for axial flow compressors in aircraft engines to spend a significant amount of operating time at off-design rotational speeds. Variations in incidence angle in a cascade can be thought to model variations in rotational speed and /or axial velocity in an axial flow compressor. Therefore, cascade research which investigates the effect of crenulated blades at various incidence angles could supply valuable information concerning the overall merit of using crenulated compressor blades in aircraft engines.

Objective and Scope

The objective of the experiment, relative to axial flow compressor design, was to determine the aerodynamic benefits and shortcomings of using blades with a crenulated trailing edge in comparison to using blades with a straight trailing edge. The study is particularly focused on modeling the last row of stator blades where secondary flow effects would be significant. With this perspective, a linear cascade experiment was conducted at four incidence angles (-1.08 deg, +4.49 deg, +9.32 deg, and +12.44 deg). Two blade configurations were investigated: one with a crenulated trailing edge, and the other with a straight trailing edge.

II. Theory

General Description of a Cascade

A cascade is a row of identical blades which is used to change the direction and pressure of a flowing gas. Cascades have been widely used to model the flow environment in axial flow compressors. A *linear* cascade (as opposed to an annular cascade) is a cascade which has its blades arranged as if they were mounted on a hub with an infinite radius of curvature. Consequently, the edges of the blades in a linear cascade are parallel to each other.

A cascade is typically defined by specifying the blade geometry, the geometric arrangement of the blades, and the flow condition. The specifications which are used to define a particular linear cascade are identified in Figure 3. The blade geometry is specified by the blade chord (c), the blade camber angle (θ), the point of maximum camber (a, typically measured along the chord and normalized by chord length), the blade thickness distribution, and the blade aspect ratio (AR). The aspect ratio is defined as the blade span normalized by the blade chord. The arrangement of the blades is specified by the blade spacing (s), the stagger angle (ζ), the blade inlet angle (α'_1), and the blade outlet angle (α'_2). The flow condition of the cascade is specified by the air inlet angle (α_1) and inlet velocity (V_1), and the air outlet angle (α_2) and outlet velocity (V_2). Various other cascade descriptors can be derived from these basic parameters. Three descriptors which are typically used are the deviation angle (δ), the incidence angle (i), and the deflection (ϵ). As shown in Figure 3, the deviation angle is simply the difference between the air outlet angle and the blade outlet angle. Likewise, the incidence angle is the difference between the air inlet angle and the blade inlet angle; and the deflection is the difference between the air outlet angle and the air inlet angle.

Ideal Cascade Flow

Ideally, a cascade would have an infinite number of blades. An infinite number of blades would eliminate the viscous effects of the cascade endwalls on the flow. These effects are undesirable because there are no analogous effects in an axial flow compressor.

In many cascade experiments it would also be considered ideal to have blades of infinite span. Blades of infinite span would eliminate the viscous effects of the cascade sidewalls on the flow. The elimination of sidewall effects (given uniform flow conditions at the flow source) would result in two-dimensional flow. Two-dimensional flow as specified by Erwin and Emery (1950) has the following characteristics:

1. Equal pressures, velocities, and directions exist at different spanwise locations.

2. The static pressure rise across the cascade equals the value associated with the measured turning angle and wake.

3. No regions of low energy flow, other than blade wakes exist. The blade wakes are constant in the spanwise direction.

4. The measured force on the blades equals that associated with the measured momentum and pressure change across the cascade.

5. The various performance values do not change with aspect ratio, number of blades, or other physical factors of the tunnel configuration.

Cascade flow which is two-dimensional is thought to have the broadest application to general axial flow compressor design.

Although purely two-dimensional flow affords considerable simplification in interpreting cascade results, it is often impractical to achieve. In practice, a finite amount of three-dimensionality in cascade flow may be desirable. In some cases, a cascade with three-dimensional effects may be useful in modeling a specific flow condition in a compressor. For example, the flow through the last row of stator blades in a compressor

may have strong three-dimensional effects. The characteristically low aspect ratio of these blades allow the viscous effects at the compressor casing and hub to significantly degrade the two-dimensionality of the flow. These effects can be particularly significant at high incidence angles. The blades used in this study were low aspect ratio blades ($AR = 1$) which are representative of those which are typically used as the last row of stator blades in an axial flow compressor. Achieving two-dimensional flow was not the intent of this study. However, the two-dimensional flow condition does serve as a point of comparison to qualitatively assess the degree of secondary flow present in the cascade.

Quantification of Cascade Performance

Several parameters can be used to quantify the performance of linear cascades. These parameters serve two purposes. They, 1) provide a basis for evaluating the validity of the cascade as a model, and 2) provide a basis for evaluating the aerodynamic performance of the particular concept being modeled. In this study, the concept that was considered was the effect of using crenulated blades at various incidence angles where three-dimensional flow was present. Since some of the parameters are expressed with respect to a coordinate system, the cascade coordinate system that was used in this study is defined as shown in Figure 4.

Evaluation of the Cascade as a Model. The validity of the cascade as a model can be evaluated by determining the periodicity and the axial velocity density ratio ($AVDR$) of the cascade. A slightly modified form of the $AVDR$ as given by DeCook (1993) is defined as

$$AVDR = \frac{\int_{r^-}^{r^+} \left(\rho_2 V_{x_2}\right)_{midspan} dy}{\int_{r^-}^{r^+} \left(\rho_1 V_{x_1}\right)_{midspan} dy} \qquad (1)$$

6

where $s^+ - s^-$ is one blade spacing. If a discrete number of data points are sampled in the y-z plane (reference Figure 4) with equal spacing in the y-direction such that the spacing between the data points is sufficiently smaller than the sample range, the $AVDR$ can be approximated numerically by

$$AVDR = \frac{\sum_{j=1}^{n} (\rho_2 V_{x_2})_j}{\sum_{j=1}^{n} (\rho_1 V_{x_1})_j} \qquad (2)$$

where n is the number of samples taken at the midspan location. The $AVDR$ is an indication of the two-dimensionality of the flow. If a cascade has no spanwise gradients of mass flux, the $AVDR = 1.0$ and the flow is two-dimensional. An $AVDR > 1.0$ indicates flow contraction and a subsequent increase of the midspan mass flux through the cascade. Results from cascades with non-unity $AVDR$ are correlated with two-dimensional flow results by the relationships presented by Gostelow (1984). According to Gostelow (1984), caution must be exercised when using the $AVDR$ to indicate the two-dimensionality of the flow because the $AVDR$ represents a midspan average which may not accurately reflect the effect of localized three-dimensional flow which may develop in the cascade. Examples of such flows are passage vortices, corner vortices, and concentrated shed vortices which in some cases develop on the suction surface of low aspect ratio cascade blades. A schematic of three-dimensional flow phenomena which may occur in a cascade are shown in Figure 5. Tang et al. (1991), and Kang and Hirsch (1991) have investigated the three-dimensional flow in linear cascades and provide many details on its structure and characteristics.

Periodicity describes the pitchwise static pressure distributions at the cascade inlet and exit. If the variation of static pressure with respect to pitchwise distance from the

7

center blade is periodic (i.e., cyclic) then periodicity is said to be achieved. According to Gostelow (1984), periodicity is essential for a cascade to be considered a valid model.

Evaluation of Aerodynamic Concepts using the Cascade. With the periodicity and AVDR established, the aerodynamic performance of a cascade can be determined. Common indicators of cascade performance are the static pressure coefficient (C_p), the total pressure loss coefficient (ϖ), and the flow turning angle or deflection. Since this investigation focuses in part on the wakes generated by the cascade, it is also relevant to quantify the character of the flow downstream of the cascade. This can be accomplished with (in addition to ϖ) the wake velocity deficit (WVD) and the outlet velocity variance (σ^2).

The blade static pressure coefficient is defined as

$$C_p \equiv \frac{p - p_1}{\frac{1}{2}\rho_1 V_1^2} \tag{3}$$

where p is the static pressure on the blade surface. C_p is useful in quantifying blade performance because it can be integrated over the blade surface to find the net force of the fluid acting on the blade. The net force on the blade is equal in magnitude and opposite in direction to the net force on the fluid. Through conservation of momentum and a force balance on the blade, it follows that the net force on the fluid indicates the amount of flow deflection caused by the blade. Since compressor blades are designed to turn the flow, C_p profiles for blades in different cascade configurations provide a comparative indication of blade performance.

The local total pressure loss coefficient is defined as

$$\varpi = \frac{P_{01} - P_{02}}{\frac{1}{2}\rho_1 V_1^2} \qquad (4)$$

Determination of ϖ provides an indication of the energy lost through the cascade due to viscous dissipation. A value of zero with no work addition would indicate isentropic flow through the cascade. The total pressure loss coefficient can be useful in defining the incidence angle at which a particular cascade is stalled. For example, Dixon (1978) suggests that the incidence at which stall occurs is that which corresponds to twice the minimum ϖ. A mass averaging scheme (Equation (6)) was used to combine the individual values of ϖ at each location in the cascade exit measurement plane to arrive at a single value of ϖ which was representative of the entire exit measurement plane. The mass averaging scheme was implemented because the flow at the cascade exit is characterized by nonuniform mass flow due to the blade wakes and three-dimensional flow.

Gostelow (1984) states that for steady, incompressible flow the non-dimensional pressure rise through a two-dimensional cascade may be expressed as (referring to Figure 2)

$$C_p = 1 - \frac{\cos^2 \alpha_1}{\cos^2 \alpha_2} - \varpi \qquad (5)$$

This expression for C_p provides a means of estimating flow deflection ($\alpha_1 - \alpha_2$) through a linear cascade from pressure measurements at the exit, provided the inlet conditions are known. In this case, C_p is determined by applying Equation (3) with p being measured just downstream of the blade trailing edge.

The wake velocity deficit and the outlet velocity variance are defined with the use of average properties. Since the wake region is a region of varying mass flow, a mass

averaging scheme was used in the wake region. The mass average of some general quantity A, is defined as

$$\bar{A} = \frac{\int_{z^-}^{z^+}\int_{y^-}^{y^+} A\,\rho_2 V_{x_2}\,dzdy}{\int_{z^-}^{z^+}\int_{y^-}^{y^+}\rho_2 V_{x_2}\,dzdy} \tag{6}$$

If a discrete number of data points are sampled in the y-z plane (reference Figure 4) with equal spacing in the y-direction and equal spacing in the z-direction such that the spacing between the data points is sufficiently smaller than the sample range, the mass average of A can be approximated numerically by

$$\bar{A} = \frac{\sum_{j=1}^{n}\rho_{2_j} V_{x_{2_j}} A_j}{\sum_{j=1}^{n}\rho_{2_j} V_{x_{2_j}}} \tag{7}$$

where n is the number of samples in the measurement plane.

The wake velocity deficit is defined as

$$WVD = 1 - \frac{\bar{V}_2}{V_\infty} \tag{8}$$

The value of the wake velocity deficit would be expected to be nearly 0 immediately downstream of a cascade which has blades with a sharp trailing edge. This is because a wake trailing a sharp edge would have a very narrow width and account for a relatively small portion of the total mass flow through the cascade. For incompressible flow over an airfoil with zero lift, it follows from White (1991) that as the wake develops downstream of the airfoil, the wake velocity deficit should initially increase to a maximum and then

10

decay to a value approaching 0 at a location far downstream of the airfoil. However, White (1991) further suggests that the flow behind a cascade of cambered blades is likely to be complicated with shed vortices and therefore the above trend can be thought of as a time averaged trend.

The outlet velocity variance is the square of the standard deviation of the exit velocity distribution. It is normalized by the square of the mean exit velocity and is defined as

$$\sigma^2 \equiv \frac{1}{\overline{V_2}^2} \cdot \frac{\sum_{j=1}^{n}(V_{2_j} - \overline{V_2})^2}{(n-1)} \tag{9}$$

where $\overline{V_2}^2$ is the square of the arithmetic mean exit velocity. It should be noted, for the sake of being rigorous, that the *sample* variance was used in the outlet velocity variance definition as opposed to the *population* variance. The sample variance was used because of the finite discretization of the measurement plane as discussed in Chapter IV. If the population variance were used, the term $(n-1)$ would be replaced by n. Because $n = 1474$ data points in this study and $1474 \gg 1$, the difference between the sample variance and the population variance is inconsequential to the results. Due to the variations of mass flow in the wake region discussed previously, it is appropriate to calculate a mass weighted variance. The mass weighted outlet velocity variance is defined as

$$\tilde{\sigma}^2 \equiv \frac{1}{\overline{V_2}^2} \cdot \frac{\sum_{j=1}^{n} \rho_{2_j} V_{x_{2_j}} (V_{2_j} - \overline{V_2})^2}{\overline{\rho_2 V_{x_2}} (n-1)} \tag{10}$$

where the expression $\overline{\rho_2 V_{x_2}}$ is the arithmetic mean mass flux in the axial direction. The variance can not be evaluated at a single data point; it applies to a set of data points. Consequently, the mass weighted exit velocity variance is not a mass *averaged* quantity

11

per the definition previously given (Equation 6). However, the mass weighted outlet velocity variance was converted into an expression which takes a mass averaged form. This conversion process is shown by the following manipulations.

In the denominator of the mass weighted outlet velocity variance expression, the mean mass flux term is expanded to take the form of a sum,

$$\tilde{\sigma}^2 = \frac{1}{\overline{V_2}^2} \cdot \frac{\sum_{j=1}^{n} \rho_{2_j} V_{x_{2_j}} (V_{2_j} - \overline{V_2})^2}{\left(\dfrac{\sum_{j=1}^{n} \rho_{2_j} V_{x_{2_j}}}{n} \right)(n-1)} \tag{11}$$

$$\tilde{\sigma}^2 = \frac{n}{(n-1)} \cdot \frac{1}{\overline{V_2}^2} \cdot \frac{\sum_{j=1}^{n} \rho_{2_j} V_{x_{2_j}} (V_{2_j} - \overline{V_2})^2}{\sum_{j=1}^{n} \rho_{2_j} V_{x_{2_j}}} \tag{12}$$

Introducing the squared mean exit velocity term into the sum in the numerator,

$$\tilde{\sigma}^2 = \frac{n}{(n-1)} \cdot \frac{\sum_{j=1}^{n} \rho_{2_j} V_{x_{2_j}} \left(\dfrac{V_{2_j}}{\overline{V_2}} - 1 \right)^2}{\sum_{j=1}^{n} \rho_{2_j} V_{x_{2_j}}} \tag{13}$$

This expression is now recognized as,

$$\tilde{\sigma}^2 = \frac{n}{(n-1)} \cdot \text{mass average of} \left(\frac{V_2}{\overline{V_2}} - 1 \right)^2 \tag{14}$$

12

III. Experimental Apparatus

The experimental apparatus consists of five major components. These components are the air supply system, the diffuser/stilling chamber, the throat, the cascade test section, and the data acquisition system. A description of each component is provided in this chapter.

Air Supply System

A schematic of the air supply system and diffuser/stilling chamber is shown in Figure 6. The air supply system consists of a 30 kW centrifugal blower which delivers air to the test section at approximately 1.6 kg/s which results in a flow Mach number of approximately 0.4 in the cascade test section. The blower is configured so that it can intake outdoor air, laboratory air, or a combination of outdoor and laboratory air. This option is useful for controlling the total temperature of the flow through the cascade. The air is electrostatically filtered before entering the diffuser.

Diffuser/Stilling Chamber

The air from the blower is diffused to approximately 3 m/s in the stilling chamber. The stilling chamber is cylindrical with an internal diameter of approximately 1.1 m. It has provisions for conditioning and straightening the flow prior to the test section entrance, and contains a styrofoam center body plug which is covered with foam rubber. The plug provides a gradual change in cross-sectional area for diffusion of the flow; it also obstructs the acoustic path between the blower and the test section. A 40 mesh wire screen, a cloth filter, and a 10 cm thick honeycomb grid provide the final flow conditioning and straightening before the flow exits the stilling chamber through a rectangular ASME long-radius bellmouth nozzle. The nozzle throat has a 5.0 cm by 20.3 cm cross-section. A

more detailed description of the air supply system and diffuser/stilling chamber is given by Allison (1982).

Throat and Cascade Test Section

A schematic of the throat and cascade test section is shown in Figure 7. As shown in Figure 7, the throat has provisions for endwall boundary layer removal. Suction was applied to the endwall suction slots for all cascade testing in this study. The test section holds seven blades. The profile of the blades used in this study is shown in Figure 8; their surface coordinates and mean camber line are listed in Table 1. The details of the blade geometry, including the determination of the blade camber angle and the inlet and exit angles, are included in Appendix A. Although the blade profile was fixed throughout this study, the trailing edge of the blades differed depending on whether the blades were crenulated or not crenulated. The planform of each blade configuration tested is shown in Figure 9. During a single test run, all seven blades were either crenulated or not crenulated. As can be seen from Figure 9, the presence of the crenulations caused the blade planform to be reduced by approximately 14 percent. The test section interfaces directly with any one of four interchangeable throat sections. Each throat section causes the cascade to see a unique incidence angle. This method of varying the incidence angle allows the stagger angle to remain fixed throughout the testing. The throat angles and corresponding incidence angles are listed in Table 2. In this study, it was assumed that the velocity in the throat was parallel to the throat endwalls and therefore the throat angles were equal to the air inlet angles (α_1). As can be seen from Figure 7, the throat/test section interface requires that the cascade test section accommodate various inlet areas. This was accomplished with the adjustable endpieces in the cascade test section. The endpieces were adjusted by using a shim of the appropriate thickness for each incidence angle. Depending on the incidence angle tested, the spacing between the outer-most blade

and the cascade endwall varied from 1.1 cm to 2.9 cm. This variation in endwall spacing can be expected to affect the performance of the outer blades. However Erwin and Emery (1950) found that variations in endwall spacing had a negligible effect on the performance of the center blade. Since this study focused on the center blade, the variations in endwall spacing were determined to be acceptable.

The center blade of each cascade configuration was fabricated with static pressure ports on its pressure surface and suction surface to allow a midspan blade surface static pressure distribution to be obtained. The position of these ports along the blade chord are listed in Table 3. It should be noted that the crenulated blades have the furthest downstream pressure port omitted due to interference with the crenulations. The cascade specifications as defined in Chapter II are listed in Tables 2 and 4.

Table 1. Blade Surface Coordinates and Mean Camber Line

Suction Surface x (cm)	Suction Surface y (cm)	Pressure Surface x (cm)	Pressure Surface y (cm)	Mean Camber y (cm)
5.001	0.000	5.001	0.000	0.000
4.902	0.020	4.901	0.009	0.015
4.703	0.061	4.699	0.028	0.044
4.404	0.119	4.497	0.046	0.083
4.257	0.148	4.245	0.069	0.108
4.010	0.202	3.992	0.092	0.147
3.612	0.285	3.590	0.132	0.208
3.213	0.359	3.189	0.169	0.264
2.811	0.420	2.790	0.198	0.309
2.404	0.456	2.397	0.213	0.335
1.997	0.460	2.004	0.210	0.335
1.744	0.448	1.757	0.201	0.325
1.491	0.427	1.510	0.189	0.308
1.238	0.396	1.263	0.172	0.284
0.986	0.356	1.015	0.150	0.253
0.734	0.304	0.766	0.122	0.213
0.483	0.239	0.517	0.087	0.163
0.383	0.209	0.417	0.071	0.140
0.283	0.174	0.317	0.053	0.114
0.184	0.134	0.216	0.034	0.084
0.086	0.084	0.114	0.013	0.049
0.038	0.053	0.062	0.002	0.028
0.016	0.033	0.034	-0.002	0.015
0.000	0.011	0.010	-0.004	0.004
0.000	0.000	0.000	0.000	0.000

Note: For Table 1, x refers to distance from leading edge along the blade chord and y refers to perpendicular distance from blade chord

Table 2. Throat Angles and Corresponding Incidence Angles

α_1 (deg)	i (deg)
25.43	-1.08
31.00	+4.49
35.83	+9.32
38.95	+12.44

Table 3. Location of Blade Static Pressure Ports

Location in Fraction of Chord	
Suction Surface	Pressure Surface
0.045	0.070
0.095	0.120
0.169	0.195
0.245	0.270
0.295	0.320
0.345	0.370
0.395	0.420
0.445	0.470
0.495	0.520
0.545	0.620
0.645	0.670
0.695	0.720

Table 4. Cascade Specifications

Specification	Symbol	Value
Blade Chord Length	c	5.0 cm
Blade Camber Angle	θ	30.51 deg
Blade Inlet Angle	α'_1	26.51 deg
Blade Outlet Angle	α'_2	-4.00 deg
Point of Maximum Camber	a	0.5 chord
Blade Spacing	s	3.4 cm
Stagger Angle	ζ	7.50 deg
Air Inlet Angle	α_1	see Table 2
Inlet Velocity	V_1	137-146 m/s
Air Outlet Angle	α_2	see Table 6
Outlet Velocity	V_2	107-122 m/s
Deviation Angle	δ	see Table 8
Incidence Angle	i	see Table 2
Deflection	ε	see Table 6

18

Data Acquisition System

The elements of the AFIT Cascade Test Facility Digital Data Acquisition System are depicted in Figure 10. As can be seen in the figure, the acquisition system consists of a central computer and four subsystems. The four subsystems can be described functionally as (1) the pressure measurement subsystem, (2) the velocity and temperature measurement subsystem, (3) the temperature measurement subsystem, and (4) the traverse control subsystem. A detailed equipment listing is presented in Appendix B.

Central Computer. The central computer for the data acquisition system is a Zenith Z-248 computer. The computer is equipped with a math coprocessor to speed numerical computations. The software which commands the acquisition process is written in MS-QuickBasic 4.5. The software consists of several multi-module programs and provides automation of both data acquisition and data reduction.

Pressure Measurement Subsystem. The pressure measurement subsystem consists of a Pressure Systems, Inc. Model 8400 Pressure Scanner, three 32-port transducer blocks, a total pressure rake, and a CEC Model 2500 Digital Barometer. The pressure scanner was used to measure the cascade inlet total and static pressures, the blade surface static pressures, and the cascade exit total and static pressures. The digital barometer was used to measure the laboratory ambient pressure.

As configured in this study, the pressure scanner scanned the output from the transducer blocks at a rate of 20 kHz. For one data point, it sampled each of the 96 ports 11 times and calculated the arithmetic mean of the 11 values which resulted in a total sample time of 0.053 seconds. The pressure scanner has an internal certified standard transducer which was used for calibration at the beginning of each test run. The standard transducer is supported by an internal heater to minimize the influence of ambient temperature fluctuations.

The transducer blocks provided 96 transducers from which pressure was measured. Each transducer block has one reference port which was vented to ambient conditions. Each block also contains a plunger operated valve which redirected the sensing location of the transducers to a known reference pressure during calibration.

The total pressure rake was used to measure the total pressure at the cascade exit. A schematic of the total pressure rake is shown in Figure 11. Each of its 11 tubes has an inner diameter of 0.0635 cm and an outer diameter of 0.0889 cm. The centers of the tubes are equally spaced at 0.381 cm. This spacing resulted in a measurement span of 75 percent of the blade span.

The digital barometer was used to measure ambient pressure for each data point. It is equipped with an IEEE 488 interface which facilitated automation of the ambient pressure data acquisition. The digital barometer also has an internal heater to minimize the influence of ambient temperature fluctuations.

<u>Velocity and Temperature Measurement Subsystem.</u> The velocity and temperature measurement subsystem consists of a TSI Model IFA 100 Intelligent Flow Analyzer, a TSI Model IFA 200 System Multichannel Digitizer, a TSI x-configuration hot-film probe, and a thermocouple.

The intelligent flow analyzer was used to acquire velocity and temperature data. It contains a Model 140 Temperature Module which acquired voltage from the thermocouple. It also contains two Model 150 Constant Temperature Anemometer Modules which acquired voltages from the hot-film sensors. The gain, offset, and low pass filtering were provided by three Model 157 Signal Conditioners. As configured in this study, the gain was set to 5 and the offset was set to 2, to make maximum use of the range of the digitizer. The low pass filter was set to 5 kHz to eliminate aliasing at the 10 kHz sample rate.

The multichannel digitizer was used to scan and digitize the voltages from the signal conditioners in the intelligent flow analyzer. It contains three Model 252 Digitizers. As configured in this study, the digitizer acquired the velocity and temperature voltages simultaneously at a sample rate of 10 kHz.

The hot-film probe was used to acquire velocity and turbulence data. A schematic of the hot-film probe is shown in Figure 12. As shown in Figure 12, one hot-film probe consists of two sensors. TSI Model 1241-10 and Model 1241-20 x-configuration hot-film probes were used. Different model numbers were used based on the limited availability of the probes and because the probes are very fragile and consequently were broken during this study. All of the probes used gave acceptable results during the verification phase of the calibration (see Chapter IV).

The thermocouple used in this subsystem was used to measure the probe calibrator total temperature. This thermocouple is an Omega T-type copper-constantan thermocouple.

Temperature Measurement Subsystem. The temperature measurement subsystem was used to supplement the temperature measurement capability of the velocity and temperature measurement subsystem. This was needed because the velocity and temperature measurement subsystem is only capable of accommodating two thermocouples, and three thermocouples were used in this study. The temperature subsystem measured cascade total temperature and ambient temperature. It consists of a Hewlett-Packard Model 3455A Digital Voltmeter, a Hewlett-Packard Model 3495A Scanner, and 2 Omega T-type thermocouples.

Traverse Control Subsystem. The traverse control subsystem consists of two New England Affiliated Technologies Model 301 Programmable Motion Controllers and two Oriental Motor Company Stepper Motors. One of each of these was used for traverse in the cascade pitchwise direction, and one of each was used for traverse in the

21

spanwise direction. When attached to the traversing mechanism, the resolution of the subsystem is 0.0013 cm.

IV. Experimental Procedures

Hot-wire/film Calibration

Overview. Hot-wire anemometry was the method chosen to measure the velocity in the cascade outlet duct and the flow deflection through the cascade. Hot-wire anemometry is a method of determining the velocity and direction of a flowing fluid by measuring the amount of energy dissipated by a heated wire placed in the flow. The two commonly used methods of measuring this energy dissipation use either constant temperature or constant current principles. This study used the constant temperature method. In constant temperature anemometry, a current is passed through a thin wire and the amount of voltage required to keep the resistance, and hence the temperature, constant is measured. This input voltage is then used to determine the mass flow of the fluid flowing over the wire. From the mass flow, the velocity of the fluid is determined. With an x-configuration probe, the magnitudes of the velocities flowing across two wires at a known angle to each other are measured. From these magnitudes and the known angle between the wires, the direction and the magnitude of the velocity is determined. The operating principles of hot-wires and the development of the following equations are discussed by DeCook (1991). A comprehensive bibliography of sources detailing the theory of the electrical and thermodynamic relationships used in hot-wire anemometry may be found in A Bibliography of Thermal Anemometry by Peter Freymuth (1982).

As stated in chapter III, the probes used in this study were TSI Model 1241-10 and Model TSI 1241-20 hot-film probes. The difference between wire and film sensors is that the latter is a quartz cylinder with a conductive film deposited on it as opposed to an actual wire. Film sensors are typically less fragile than wire sensors; however wire sensors typically have higher frequency response than film sensors. The frequency response of

both types of sensors were at least twice as high as the sample rate, and therefore the sturdier hot-film sensors were chosen.

Governing Equations. The equations that follow are given by DeCook (1991) and were implemented with the calibration and data reduction software. The equations used in this study are summarized here for reference.

The fluid velocity was found using the definition of the Reynolds number. In this study, the Reynolds number was defined as

$$Re = \frac{\rho V_{eff} d_s}{\mu} \tag{15}$$

The effective velocity over each sensor of the probe is the vector sum of the component of velocity normal to the sensor axis and a fraction of the velocity parallel to the sensor axis. The relationship between the effective velocity and the actual fluid velocity is

$$V_{eff} = V\sqrt{\sin^2\alpha + k^2 \cos^2\alpha} \tag{16}$$

The cooling ratio is related to the ratio of the sensor length to the sensor diameter and was determined as a result of the angle and velocity calibration procedure described below.

The Reynolds number was found by solving the equation

$$Nu\left(\frac{T_r}{T}\right)^b = A + B\sqrt{Re} + CRe \tag{17}$$

The constants A, B, and C were determined by the previously mentioned calibration and the temperature loading factor (b)was determined by a separate temperature calibration.

24

Each of these calibration procedures are detailed below. The method of solving Equations (15)-(17) for the actual fluid velocity are thoroughly detailed by DeCook (1991).

Calibration Procedure. The calibration procedure for the hot-film probe consisted of two parts: (1) a velocity and angle calibration, and (2) a temperature calibration. The first of these required a set of velocity measurements and a set of angle measurements. This procedure determined the constants A, B, and C in equation (17) and the value of k in equation (16). The first step was accomplished by performing a 31-point unidirectional calibration at a constant air total temperature with velocities ranging from 65 m/s to 150 m/s. Next, a 21-point unidirectional angle calibration was performed with angles ranging from +10 deg to -10 deg. The ranges of velocities and angles used in the calibration were chosen based on expected ranges of velocities and angles to be found in the cascade. These choices proved to include at least two standard deviations of both the velocities and angles that were found in the cascade and were therefore determined to be acceptable. Equations (16) and (17) were solved by setting the temperature loading factor to zero to temporarily eliminate the temperature dependency of constants A, B, and C. These constants were then calculated for a range of values of k using the known calibrator velocities and angles with the temperature held constant. The resulting coefficients were then used with the known velocities and angles measured with the calibrator to calculate the sum squared error (SSE). The sum squared error was computed (with the value of b set to zero) for each value of k by

$$SSE = \sum_{j=1}^{n} \left[Nu_j \left(\frac{T_{r_j}}{T_j} \right)^b - \left(A + B\sqrt{Re_j} + CRe_j \right) \right]^2 \qquad (18)$$

The value of k which produced the lowest *SSE* for the velocity and angle calibration was used. The values used in this study varied from 0.09 to 0.45 and depended on the particular hot-film sensor that was used.

With the values of A, B, and C determined, the temperature calibration was accomplished to determine the value of the temperature loading coefficient. This procedure consisted of taking a series of velocity measurements while the total temperature of the airflow was varied. The range of temperatures used in the calibration was chosen based on an expected range of temperatures to be found in the cascade. This process was repeated twice to include measurements of both high and low velocities at both high and low temperatures. Equation (18) was again solved by using the previously determined value for k and a range of values for b. The value of b which yielded the smallest sum squared error over the expected temperature range was chosen. The choice of b was dependent on the particular hot-film sensor that was used and varied from -0.15 to 0.44 .

Calibration Verification. With the values of the coefficients determined, the calibration was verified by comparing the velocities and angles indicated by the probe to known velocities and angles throughout the calibration temperature range. The results of this verification showed the probe to be accurate to within ±0.25 degrees and ±0.5 m/s within a 4°C temperature range. The center of this range depended on the particular probe that was used. Deviations outside of this range produced progressively larger discrepancies between the actual flow conditions and the measured flow conditions. These discrepancies were particularly evident with the angle measurements. The angle measurement discrepancies increased slowly up to a maximum of about 0.5 deg at the extremes of a 10°C temperature range. Therefore it was determined to actively control the total temperature of the flow such that a 4°C temperature range was not exceeded during testing.

The velocities and directions measured with the hot-film probe were measured relative to the line bisecting the angle between the two sensors. This velocity was transformed into the cascade axis system. This details of this transformation are given by DeCook (1991).

Pressure Measurement Subsystem Calibration

The PSI 8400 pressure scanner was calibrated using an internal standard and an automated calibration process. Because the calibration was automated, the time required to calibrate the 96 pressure transducers in the system was less than 4 minutes. This allowed a complete calibration (determination of the voltage/pressure slope and offset) of each transducer to be performed prior to each test run. A complete calibration consisted of a 5-point calibration which ranged from -1.0 psid to +1.0 psid. In addition to the complete calibration prior to each test run, the data acquisition software included provisions to adjust the offset of the voltage/pressure curve should the temperature drift beyond 1.5°C from the calibration temperature. The implementation details of the calibration may be found in the PSI 8400 Pressure Scanner User's Manual (1993).

Cascade Inlet Flow Conditions

A survey of the throat was made with the hot-film probe to determine the throat velocity distribution and turbulence intensity. Turbulence intensity quantifies the magnitude of unsteady velocity fluctuations which are superimposed on the steady mean flow velocity. In this study, velocity fluctuations were measured in the cascade x-y plane (Figure 4) with an x-configuration hot-film probe. Turbulence intensity (Tu) for one data point in a given measurement plane is defined as

$$Tu = \frac{\sqrt{\frac{1}{2}(\overline{V_x}^2 + \overline{V_y}^2)}}{\overline{V}} \qquad (19)$$

$$\text{where } \overline{V_x} = \sqrt{\frac{\sum_{j=1}^{L}(V_{x_j} - \overline{V_x})^2}{L}} \qquad (20)$$

$$\overline{V_y} = \sqrt{\frac{\sum_{j=1}^{L}(V_{y_j} - \overline{V_y})^2}{L}} \qquad (21)$$

where L is 100 samples taken at each data point. The survey was made with the test section removed because the test section interfered with the hot-film probe. The plane surveyed was located 5.1 cm upstream of the throat exit. This survey revealed a slight skewness to the velocity distribution. From the survey, the mass averaged turbulence intensity was found to be 0.68 percent and the mass averaged velocity was found to be 135.6 m/s.

Periodicity. The periodicity of the inlet static pressure distribution was measured with the test section in place and the straight trailing edge blades installed at each of the four incidence angles. The inlet periodicity was determined by sampling 23 inlet static pressure ports. These ports were located $0.05c$ upstream from the blade row leading edge plane, were spaced at 0.46 cm intervals, and covered a range of about 3 blade spacings centered on the leading edge of the center blade. The inlet plane static pressure distribution was found to be periodic. The periodicity results are discussed in Chapter V. Evaluation of the periodicity results led to a method of estimating the cascade inlet static pressure for each data point in a given measurement plane. This method involved averaging a centered period of static pressure values. The nine inlet static pressure ports that were centered on the center blade were chosen to be monitored during testing. The arithmetic mean of the pressure measurements from these ports was taken to be the inlet static pressure.

Inlet Total Pressure.   The final aspect of the inlet flow conditions that was evaluated was the inlet total pressure. In this study, the stilling chamber static pressure was taken to be the stilling chamber total pressure. The total pressure losses through the bellmouth and the total pressure losses due to the endwall boundary layer suction were quantified experimentally. The measurement made to determine these losses was made with the straight trailing edge blades mounted in the test section at the +4.49 deg incidence. The total pressure rake was placed so that it was about $0.05c$ upstream of the blade row at an angle of approximately 9.5 deg to the flow direction. This location was downstream of the endwall suction slots and at the same axial location as the inlet static ports. The 9.5 deg angle was determined to be acceptable since pitot tubes are reasonably insensitive to small angle variations. The value of the cascade inlet total pressure was taken to be the arithmetic mean of the 11 total pressure readings of the total pressure rake and was found to be 99.85 percent of the stilling chamber total pressure ($0.9985\ P_{mk}$). For all calculations in this study, the inlet total pressure was considered to be $0.9985\ P_{mk}$ where P_{mk} varied from 15.5 psia to 15.8 psia.

Cascade Exit Flow Conditions

The exit plane of the cascade was evaluated for static pressure periodicity. The size of the measurement window and discretization of the measurement window were also determined.

Periodicity.   The cascade exit static pressure periodicity was evaluated by sampling 23 sidewall static pressure ports. These ports were spaced at 0.46 cm intervals, were centered on the trailing edge of the center blade, and covered a range of about 3 blade spacings. This row of ports was located $0.05c$ downstream from the blade row trailing edge plane. The measurements were made with the straight trailing edge blades mounted in the test section at the +4.49 deg incidence. The exit plane static pressure

distribution was found to be periodic. The periodicity results are discussed in Chapter V. Evaluating the periodicity results led to a method of estimating the cascade exit static pressure for each data point in a given measurement plane. This method involved averaging a centered period of static pressure values. The nine exit static pressure ports that were centered on the center blade were chosen to be monitored during testing. The arithmetic mean of the pressure measurements from these ports was taken to be the exit static pressure.

Establishment of the Sampling Window. With the periodicity evaluated, five planes were sampled with the hot-film probe. These surveys, which were made with the straight trailing edge blades installed at the +4.49 deg incidence angle, were used to determine the appropriate window to sample during the data acquisition runs. The planes that were surveyed were located at x/c = 0.05, 0.30, 0.56, 0.96, and 1.37 downstream from the cascade exit where the rows of sidewall static ports were located. Using these rows of static ports to determine the location of the measurement planes allowed the static pressure at each x/c location to be most accurately measured.

Contour plots of the velocity distributions were evaluated to determine an appropriate sampling window for all of the planes. The chosen sampling window is shown in Figures 13 and 14 where the center blade is located at y = 0. For the initial velocity surveys, relatively coarse grid spacings of 0.127 cm in the y direction and 0.279 cm in the z direction were used. As can be seen in Figures 13 and 14, the blade wakes and associated vortices migrated in the negative pitchwise direction from the trailing edge of the center blade as they developed downstream of the cascade exit plane. To capture this phenomenon, the sampling window was chosen to cover a range from 1.22 cm above the trailing edge of the center blade to 2.16 cm below the trailing edge of the center blade. This range covered one blade spacing and was chosen so that the extremes of the window were outside of the blade wakes. The window was chosen such that all wake turbulence

and vortices in the window came from the center blade. The window was also chosen to allow for an anticipated greater migration of the blade wakes and vortices at the highest incidence angle.

With the range of the window chosen, the discretization of the window was then determined. From the preliminary contour plots, it could be seen that conditions changed much more rapidly in the pitchwise (y) direction than in the spanwise (z) direction. This indicated that the sampling grid should be as fine as practical in the pitch direction and could be coarser in the span direction. The total pressure rake spanned a distance of 3.81 cm and had tubes at 0.381 cm intervals. The hot-film probe however, could be placed at much smaller intervals but could only scan an additional 0.05 cm in the spanwise direction. It was decided that the distance and spacing of the total pressure rake would be adequate for the hot-film probe as well. A much finer grid of 0.025 cm was used in the pitch direction than in the span direction for both instruments. This spacing ensured that approximately 10 measurements were taken within the wake because the thickness of the blade wake was found to be approximately 0.25 cm at the first sampling plane. While a finer grid would have provided more resolution, the time required to scan the window would have been excessive. The measurement plane discretization was chosen to be the same for the hot-film probe and the total pressure rake; this resulted in 1474 points being sampled for each window surveyed.

Data Acquisition

Tailboard Balancing. The tailboards (Figure 7) were balanced prior to the first test run for each configuration. "Tailboard balancing" refers to the procedure of adjusting the cascade tailboards such that they are optimally positioned. This procedure was necessary to minimize the influence of the tailboards on the flow deflection for each cascade configuration. The two primary objectives of balancing the tailboards were to

31

ensure the diffuser exit pressure was equal to ambient pressure and to ensure that the top and bottom tailboards had the same pressure distribution. Since it was desired to have ambient pressure at the exit plane of the diffuser, the pressure at the exit plane of the blade row varied with flow deflection angle. In all cases the tailboards were balanced to achieve 0 ± 0.09 psig at the diffuser exit and 0 ± 0.09 psig between top and bottom. This resulted in blade row exit pressures of 0.047 to 0.083 psig depending on the particular cascade configuration. These procedures also ensured the previously mentioned periodic pressure distribution across the blade exit plane. The tailboards were balanced with the instrument to be used, either the total pressure rake or the hot-film probe, installed in the cascade.

Instrument Alignment. The procedures for aligning each of the instruments (the hot-film probe and the total pressure rake) were nearly the same. Each was centered spanwise downstream of the center blade and the reference point of the traverse control subsystem was set to zero. The spanwise alignment process required the removal of the sidewall and the subsequent balancing of the tailboards (reference Figure 7). The pitchwise alignment was made with the tailboards aligned and the airflow turned on. The precision with which the instruments could be aligned was ± 0.13 mm. An additional alignment check was made for the hot-film probe to ensure that it was aligned with the cascade x-axis. This check was made in the flow and any corrections for misalignment were made to the reduced data.

Pressure Measurement. The pressure measurement process was fully automated. All pressures were read into the central computer from the pressure measurement subsystem. The pressure data received by the central computer were in reduced form (i.e., psig). The arithmetic mean of the static pressure readings from the nine ports at the cascade inlet was calculated; and the arithmetic mean of the static pressure readings from the nine ports at the cascade exit measurement plane was calculated. The resulting mean values were taken to be the inlet and exit static pressures respectively, and were written to

32

the data file for each data point. The stilling chamber static pressure was read directly into the data file. The static pressure ports on both surfaces of the center blade were sampled by the pressure scanner for each blade configuration at each of the four incidence angles.

Each pressure reading passed on to the central computer represented the arithmetic mean of 11 samples taken at 208 Hz. The pressure transducers were referenced to ambient pressure. The ambient pressure was monitored by the central computer via the digital barometer. Because the elapsed time between the first data point and the last data point was as long as 90 minutes, an ambient pressure reading was taken for each of the 1474 data points.

Temperature Measurement. The temperature measurement process was fully automated. The thermocouples which monitored the stilling chamber total temperature and the ambient temperature were read for each data point. The temperature data received by the central computer were in raw form (i.e., Volts). These voltages were then transformed into temperatures during data reduction.

Total Pressure Rake Positioning. The total pressure rake (Figure 11) positioning procedures were automated except for the initial alignment. The airflow was turned on and the tank and ambient temperatures were allowed to stabilize. The central computer positioned the traversing mechanism at the highest pitchwise point of the traverse via the traverse control subsystem. All total pressure rake data runs were made using a vertical traverse with the rake aligned with the span of the blades. At each point of the traverse, the readings from each of the 11 total pressure tubes were read from the pressure scanner. If the change in pressure from one point to the next resulted in a change of more than 0.02 psid for any of the 11 total pressure rake tubes, that point was re-taken for all 11 tubes. This process was repeated until all tubes showed a change in pressure of less than 0.02 psid for two consecutive samples. All 11 pressures were recorded simultaneously. The previously mentioned grid spacing resulted in 134 vertical points being taken to cover the

survey window and required from 7 to 25 minutes to complete for each measurement plane.

Hot-film Probe Positioning. The hot-film probe (Figure 12) positioning procedures were also automated except for the initial alignment, but used a slightly different scanning pattern than did the pressure rake. The difference being that it traversed in the span direction in addition to the pitch direction. This difference required that the probe be positioned for each of the 1474 data points (as opposed to only 134 vertical points) and caused significantly longer run times of 90 minutes. These longer run times and the sensitivity of the hot-film sensors to temperature changes made it necessary to actively control the stilling chamber total temperature. This was done by configuring the blower intake such that a combination of outdoor air and laboratory air flowed into the blower. Outdoor air entered the blower containment room from a fixed geometry duct. Laboratory air entered the blower through the blower containment room door. The proper mixture of outdoor/laboratory air was maintained by varying the door position such that the total temperature of the stilling chamber was maintained within the 4°C range as mentioned in the calibration procedure. At each point in the measurement plane, 100 samples of the hot-film voltages were taken at a rate of 10 kHz. The arithmetic mean of the 100 samples and the root mean squared (rms) fluctuation from the mean for each hot-film voltage was recorded along with the pressure and temperature data at each point. These quantities were written to data files for subsequent data reduction.

Data Reduction

The data reduction was accomplished by employing two separate, but not independent, reduction procedures. These two procedures were the total pressure rake data reduction and the hot-film probe data reduction. As discussed below, the two procedures were not independent because the total pressure rake data reduction procedure

depended on the results of the hot-film probe data reduction procedure to implement the mass averaging of the total pressure loss coefficient. Both reduction procedures reduced the thermocouple voltages by using a calibration-derived temperature/voltage function. The reduction procedures are discussed below.

Total Pressure Rake Data Reduction. In this study, the total pressure loss coefficient was the only reported quantity that used measurements taken by the total pressure rake. The total pressure rake was used to measure P_{02} at each location in the measurement plane. With P_{02} measured, the quantity $(P_{01}-P_{02})$ was calculated. Recall P_{01} was the total pressure at the cascade inlet and was found experimentally to be $0.9985\,P_{ink}$. The value for ρ_1 in Equation (4) was calculated by

$$\rho_1 = \frac{p_1}{RT_1} \tag{22}$$

The value for T_1 in Equation (22) was calculated by

$$T_1 = T_{ink}\left(\frac{p_1}{P_{01}}\right)^{\frac{\gamma-1}{\gamma}} \tag{23}$$

The value for V_1 in Equation (4) was calculated by

$$V_1 = \sqrt{2\frac{\gamma R}{\gamma-1}\left(T_{ink}-T_1\right)} \tag{24}$$

After the total pressure loss coefficient was computed for each location in the measurement plane, these values were mass averaged. This mass averaged result provided a total pressure loss coefficient for the measurement plane as a whole. The mass averaging was accomplished according to Equation (7) with A_j being replaced by ϖ_j. The value for ρ_2 in the mass averaging scheme was calculated using Equations (22) and (23)

with all inlet subscripts (1) changed to measurement plane subscripts (2). The velocity used in the mass averaging scheme was the axial component of velocity taken from the hot-film probe data reduction results.

Hot-film Probe Data Reduction. Values for the axial velocity density ratio, flow deflection, outlet turbulence intensity, wake velocity deficit, and outlet velocity variance were calculated solely from data acquired with the hot-film probe. The reduction of the hot-film probe voltages into velocities and angles at each location in the measurement plane was accomplished using Equation (17) where velocity is embedded in the Reynolds number and voltage is embedded in the Nusselt number for each sensor. The flow angle is then found from the velocity about each sensor and the known angle between the sensors. A detailed discussion of the reduction procedures used to transform the hot-film probe voltages to velocities and angles is given by DeCook (1991).

The flow deflection angles calculated for each location in the measurement plane were mass averaged. This was accomplished by using Equation (7).

The mass weighted outlet velocity variance was calculated using Equation (13). The values for the other quantities in Equation (13) were calculated as previously discussed. As explained in Chapter II, this expression for outlet velocity variance is a mass weighted value and thus did not require implementation of Equation (7).

The wake velocity deficit was calculated using Equation (8). The mass averaged value for the velocity in the measurement plane was calculated using Equation (7). In this study, the freestream velocity in Equation (8) was assumed to be the arithmetic mean of the velocities within the 75th percentile of all the velocities recorded in the measurement plane. This assumption was found to reasonably valid by examining the results presented in Chapter V.

The nondimensional static pressure rise was calculated using Equation (3). In this equation, p was taken to be the arithmetic mean of the sidewall static pressures measured

at the same axial location as the measurement plane. The other quantities in Equation (3) were calculated as previously discussed. The blade static pressure coefficients were also calculated using Equation (3). In this case, p was taken to be the blade surface static pressure measured at each location on the blade surface as listed in Table 3.

The axial velocity density ratio was calculated using Equation (2). The quantities ρ_2 and V_{x_2} in Equation (2) were taken to be those values calculated at the midspan locations ($z = 0$) in the measurement plane. This resulted in $n = 134$ midspan locations. The other quantities in Equation (2) were calculated as previously discussed where

$$V_{x_1} = V_1 \cos \alpha_1.$$

Error Analysis

The manufacturer specified accuracies for the various pieces of data acquisition equipment are discussed in Appendix C. The errors resulting from these accuracies are calculated in Appendix C and summarized in Table 5.

Table 5. Estimated Equipment Errors

Parameter	Expected Error (%)
$AVDR$	1
Blade C_p	2
Exit Plane C_p	2
ϖ	2
Tu	1
WVD	3
$\bar{\sigma}^2$	1

Repeatability

The results of this study were validated by conducting repeat test runs. These repeat runs were normally made at the $x/c = 0.05$ measurement plane. This location was chosen since it was determined to be the most sensitive to changes in either cascade conditions or instrument alignment and calibration. Before a repeat run was made, the cascade blower was turned off and the system was allowed to blow down. In most cases the repeat run was made approximately eight hours after the initial run at that location. In some cases the repeat run was made on the day following the initial run with the system having been shut down for several hours.

A repeat run was considered to validate the initial results if the repeated run yielded results which differed from the initial results by no more than the estimated errors listed in Table 5. If the repeat run did not corroborate the initial results, then another repeat run was made at the $x/c = 0.56$ measurement plane. If this run also failed to corroborate the initial results, the cause of the different results was investigated and corrected. Following this investigation, the data acquisition process was repeated in its entirety.

V. Discussion of Results

The Results are presented as a function of location downstream from the cascade and also as a function of incidence angle. The dependence of the various quantities on location downstream provides insight into the trends which resulted from the wake development process. However, the trends associated with incidence angle variations can be difficult to visualize when plotted versus location downstream; therefore both formats are used. The amount of uncertainty, or estimated error, associated with each quantity presented in this chapter is presented in Table 5. Three-dimensional contour plots are also presented to support and clarify results as needed.

Evaluation of the Cascade as a Model

The axial velocity density ratio (*AVDR*) through the cascade and the periodicity of the static pressure distributions at the cascade inlet and exit were used as the basis of evaluating the cascade as a model. The *AVDR* evaluation was focused on determining the cascade flow condition relative to the two-dimensional flow condition. It is important to emphasize however that achieving two-dimensional flow was not an objective of this experiment. The two-dimensional flow condition (*AVDR* = 1) was used only as a point of comparison to determine, in relative terms, the impact of the secondary flow on the midspan mass flux. The periodicity on the other hand was evaluated in a more qualitative manner.

Axial Velocity Density Ratio. The *AVDR* was calculated at the midspan of the five measurement planes downstream of the cascade using both blade configurations. The results are shown in Figure 15. From these results it can be seen for all test runs that

0.97 < AVDR < 1.04. These bounds on the AVDR indicate that the midspan mass flux

through the cascade increased by as much as 4 percent or decreased by as much as 3

percent. Scholz (1977) establishes the bounds of quasi two-dimensional flow as being

0.8 < AVDR < 1.2. However as stated in Chapter II, the AVDR is not sensitive to the

presence of secondary flow which may be concentrated away from the midspan of the

blade. This type of secondary flow was found to exist in the cascade. Because its

presence is more easily observed from an examination of the total pressure losses, the

secondary flow in the cascade is discussed in the total pressure loss results.

The AVDR results also indicate that the crenulated blades generally showed a

higher AVDR than that of the straight trailing edge blades. It is suspected that this

phenomenon is related to the crenulation induced vortices. These vortices shed on either

side of a crenulation and are characterized by a defect in axial mass flux. Because a

crenulation is located at center span, it forces a local contraction of the flow between the

two vortices which results in an increase in midspan axial mass flux.

Periodicity. The inlet and exit static pressure distribution periodicity were

evaluated at 0.05c upstream from the blade leading edge and 0.05c downstream from the

blade trailing edge respectively. Measurements were taken across three blade spacings for

each incidence angle. The periodicity results are shown as pitchwise static pressure

distributions nondimensionalized by inlet total pressure in Figure 16. The results show

that the exit pressure distributions for all incidence angles were essentially periodic. This

result was forced by the tailboard balancing procedures outlined in Chapter IV. The

consequence of this tailboard balancing technique is shown by the resulting skewness and

variation in the peaks of the inlet pressure distributions. Although the inlet pressure

distributions exhibit noticeable skewness and variations in peak values, these imperfections

are relatively small compared to the amplitude of their respective distributions.

The results show very good periodicity at the cascade inlet and exit. It was determined that the periodicity was acceptable for testing.

Evaluation of Crenulated Blade Performance

The evaluation of crenulated blade performance at various incidence angles was performed by comparing the performance of a cascade with crenulated blades to that of a cascade with blades that were not crenulated (straight trailing edge blades) at four incidence angles. The following points of comparison were made:

1. blade surface static pressure distribution

2. static pressure rise

3. total pressure loss

4. flow deflection

With the exception of blade surface static pressures, measurements for each blade configuration were taken at the five measurement planes for each of the four incidence angles. The blade surface static pressure measurements were taken through the static pressure ports on the center blade of each cascade configuration tested.

Blade Surface Static Pressure Distribution. The blade surface static pressure measurements were taken at midspan of the center blade at the locations along the chord shown in Table 3. The resulting pressure distributions are shown in Figure 17. The results show that as incidence angle was increased for both the crenulated blade and the straight trailing edge blade, the blades became more highly loaded near the leading edge. This is evident in Figure 17 by the increasing pressure differential between the pressure surface and the suction surface at $x/c < 0.20$. This trend was accompanied by a less substantial decreased loading of the blades at $x/c > 0.40$. The net effect was then for an increase in incidence angle to cause the loading of the blades to increase which corresponds to an increase in flow turning (flow deflection).

The results also indicate that the crenulated blades were loaded less than the straight trailing edge blades at all incidence angles tested. The greatest difference between the blade configurations is seen at the highest incidence angle. This trend is consistently seen locally in the results for all incidence angles at $0.60 < x/c < 0.70$. This local trend is most likely due to the presence of the crenulation at midspan which allows the flow on the pressure surface to merge with the flow on the suction surface at $x/c = 0.75$ hence forcing the pressures to be equal at that point. This creates an effective midspan trailing edge at $x/c = 0.75$ which is then felt upstream.

The results from the blade surface static pressure measurements indicate that the crenulated blades were loaded less than the straight trailing edge blades and therefore should cause less flow deflection than should the straight trailing edge blades at the same incidence angle. This is consistent with the measured flow deflection results which are presented in a later discussion. The loading of the blades, which is a function of flow deflection, is also quantified in the flow deflection results.

Cascade Static Pressure Rise. The static pressure rise across the cascade was measured at the five measurement planes for each blade configuration at the four incidence angles. The results expressed as the difference in static pressure between the measurement plane and cascade inlet, divided by the inlet dynamic pressure are shown in Figure 18. The results show that for all incidence angles and both blade configurations that the majority of diffusion has occurred upstream from $x/c = 0.30$, more so for the crenulated blades.

Figures 18c and 18d show for both blade configurations that the pressure rise across the cascade increased with increasing incidence angle up to +9.32 deg and then decreased slightly as the incidence angle was increased to +12.44 deg. This trend provides an indication that the blades may have approached a stalled condition at the highest incidence angle similarly to how an isolated airfoil loses lift as angle of attack is increased beyond some maximum. This decrease in pressure rise at the highest incidence angle was

found to be less severe for the crenulated blade than for the straight trailing edge blade. In fact, the crenulated blades caused a greater pressure rise than did the straight trailing edge blades at the two measurement planes nearest the blade trailing edge for the highest incidence angle. At the other incidence angles tested, the results show that the straight trailing edge blades caused more pressure rise than did the crenulated blades. This is consistent with the implication made in the blade surface static pressure results that the straight trailing edge blades cause more flow deflection than do the crenulated blades at the same incidence angle (the highest incidence angle being excepted).

Total Pressure Losses. The total pressure losses across the cascade were measured at the five measurement planes for each blade configuration at the four incidence angles. The results are expressed as the mass averaged difference between the total pressure at the cascade inlet and the total pressure at the cascade exit measurement plane, divided by the inlet dynamic pressure. The results are shown in Figure 19. As can be seen from Figures 19a and 19b, the total pressure losses increased moderately for each blade configuration/incidence angle combination as the measurement plane was moved further downstream from the blade trailing edge. This trend is physically sensible because the wake region is known to be a region where viscous losses are incurred due to mixing. It is also evident from Figures 19a and 19b that the total pressure losses increased substantially for each blade configuration/measurement plane combination as incidence angle was increased. This trend is more easily seen in Figures 19c and 19d and is explained by the relative loadings of the blades. As shown in the blade static pressure results, the blades at higher incidence angles were more highly loaded than the blades at lower incidence angles. A higher loading causes a stronger disturbance on the flow which in turn causes greater viscous losses through the cascade.

Examination of the differences in total pressure losses between the crenulated blades and the straight trailing edge blades at the same incidence angle reveals mixed

43

effects. At the three lowest incidence angles, it can be seen from Figure 19 that there were negligible differences in losses between the two blade configurations. However, a dramatic difference in losses can be seen at the highest incidence angle. From Figure 19 it can be seen that the losses incurred by the crenulated blades were approximately 20 percent less than those of the straight trailing edge blades at the +12.44 deg incidence angle. This notable difference prompted a closer look at the distribution of the total pressure losses within the measurement plane.

Because the difference in mass averaged losses was found to not be related to the particular choice of measurement plane, the loss distributions were examined only at the x/c = 0.56 plane. The total pressure loss distribution for each blade configuration at each incidence angle is shown in Figures 20 - 23 where the center blade is located at y = 0. These distributions reveal several important aspects of the flow downstream of the cascade. The loss distributions provide an approximate illustration of the size and location of the blade wakes, the passage vortices, and the crenulation induced vortices. This is true because these are the primary total pressure loss mechanisms in the cascade. Representations of blade wakes are most easily seen in Figures 20a and 21a. They are characterized by the nearly horizontal parallel isolines near the midspan of the blade. Interactions of the blade wakes with the passage vortices also can be seen in Figures 20a and 21a. They are characterized by the widening region of losses as the distance from midspan is increased. These interactions extend outside of the measurement window and are only partially represented.

Interactions of the crenulation induced vortices with the blade wake can most easily be seen by comparing Figures 23a and 23b. Figure 23a shows a wide region of high losses extending across the span of the blade. Figure 23b shows that the effect of the crenulation induced vortices was to pinch this region into smaller (in magnitude and size) loss plateaus and to reduce the losses directly behind the crenulations. This effect of the

crenulation induced vortices is the key to the explanation of why the mass averaged total pressure losses in Figure 19 were lower for the crenulated blades than for the straight trailing edge blades only at the highest incidence angle. Comparing Figures 20a - 22a to Figures 20b - 22b shows that although the crenulations reduced the losses locally, the gross area of losses increased; thus the net effect was merely a redistribution (not a reduction) of losses. This was not the case at the highest incidence angle where the gross area of losses and the magnitudes of the losses were reduced by the crenulated blades.

Flow Deflection. The flow deflection was measured at the five measurement planes for each blade configuration at the four incidence angles. The results are expressed as the mass averaged flow deflection. Recall flow deflection is defined as the difference between the air outlet angle (α_2) and the air inlet angle (α_1). The results presented in Figure 24 show that higher incidence angles caused higher flow deflections for each blade configuration. This is consistent with the blade static pressure distribution results where it was found that a higher blade loading resulted from higher incidence angles. Figures 24a and 24b show that the flow deflection changed a negligible amount (very near the estimated error) as the measurement plane was moved further from the blade trailing edge.

Figures 24c and 24d serve to show the differences in flow deflection between the crenulated blades and the straight trailing edge blades. For all incidence angles tested, the crenulated blades caused less flow deflection than did the straight trailing edge blades. The flow deflection results for each blade configuration at the x/c = 0.56 measurement plane are compared in Table 6. A comparison of the flow deflections for each blade configuration reveals that the crenulated blades reduced the flow deflection by approximately 8 percent at the lower 3 incidence angles and by 10 percent at the highest incidence angle. These results correspond to a 1.9 deg reduction at -1.08 deg incidence, a 2.4 deg reduction at +4.49 deg incidence, a 2.6 deg reduction at +9.32 deg incidence, and a 3.7 deg reduction at +12.44 deg incidence.

Table 6. Comparison of Flow Deflections

		Straight TE		Crenulated TE		Difference
i (deg)	α_1 (deg)	ε (deg)	α_2 (deg)	ε (deg)	α_2 (deg)	$\Delta\varepsilon/\varepsilon_s$ (%)
-1.08	25.43	23.84	1.59	21.93	3.50	-8.0
+4.49	31.00	27.95	3.05	25.60	5.40	-8.4
+9.32	35.83	32.03	3.80	29.41	6.42	-8.2
+12.44	38.95	35.53	3.42	31.82	7.13	-10.4

The determination of the flow deflection for each cascade configuration permits quantification of the blade loading. This can be done by introducing the diffusion factor (*DF*). The diffusion factor is defined in terms of the velocity gradient on the suction surface of the blade and is empirically based on two-dimensional cascade data. The full derivation of the diffusion factor is given by Lieblein et al. (1953). Cohen et al. (1987) present an approximate expression for the *DF* in an axial flow compressor blade row in terms of velocities. This approximation can be reduced to the following expression for a cascade in terms of flow angles:

$$DF \approx 1 - \frac{\cos\alpha_1}{\cos\alpha_2} + \frac{s}{c} \cdot \frac{\cos\alpha_1}{2}(\tan\alpha_1 - \tan\alpha_2) \qquad (25)$$

Using the appropriate values from Tables 4 and 6, the diffusion factor for each cascade configuration in this study is compared in Table 7.

46

Table 7. Comparison of Diffusion Factors

i (deg)	DF		Difference (%)
	Straight TE	Crenulated TE	$\Delta DF/DF_s$
-1.08	0.233	0.221	-5.1
+4.49	0.300	0.285	-5.0
+9.32	0.367	0.351	-4.4
+12.44	0.417	0.396	-5.0

The diffusion factor comparison in Table 7 indicates that the crenulations were observed to reduce the blade loading by 4 to 5 percent throughout the range of incidence angles tested. According to Cohen et al. (1987), losses in stator blades are largely unaffected by increases in DF up to about 0.6 while losses at the rotor tip of an axial flow compressor increase rapidly at values of DF above 0.4. The loss results from this study (Figure 19c) however show that the losses for the straight trailing edge blade doubled as the value of DF was increased from 0.367 to 0.417. This apparent discrepancy is most likely due to the strong three-dimensional flow in the cascade. The results show that the presence of three-dimensional flow in the cascade serves to prematurely increase flow losses as incidence angle is increased. However, the crenulations appear to redistribute the three-dimensional flow and thereby reduce the losses as shown in Figures 19c and 19d, and Figures 23a and 23b at the highest incidence angle.

Although the flow deflection differences between the blade configurations appear to be relatively small at the +12.44 deg incidence angle, they become substantial when examined on a scale of the same order as the observed differences. The deviation angle provides such a scale. Recall that the deviation angle is the difference between the air

outlet angle (α_2) and the blade outlet angle ($\alpha'_2 = -4.00$ deg in this study). The deviation angles for the crenulated blades and the straight trailing edge blades are compared in Table 8.

Table 8. Comparison of Deviation Angles

i (deg)	δ (deg)		Difference
	Straight TE	Crenulated TE	$\Delta\delta/\delta_s$ (%)
-1.08	5.59	7.50	34.2
+4.49	7.05	9.40	33.3
+9.32	7.80	10.42	33.6
+12.44	7.42	11.13	50.0

When examined on this scale, it is seen that the crenulated blades caused a deviation angle 33 to 34 percent greater than did the straight blades from -1.08 to +9.32 deg incidence whereas the difference between the blade configurations increased to 50 percent at +12.44 deg of incidence. Closer examination of Table 8 reveals that the deviation angle decreased for the straight trailing edge blade as the incidence angle was increased from +9.32 deg to +12.44 deg. This result was unexpected since typically deviation angle increases as incidence angle increases. These results imply that a phenomenal change has occurred in the flow about the straight trailing edge blade as the incidence angle was increased beyond +9.32 deg. This change did not occur for the crenulated blade.

The deviation angle results combined with the static pressure rise results and total pressure loss results indicate that the phenomenal change in the flow about the straight trailing edge blade at the highest incidence angle has caused the deviation angle and the

static pressure rise to decrease. The onset of this flow phenomenon is suspected to be the result of the high blade loading combined with the strong three-dimensional flow about the blade. It is suspected that a separation bubble has formed on the suction surface of the straight trailing edge blade where the boundary layer has reattached downstream of the bubble as fully turbulent.

A turbulent boundary layer has a stronger resistance to separation on a convex surface than does a laminar boundary layer which implies that the reduced deviation angle of the straight trailing edge blade could be the result of boundary layer transition. A turbulent boundary layer is also characterized by higher losses than a laminar boundary layer which implies that the dramatic increase in total pressure loss of the straight trailing edge blade could also be the result of boundary layer transition. Although the analytic prediction of transition is extremely complex, it is known to be Reynolds number dependent. It would not be unusual for turbulent transition to occur at blade chord Reynolds numbers on the order of $5 (10)^5$, particularly under the influence of an adverse pressure gradient. In this study the blade chord Reynolds numbers were approximately $4.1 (10)^5$ and the static pressure ratios of the blade suction surface and pressure surface were estimated from the blade static pressure results. From Equation (3), Figure 17, and knowledge of the inlet dynamic pressure and inlet static pressure, the pressure ratio across each blade surface was calculated for each blade configuration and incidence angle and is shown in Table 9. The blade surface pressure ratio is defined for the suction surface as

$$PR_{ss} = \frac{p(x/c = 0.695)}{p(x/c = 0.045)}$$

where $p(x/c)$ is the blade surface static pressure at the given blade chord location. The blade surface pressure ratio for the pressure surface is likewise defined as

$$PR_{ps} = \frac{p(x/c = 0.670)}{p(x/c = 0.070)}$$

Table 9. Comparison of Blade Surface Pressure Ratios

	PR_{ss}		PR_{ps}	
i (deg)	Straight TE	Crenulated TE	Straight TE	Crenulated TE
-1.08	1.067	1.062	0.989	0.982
+4.49	1.123	1.109	0.977	0.970
+9.32	1.156	1.156	0.966	0.958
+12.44	1.147	1.162	0.959	0.951

These results, derived from the blade static pressure results, form the only results that were taken from measurements within the blade surface boundary layers. It is clear that some physical phenomenon occurred which effectively relieved (although not entirely) the adverse pressure gradient on the suction surface of the straight trailing edge blade at the +12.44 deg incidence angle. This phenomenon did not occur on the crenulated blade. This lends plausibility to the argument that the straight trailing edge blade suction surface boundary layer has transitioned to turbulent via a separation bubble at the +12.44 deg incidence. The observed flow phenomena is consistent with current technical knowledge as given by Fottner (1989). In the words of Fottner (1989), the separation bubble is more precisely termed a "long separation bubble" due to the reduced pressure gradient on the blade suction surface. A schematic of the transition phenomena which is suspected to have occurred on the straight trailing edge blade suction surface is shown in Figure 25. However, this boundary layer transition hypothesis is based on indirect indicators of

50

turbulence and is therefore supplemented by direct measurements of the cascade outlet turbulence intensity. These results are discussed below.

Evaluation of Crenulated Blade Wake Mixing Characteristics

Like the evaluation of crenulated blade performance, the evaluation of crenulated blade wake mixing characteristics for various incidence angles was performed by comparing the characteristics of a cascade with crenulated blades to those of a cascade with straight trailing edge blades at four incidence angles. The following points of comparison were made:

1. outlet turbulence intensity
2. wake velocity deficit
3. outlet velocity variance

Outlet Turbulence Intensity. The outlet turbulence measurements were taken at the five measurement planes for each blade configuration at the four incidence angles. The results are expressed as the mass averaged outlet turbulence intensity.

The mass averaged turbulence intensity results are presented in Figure 26 and show that turbulence intensity was found to increase with a corresponding increase in incidence angle for each blade configuration. Figures 26a and 26b show that as the blade wake developed downstream of the cascade, turbulence intensity increased moderately to a maximum and then decreased for the highest two incidence angles. Turbulence intensity for the lowest two incidence angles increased only slightly and did not decrease with increasing distance from the cascade. This is explained by the higher amount of energy required by the higher turbulence intensities to be sustained. If the measurements taken were far enough removed from the cascade exit plane, it is expected that the turbulence intensities for all incidence angles would reach a common freestream value much nearer to the lowest turbulence intensity shown in Figure 26 than to the highest intensity.

51

A dramatic increase (from 2.5 percent to 8 percent) in turbulence intensity was found to occur as the incidence angle was increased from +9.32 deg to +12.44 deg for the straight trailing edge blade. This is shown in Figure 26c. However, only a moderate increase (from 2.5 percent to 3.5 percent) in turbulence intensity was observed for the same increase in incidence angle with the crenulated blade as shown in Figure 26d. With this exception, the turbulence intensity observed for the crenulated blade was comparable in magnitude to that of the straight trailing edge blade when viewed at the same incidence. To further examine the nature of the difference between the blade configurations at the higher incidence angles, the turbulence intensity distributions at the x/c = 0.05 measurement plane were compared. This measurement plane was chosen to be as close to the blade trailing edge as possible with the hope of gaining insight into the flow structure on the blade surfaces.

The turbulence intensity distribution for each blade configuration at +9.32 deg incidence is shown in Figure 27 where the center blade is located at y = 0. The +9.32 deg incidence angle distributions serve to show that although a minor reduction in peak turbulence was caused by the crenulated blades at midspan and near the z = -1.9 cm span location, the distributions are very similar in shape and magnitude. This is contrasted with the very different turbulence distributions between the blade configurations at the +12.44 deg incidence angle. These distributions are shown in Figure 28 where the center blade is located at y = 0. The turbulence distribution for the straight trailing edge blade (Figure 28a) dominates that portion of the measurement window which lies on the suction side of the blade trailing edge (below y = 0). This region is characterized by widespread unsteady velocity fluctuations that have magnitudes ranging from 24 to 32 percent of the mean flow velocity. Comparing this distribution to the crenulated blade turbulence intensity distribution in Figure 28b reveals that the crenulated blade inhibited the generation of turbulence in terms of magnitude, and spatially as well.

The turbulence intensity distribution for the straight trailing edge blade also shows that much of the identity of the passage vortices has been smeared at the +12.44 deg incidence. This smearing is also evident to a lesser extent in the corresponding total pressure loss distribution (Figure 23a). This points to a possible cause for the sudden rise in turbulence intensity. The increase in turbulence intensity may have been caused by the same phenomenon observed by Tang et al. (1991). They observed at +11.5 deg incidence, that a high blade loading near the leading edge caused strong interactions between the corner vortex and the horseshoe vortex which led to vortex breakdown and resulted in high losses. It was found in the present study however that in contrast to the straight trailing edge blades, the crenulated blades may have precluded vortex breakdown as its identity is still well-defined in the turbulence intensity distribution. This in turn led to a mitigation of the losses at the highest incidence angle.

Wake Velocity Deficit. The wake velocity deficit measurements were taken at the five measurement planes for each blade configuration at the four incidence angles. The freestream velocity in Equation (8) was taken to be the arithmetic mean of the velocities that were in the 75th percentile of all velocity measurements taken. The results are expressed as the wake velocity deficit and are shown in Figure 29. Figures 29a and 29b show at the highest incidence angle that the wake velocity deficit initially increased to a maximum and then decreased as the wake developed downstream of the cascade. This decrease is particularly noticeable with the straight trailing edge blade. At the lower three incidence angles, the trend was a very gradual increase in wake velocity deficit. The difference in trends is due to the relative magnitudes of the wake velocity deficit. A wake with a higher velocity deficit mixes more vigorously with the freestream causing a higher rate of mass entrainment into the wake which serves to dissipate the wake more rapidly. Although a high wake velocity deficit indicates a high rate of mixing, it also indicates that less mixing has occurred upstream of the location at which it was evaluated. If the

measurement plane were far enough removed from the cascade exit, the wake velocity deficit for each blade configuration at all incidence angles would approach zero as the wake velocity recovered to the freestream velocity. It can also be seen in Figures 29a and 29b for all incidence angles and measurement planes that the crenulated blades had a lower wake velocity deficit than the straight trailing edge blades. This demonstrates the enhanced wake mixing effect (i.e., more mixing has occurred) of the crenulated blades relative to the straight trailing edge blades.

The wake velocity deficit results show that the degree of wake mixing enhancement is dependent on the magnitude of the wake velocity deficit. The magnitude of the wake velocity deficit is in turn dependent on the incidence angle. A comparison of Figures 29c and 29d provides an indication of the degree of enhancement that was observed at the various incidence angles. It can be seen from these figures that the degree of wake mixing enhancement increased substantially with incidence angle. The degree of wake mixing erhancement of the crenulated blades based on ^he wake velocity deficit results at the x/c = 0.56 measurement plane is quantified in Table 10.

Table 10. Degree of Wake Mixing Enhancement Based on the Wake Velocity Deficit

i (deg)	Wake Velocity Deficit (%)		Enhancement (%)
	Straight TE	Crenulated TE	$-(\Delta WVD/WVD_{st})$
-1.08	2.27	2.05	9.7
+4.49	3.46	3.02	12.7
+9.32	5.63	4.49	20.2
+12.44	10.48	6.25	40.4

The comparison made in Table 10 shows that although enhanced wake mixing was most substantial at the higher incidence angles, the degree of enhancement at the lower incidence angles was also significant.

As stated earlier, the wake velocity deficit determination relied on an approximated value of the freestream velocity. The validity of this approximation is demonstrated by the total pressure loss distributions (Figures 20 - 23). The freestream velocity can be taken to be that velocity which is present at the locations in the measurement plane which have nearly zero total pressure losses. The freestream velocity was approximated by calculating the arithmetic mean of the velocities which lie in the 75th percentile of all velocities in the measurement plane. It follows then that the approximation is accurate only if at least 25 percent of the measurement plane has total pressure losses of nearly zero. Inspection of Figures 20 - 23 reveals that only the straight trailing edge blade at +12.44 deg incidence (Figure 23a) challenges the validity of the freestream velocity approximation. This is revealed by approximating the fraction of the measurement plane area that has nearly zero losses. This area is seen in Figure 23a to be that which lies above $y = 0.34$ cm and is equal to 34,200 cm². The total area of the measurement plane is seen to be 129,200 cm². This corresponds to $34,200/129,200 \approx 26$ percent of the measurements were taken in the freestream. The approximation is thus shown to be valid at the $x/c \leq 0.56$ measurement planes. However, as a wake develops its width increases which further challenges the validity of the approximation. Therefore, the approximated value of the freestream velocity may be slightly less than the actual freestream velocity further downstream. The wake velocity deficit results will be supported by the determination of the outlet velocity variance which also quantifies the strength of the wake. A benefit of the outlet velocity variance compared to the wake velocity deficit is that the outlet velocity variance does not rely on an approximation of the freestream velocity. It will also be shown that the outlet

55

velocity variance is more sensitive to the wake mixing process than is the wake velocity deficit.

Outlet Velocity Variance. The outlet velocity variance measurements were taken at the five measurement planes for each blade configuration at the four incidence angles. The results are expressed as the mass weighted outlet velocity variance and are shown in Figure 30. The results show for each measurement plane/incidence angle combination that the outlet velocity variance for the crenulated blades was less than that for the straight trailing edge blades. This result is consistent with the wake velocity deficit results. That is, the outlet velocity variance results also indicate that in general, the crenulated blades enhanced the wake mixing process with respect to the straight trailing edge blades. Also consistent with the wake velocity deficit results is that the outlet velocity variance results indicate that stronger wakes were observed at higher incidence angles for each measurement plane. This trend can be seen in Figures 30c and 30d.

Although the outlet velocity variance results show consistency with the wake velocity deficit results, its sensitivity to measurement plane location is comparable to its sensitivity to incidence angle as shown by a comparison of Figures 30a and 30b with Figures 30c and 30d. In contrast, the wake velocity deficit was found to be relatively insensitive to measurement plane location. The degree of wake mixing enhancement based on the outlet velocity variance at the $x/c = 0.05$, 0.56, and 1.37 measurement planes is shown in Table 11. Because the outlet velocity variance is sensitive to measurement plane location, three measurement planes were chosen. Comparing the outlet velocity variance based results at the $x/c = 0.56$ location with the wake velocity deficit based results in Table 10 reveals consistency between the results. That is, both results show that the degree of wake mixing enhancement due to the crenulated blades increased with incidence angle.

Table 11. Degree of Wake Mixing Enhancement Based on the Outlet Velocity Variance

i (deg)	$\bar{\sigma}^2$ (%)		Enhancement (%)
	Straight TE	Crenulated TE	$-(\Delta\bar{\sigma}^2/\bar{\sigma}^2_{st})$
x/c = 0.05			
-1.08	0.71	0.38	46.5
+4.49	1.28	0.69	38.3
+9.32	2.63	1.32	46.4
+12.44	4.67	2.39	45.4
x/c = 0.56			
-1.08	0.38	0.28	26.3
+4.49	0.69	0.46	33.3
+9.32	1.32	0.75	43.2
+12.44	2.39	1.09	54.4
x/c = 1.37			
-1.08	0.30	0.23	23.3
+4.49	0.43	0.34	20.9
+9.32	0.67	0.53	20.9
+12.44	0.95	0.63	33.7

The cause of the difference between the outlet velocity variance and the wake velocity deficit in sensitivity to measurement plane location can be made evident by comparing Equation (8) with Equation (14). Both equations contain similar forms of expressing the velocity defect (i.e., 1 minus a ratio of velocities). Equation (8) contains a mass averaged velocity term whereas Equation (14) contains a mass averaged velocity

squared term. Because a wake is known to entrain mass as it develops, the wake region is weighted more heavily as the wake develops downstream of the cascade. However, the amount of velocity defect decreases as the wake develops downstream of the cascade. With small changes in density, the amount of weighting in the mass averaging scheme (Equation (7)) is proportional to velocity. As the wake develops downstream, the velocity in the wake region increases causing the velocity defect to decrease in proportion to velocity, and at the same time the mass weighting is increased in proportion to velocity causing nearly offsetting changes in the value of the wake velocity deficit. In contrast, the outlet velocity variance decreases in proportion to the square of the velocity defect while the mass weighting causes an increase proportional to velocity. The net effect is a decrease in mass weighted outlet velocity variance proportional to the velocity defect as the wake develops downstream of the cascade.

Both the mass weighted outlet velocity variance and the wake velocity deficit provide acceptable indications of the wake strength relative to the bulk flow behind a blade. However as explained above, the mass averaged outlet velocity variance has a stronger dependence on the velocity defect of the wake than does the wake velocity deficit. Although the wake velocity deficit also depends on the velocity defect, its dependence is largely offset by the growth of the wake width or mass entrainment. A larger velocity defect implies stronger pitchwise velocity gradients. Because it is these pitchwise velocity gradients which make blade wakes undesirable, the outlet velocity variance is the most useful parameter with which to quantify the degree of wake mixing enhancement.

The degree of wake mixing enhancement results as shown in Table 11 indicate that the crenulated blades demonstrated approximately 38 to 47 percent more wake mixing very near the blades with little change with respect to incidence angle. As the wakes developed to $x/c = 0.56$, the crenulated blades demonstrated approximately 26 to 54

percent more wake mixing, the lowest value being at the lowest incidence angle and the highest value at the highest incidence angle. Further removed from the cascade exit, the crenulated blades demonstrated approximately 21 to 34 percent more mixing with the highest value at the highest incidence angle and the lowest value at the other three incidence angles. These results indicate with one exception that the degree of mixing enhancement offered by crenulated blades decreases with increasing distance from the cascade exit and increases with increasing incidence angle. The exception being that at the highest incidence angle the degree of mixing enhancement increased from $x/c = 0.05$ to $x/c = 0.56$ and then decreased from $x/c = 0.56$ to $x/c = 1.37$. However, at all incidence angles and measurement planes investigated, the crenulated blades were observed to enhance the wake mixing process.

Generalized Blade Performance

Cascade performance data is typically presented in summary form which indicates nondimensional flow deflection and losses as a function of nondimensional incidence angle. Perhaps the most widely used generalized performance curves for two-dimensional cascade flow are known as Howell's Generalized Performance Curves as reprinted by Dixon (1978). The flow deflection results and the incidence angles of this study can be expressed in nondimensional form by introducing a nominal flow deflection (ε^*) and a nominal incidence angle (i^*). The calculation of these nominal values can be found in Appendix A. Using these nominal values, the relative incidence and relative deflection are defined as

$$\text{Relative Incidence} = \frac{i - i^*}{\varepsilon^*}$$

$$\text{Relative Flow Deflection} = \frac{\varepsilon}{\varepsilon^*}$$

$$\text{where } i^* = 12.24 \text{ deg}$$

$$\varepsilon^* = 36.89 \text{ deg}$$

The nominal flow deflection, as applied to two-dimensional flow, represents an analytical prediction corresponding to 80 percent of the maximum deflection possible before stall occurs. As discussed in the static pressure rise results, stall was suspected to be approached at a flow deflection very near the nominal flow deflection. This observation shows that the correlation between the nominal flow deflection and the stalled flow condition for two-dimensional flow is not valid for three-dimensional flow. However, the nominal flow deflection and its corresponding incidence angle adequately serve as explicit reference values for the purpose of nondimensionalizing the performance results of this three-dimensional flow study. The off-design performance results of this study, derived from the flow deflection results and the total pressure loss results are presented summarily in Figure 31 for each measurement plane. Excluding the wake mixing benefits of the crenulated blades, the off-design performance curves show at a glance the impact on performance of introducing crenulations to the blade trailing edge. It is shown that crenulations were found to mitigate the losses at high incidence angles and may have delayed the onset of stall. The cost of crenulations however was found to be reduced flow deflection at all incidence angles tested.

VI. Conclusions and Recommendations

Conclusions

At all incidence angles tested, crenulated blades were found to significantly enhance the wake mixing process compared to that of straight trailing edge blades. The effect of the enhancement is to reduce non-axial gradients in the flow downstream from the blades. With respect to axial flow compressors, this effect is desirable if a specified amount of uniformity is required by a subsequent engine component or stage. The degree of wake mixing enhancement ranged from 21 percent to 54 percent. The value of 21 percent was found at the furthest downstream location ($x/c = 1.37$) from the blade trailing edge. This value would be the more representative value related to the improvement of combustor inlet flow uniformity. The higher values of wake mixing enhancement were found at locations much nearer the blade trailing edge. This introduces the prospect that crenulations may be useful relative to interstage effects.

The wake mixing enhancement was found to be the result of a trade-off. The desirable wake mixing characteristics were achieved at the cost of flow deflection. The effect of using crenulated blades was to reduce the flow deflection by 1.9 deg at -1.08 deg incidence, by 2.4 deg at +4.49 deg incidence, by 2.6 deg at +9.32 deg incidence, and by 3.7 deg at +12.44 deg incidence. Consistent with the flow deflection trade-off, static pressure rise was also sacrificed except at the highest incidence angle (+12.44 deg). This exception will be addressed separately.

Although the wake mixing enhancement sacrificed deflection, it did not sacrifice pressure losses. At the incidence angles from -1.08 deg to +9.32 deg, the crenulated blades had virtually no impact on total pressure losses. However, to regain the flow deflection lost by the crenulated blades, the crenulated blades would be required to operate at a higher incidence than the straight trailing edge blades. Increasing the

61

incidence angle would result in a corresponding increase in total pressure losses. Therefore, crenulated blades which turn the flow as much as straight trailing edge blades would have higher total pressure losses than the straight trailing edge blades except possibly at incidence angles greater than +12.44 deg. At the +12.44 deg incidence angle, the crenulated blades were observed to reduce total pressure losses by 20 percent of the losses for the straight trailing edge blades.

Throughout this study, the +12.44 deg incidence angle proved to be an exception concerning the impacts of the crenulated blades on the flow through the cascade. The results, in sum, appear to indicate that at this incidence angle the straight trailing edge blades approached a stalled flow condition with a reattached fully turbulent boundary layer near their trailing edges. This highly undesirable flow condition was characterized by exceptionally high losses and turbulence, with reduced pressure rise and deviation angle. However, the crenulated blades showed no signs of large scale flow degradation at this incidence angle; instead they enhanced the wake mixing by 45 percent, reduced the outlet turbulence intensity by a factor of 2, and reduced total pressure losses by 20 percent. At the maximum incidence angle tested, the performance of the crenulated blades (neglecting their superior wake mixing characteristics) surpassed that of the straight trailing edge blades. It appears that crenulated blades may be aerodynamically robust in that they inhibit the onset of stall on highly loaded compressor blades with strong three-dimensional flow.

Recommendations

This study made limited measurements in the blade surface boundary layers and no measurements between the blades, outside of the boundary layers. A study which made extensive measurements in these areas of the flow would provide valuable insight into crenulation impact on vortex structure and breakdown, and boundary layer development

and transition. An understanding of these phenomena would help in optimizing crenulated blade applications.

In this study, stall appears to have been approached at +12.44 deg incidence for the straight trailing edge blades. A further study which determines the stall incidence angle for the crenulated blades would help quantify the robustness of the crenulated blades at high loadings.

Spacy (1993) has studied the performance of various crenulation geometries at a single incidence angle. A study which investigates the off-design performance of the optimum geometry would provide insight into the overall performance of this optimum geometry.

Although the positive stall incidence was approached, the values of the negative stall incidence and minimum loss incidence are yet unknown. It would be useful to examine the negative incidence angles so that the influence of the crenulations on the negative stall condition and minimum loss condition could be assessed.

References

Allison, Dennis M. Design and Evaluation of a Cascade Test Facility. MS Thesis GAE/AA/81D-2. School of Engineering, Air Force Institute of Technology (AU), Wright-Patterson AFB, OH, June 1982.

Cohen, H., G. F. C. Rogers, and H. I. H. Saravanamuttoo. Gas Turbine Theory (Third Edition). New York: John Wiley and Sons, 1987.

DeCook, S. J., P. I. King, and W. C. Elrod. "Wake Mixing and Performance of a Compressor Cascade with Crenulated Trailing Edges," Journal of Propulsion and Power, Volume 9, Number 2: 293-300 (March-April 1993).

DeCook, S. J. Experimental Investigation of Trailing Edge Crenulation Effects on Losses in a Compressor Cascade. MS Thesis GAE/ENY/91D-1. School of Engineering, Air Force Institute of Technology (AU), Wright-Patterson AFB OH, December 1991.

Dixon, S. J. Fluid Mechanics, Thermodynamics of Turbomachinery. Oxford: Pergamon Press, 1978.

Erwin, John R., and James C. Emery. Effect of Tunnel Configuration and Testing Technique on Cascade Performance. NACA TN-2028. Washington: National Advisory Committee for Aeronautics, 1950.

Eschbach, Ovid W. and others. Handbook of Engineering Fundamentals. New York: John Wiley & Sons, 1975.

Fottner, L. "Review on Turbomachinery Blading Design Problems," Blading Design for Axial Turbomachines. AGARD-LS-167. Neuilly sur Seine: Advisory Group for Aerospace Research and Development, 1989.

Freymuth, Peter. A Bibliography of Thermal Anemometry. St. Paul, MN: TSI, Inc., 1982.

Gostelow, J. P. Cascade Aerodynamics. Oxford: Pergamon Press, 1984.

Kang, Shun, and C. H. Hirsch. "Three Dimensional Flow in a Linear Compressor Cascade at Design Conditions," ASME Paper 91-GT-114, Orlando, FL, June 1991.

Lieblein, Seymour. "Experimental Flow in Two-Dimensional Cascades," Aerodynamic Design of Axial Flow Compressors Revised, edited by Irving A. Johnson and Robert O. Bullock. NASA SP-36 . Washington: National Aeronautics and Space Administration, 1965.

Lieblein, Seymour, G. W. Lewis, Jr., and D. M. Sandercock. Diffusion Factor for Estimating Losses and Limiting Blade Loading in Axial Flow Compressor Blade Elements. NACA RM E53D01. Washington: National Advisory Committee for Aeronautics, 1953.

PSI 8400 Pressure Scanner User's Manual. Hampton, VA: Pressure Systems, Incorporated, March 1993.

Scholz, Norbert. Aerodynamics of Cascades, translated and revised by A. Klein. AGARD-AG-220. Neuilly sur Seine: Advisory Group for Aerospace Research and Development, 1977.

Spacy, William L. II. Effects of Crenulations on Three-Dimensional Losses in a Compressor Cascade. Unpublished thesis. Graduate School of Engineering, Air Force Institute of Technology (AU), Wright-Patterson AFB OH, December 1993.

Tang, Y. P., F. Chen, M. Z. Chen. "Experimental Investigation of Vortex Structure in Corner Region of a Linear Compressor Cascade," ASME Paper 91-GT-158, Orlando, FL, June 1991.

Veesart, J. L., P. I. King, W. C. Elrod, and A. J. Wennerstrom. "Wake Mixing Improvements in a Linear Compressor Cascade with Crenulated Trailing Edges," ASME Paper 90-GT-218, Brussels, Belgium, June 1990.

Wennerstrom, Arthur J. "Vane Configuration for Fluid Wake Re-energization", United States Patent Number 4,318,669, 1982.

White, Frank M. Viscous Fluid Flow (Second Edition). New York: McGraw-Hill, Inc., 1991.
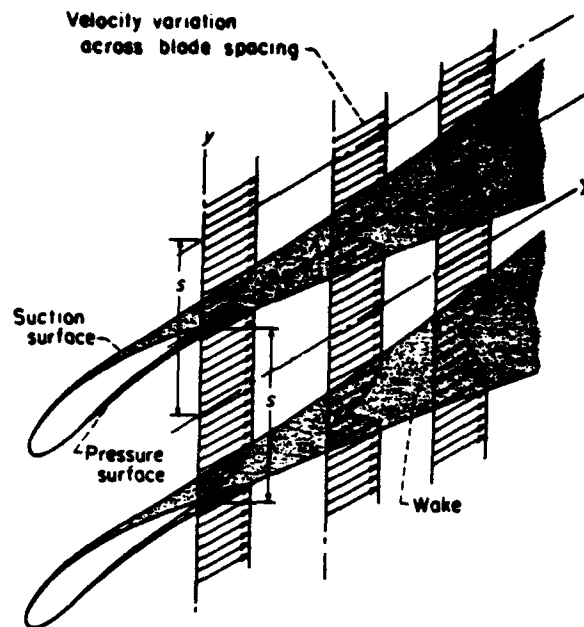
Figure 1. Blade Wake Development (Lieblein, 1965)

Figure 2. Crenulation Induced Vortices
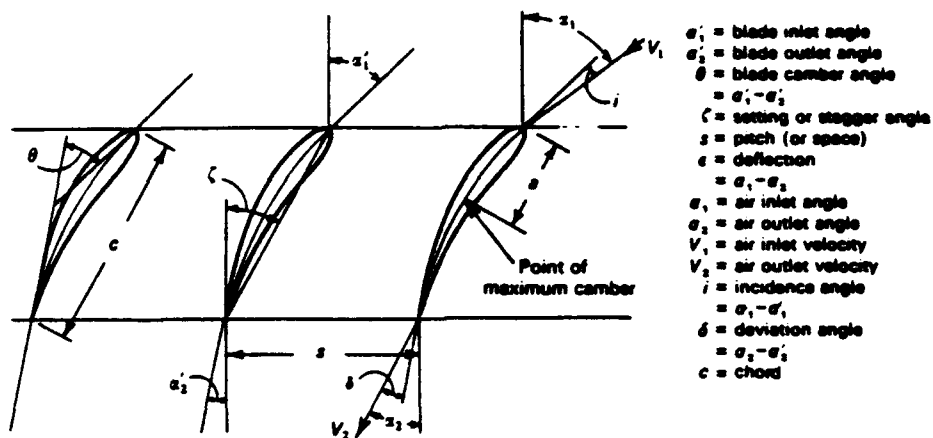
Figure 3. General Cascade Specifications (Cohen et al., 1987)
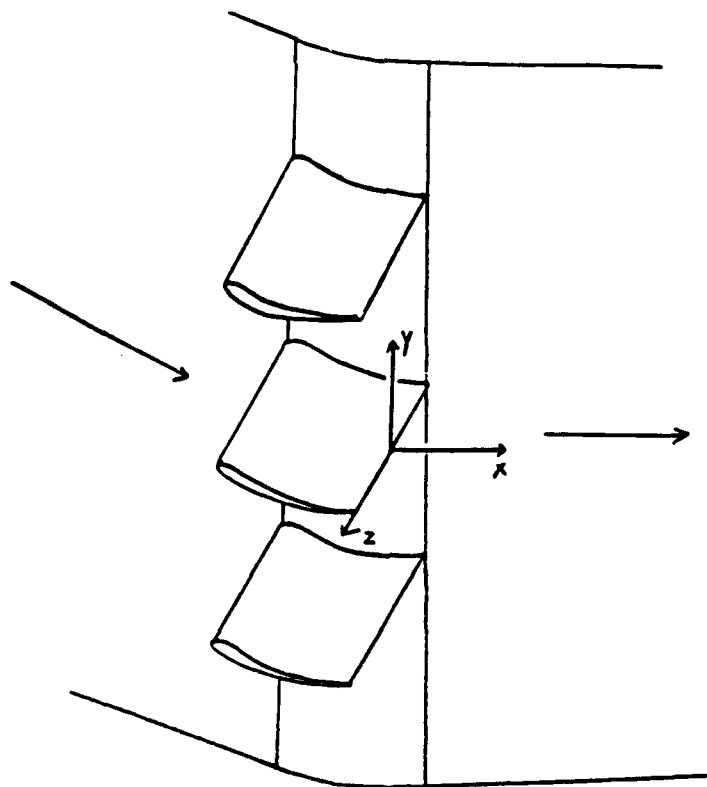
Figure 4. Cascade Coordinate System
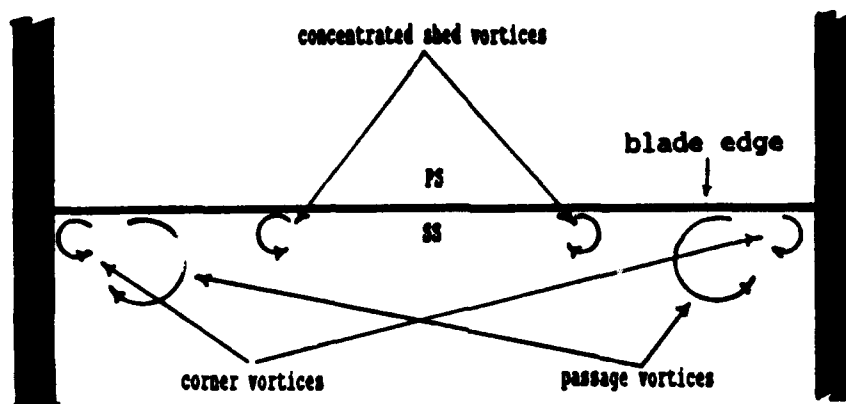
Figure 5. Three-Dimensional Flow Development (adapted from Kang and Hirsch, 1991)
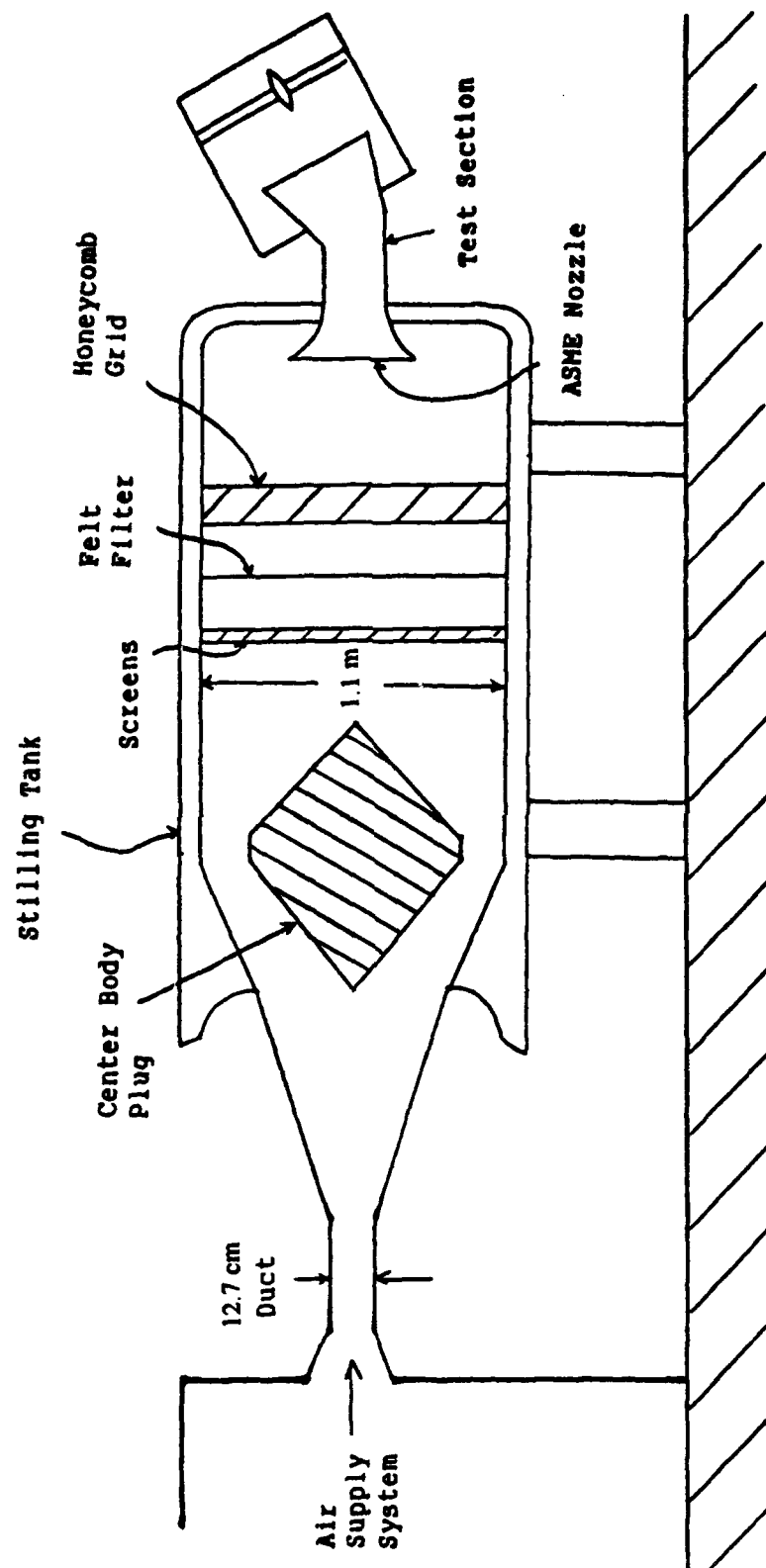
Figure 6. Air Supply System and Diffuser/Stilling Chamber
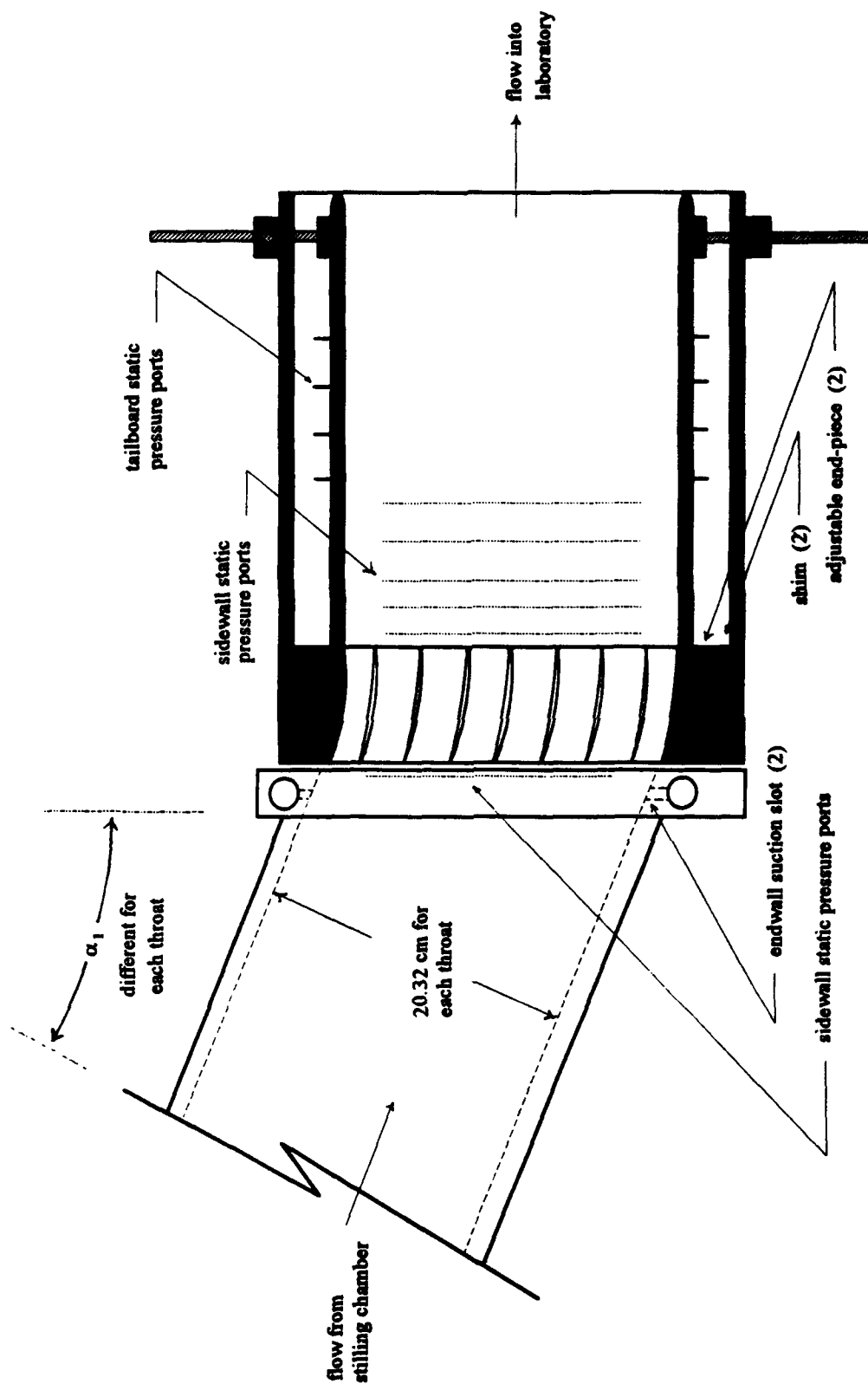
Figure 7. Throat/Cascade Test Section

0.50

0.00

0.00 0.50 1.00 1.50 2.00 2.50 3.00 3.50 4.00 4.50 5.00 5.50
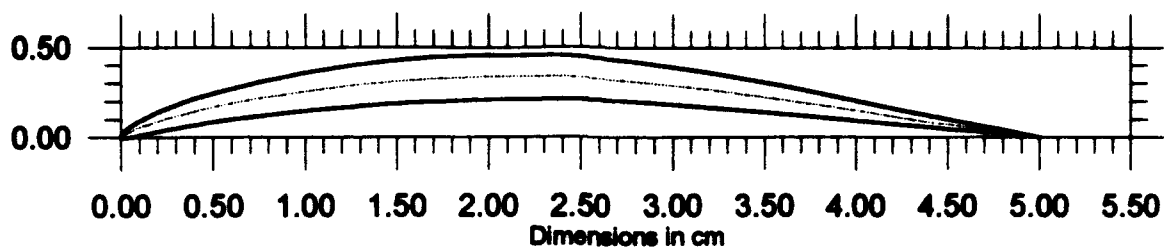
Dimensions in cm

Figure 8. Compressor Blade Profile

Leading Edge

Straight TE Blade

Trailing Edge

5.0

5.0

Crenulated Blade

1.3

1.0   0.5
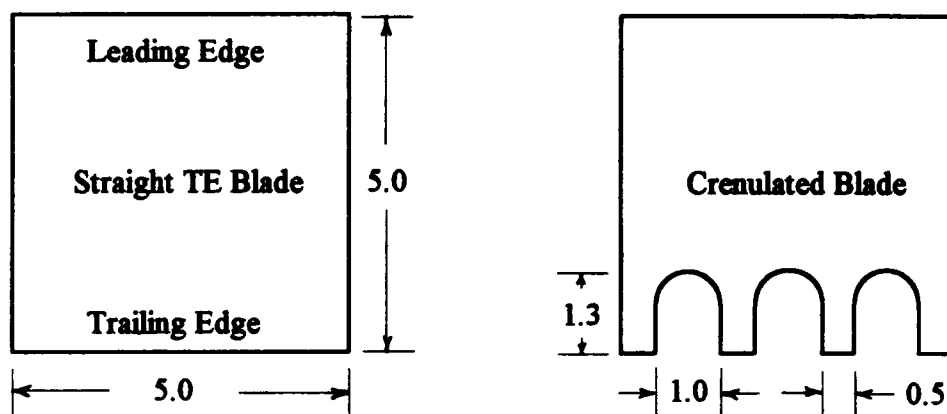
Dimensions in cm

Figure 9. Compressor Blade Planforms

71
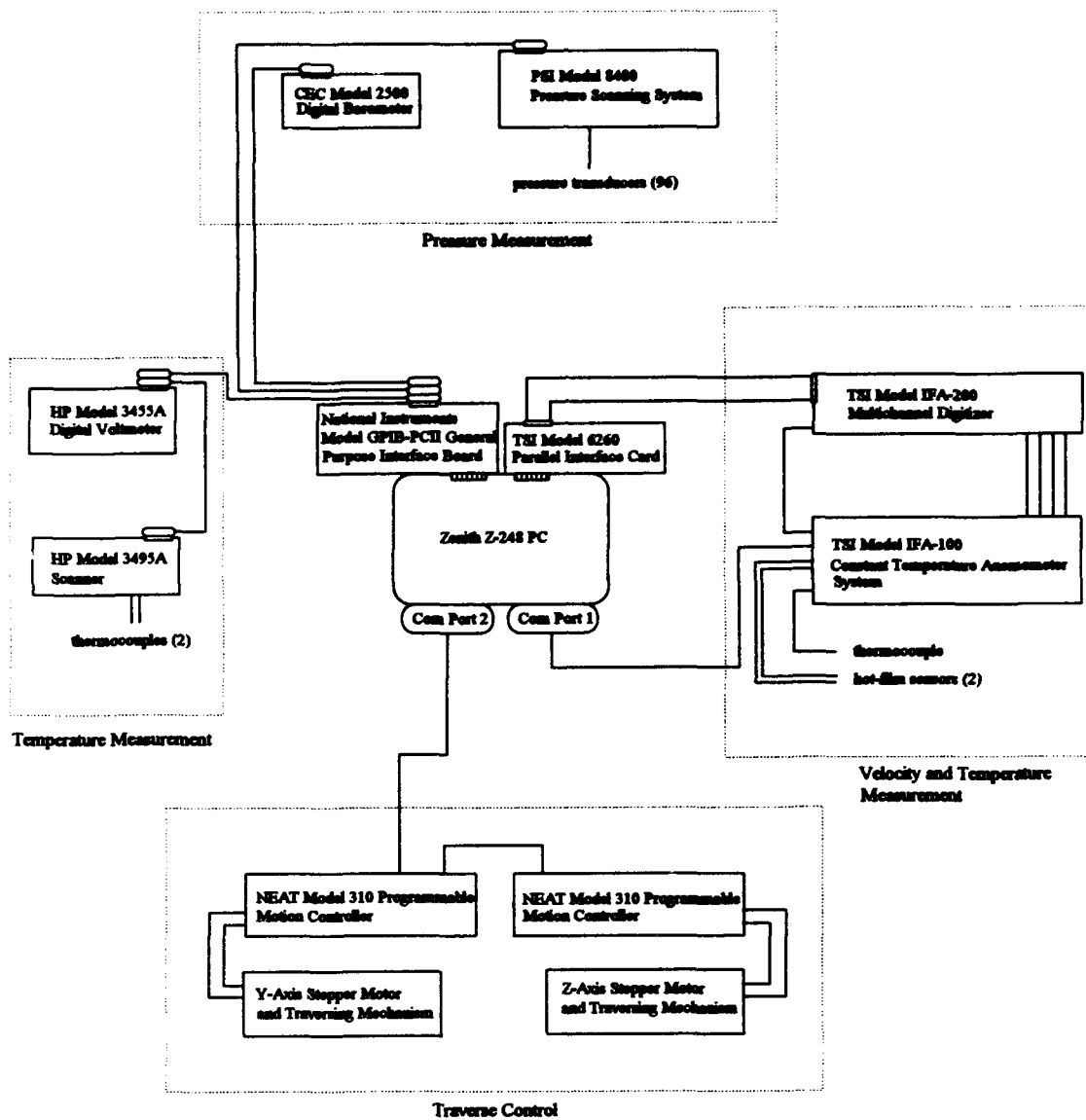
Figure 10. AFIT Cascade Test Facility Digital Data Acquisition System

TOP VIEW

|———————— 78.7 cm ————————|

SIDE VIEW
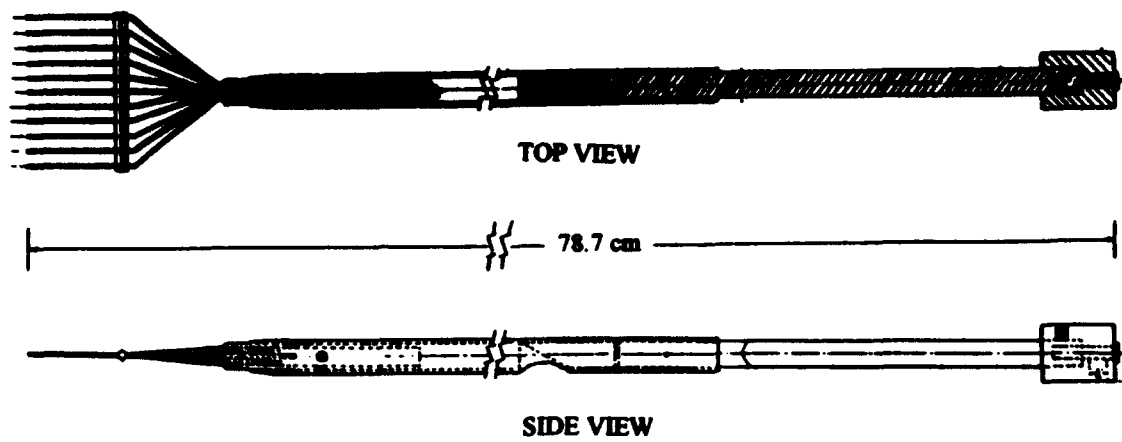
Figure 11. Total Pressure Rake

SENSOR #1

SENSOR #2
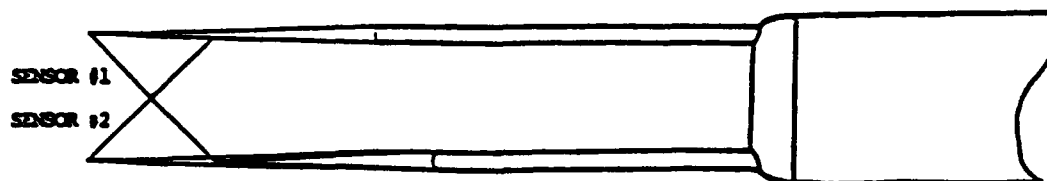
Figure 12. X-Configuration Hot-film Probe
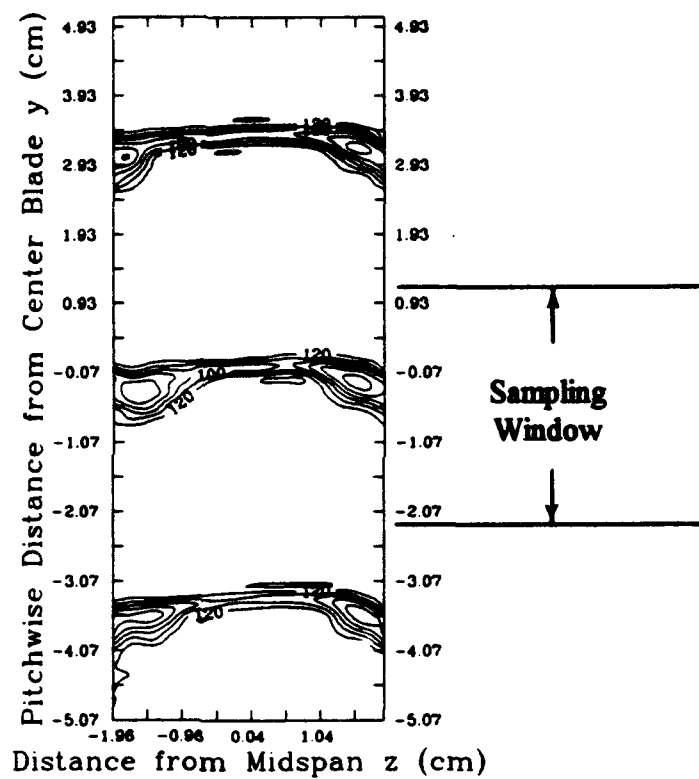
Figure 13. Initial Velocity Survey (m/s): i = +4.49 deg, x/c = 0.30
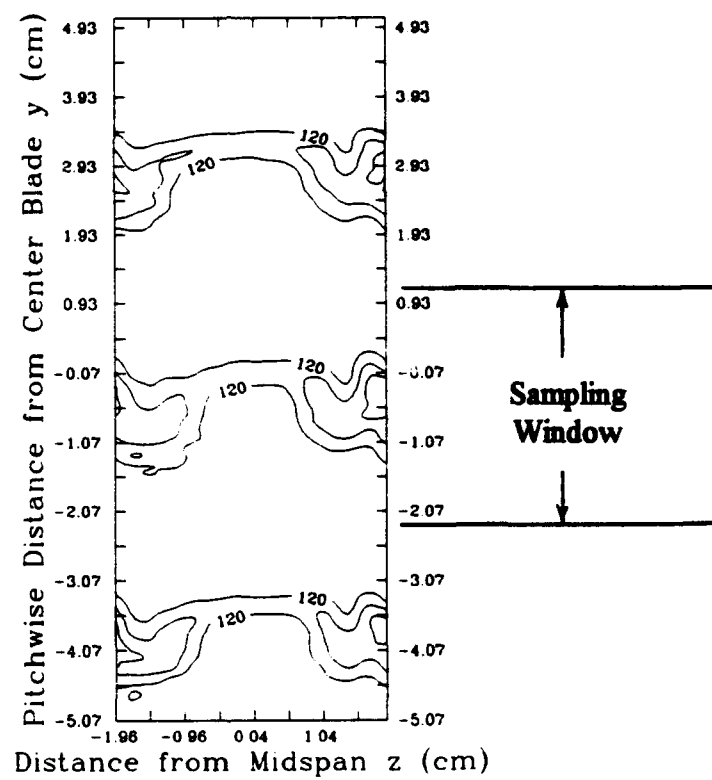
Figure 14. Initial Velocity Survey (m/s): i = +4.49 deg, x/c = 1.37
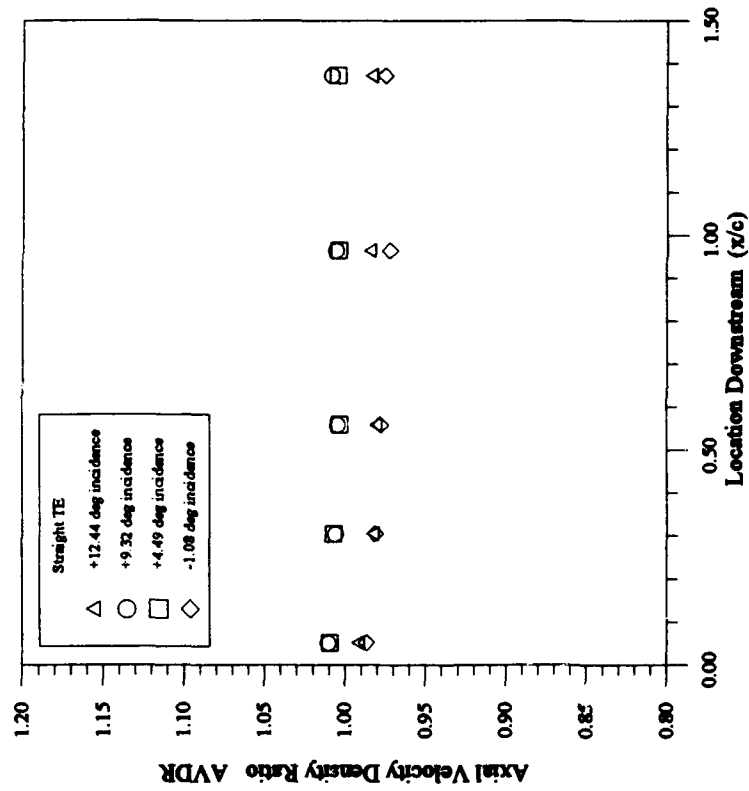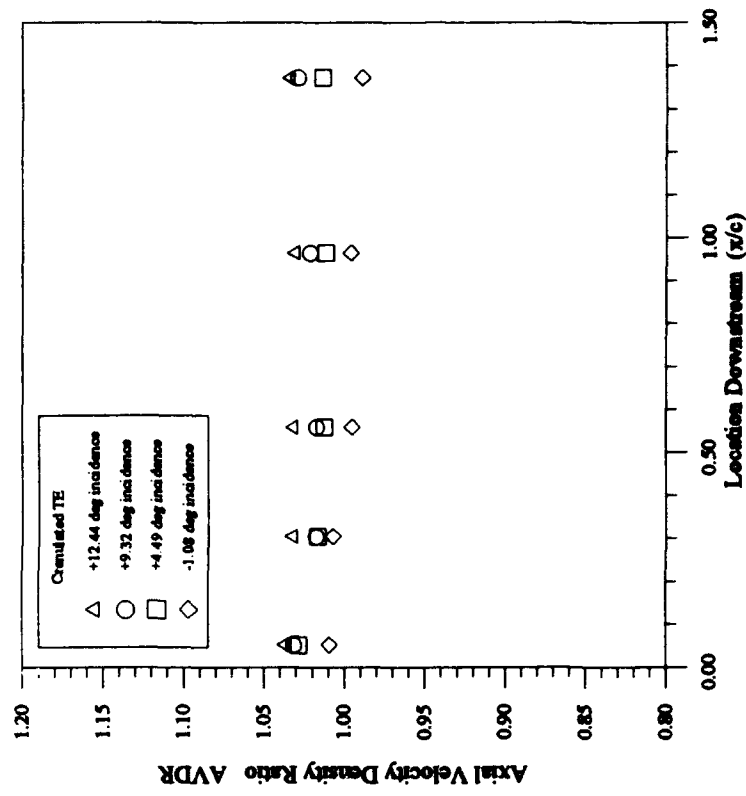
Figure 15b.

Figure 15a.

Figure 15. Axial Velocity Density Ratio
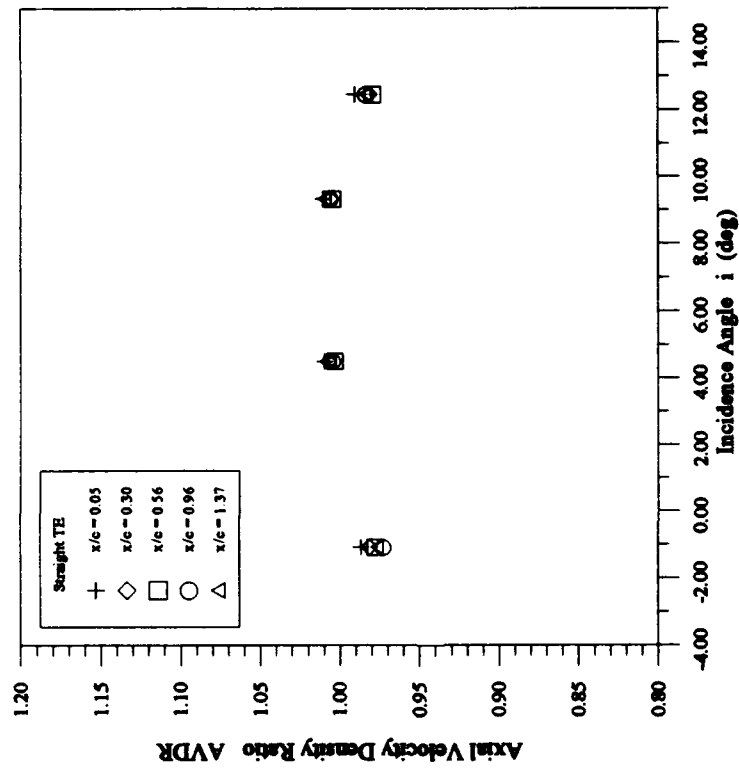
Figure 15c.
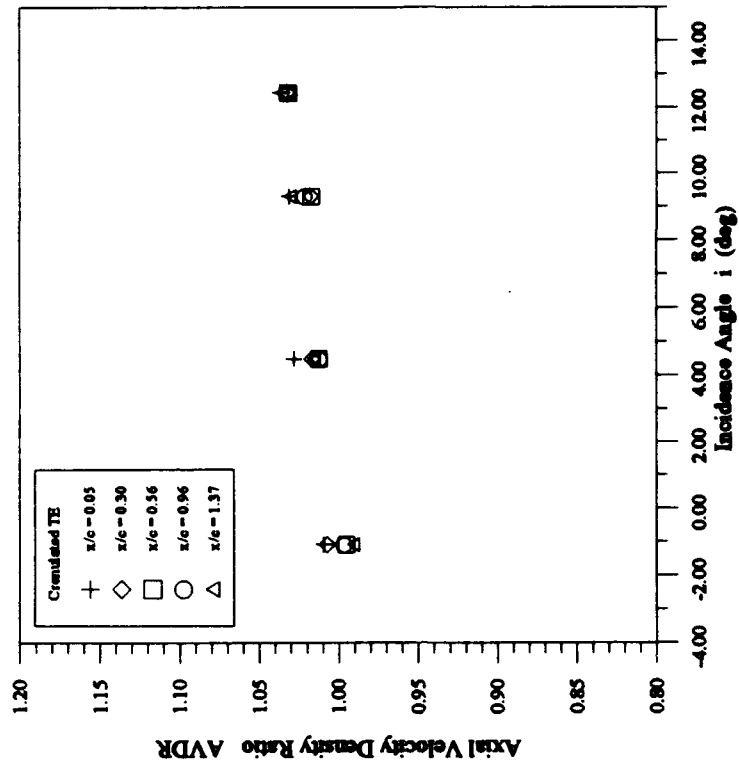
Figure 15d.

Figure 15 (cont.). Axial Velocity Density Ratio
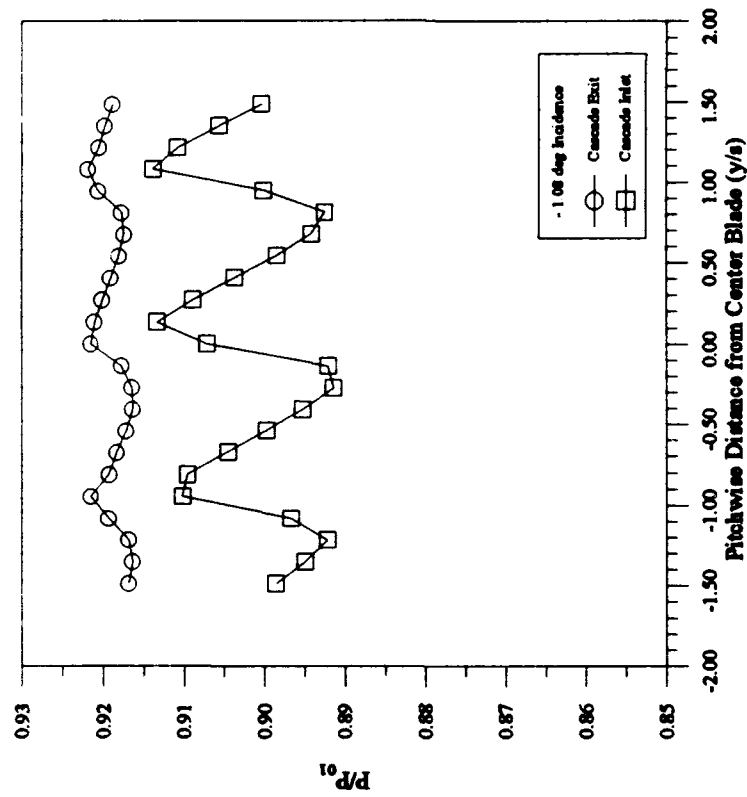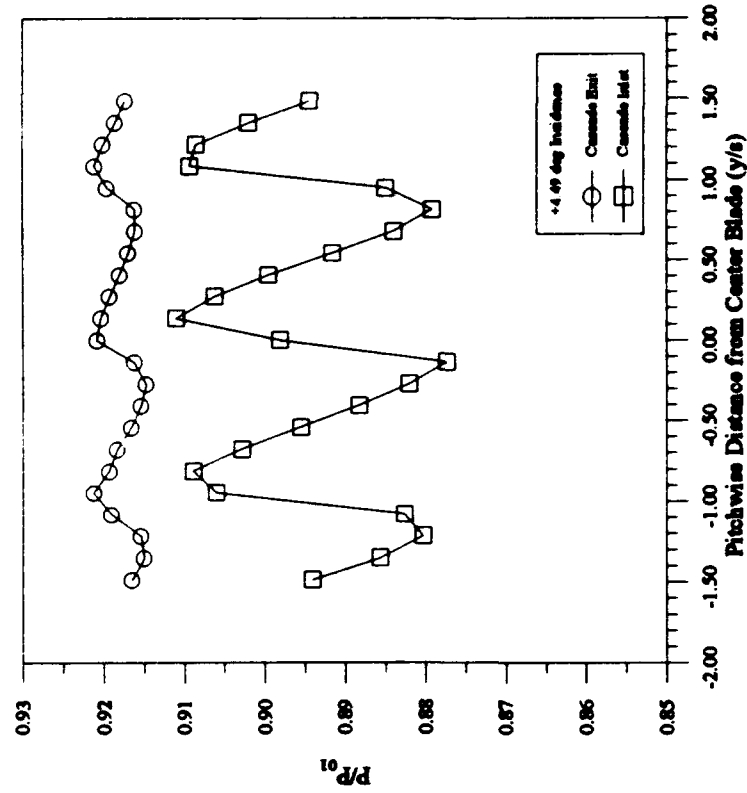
Figure 16b.

Figure 16a.

Figure 16. Inlet and Exit Static Pressure Periodicity

78
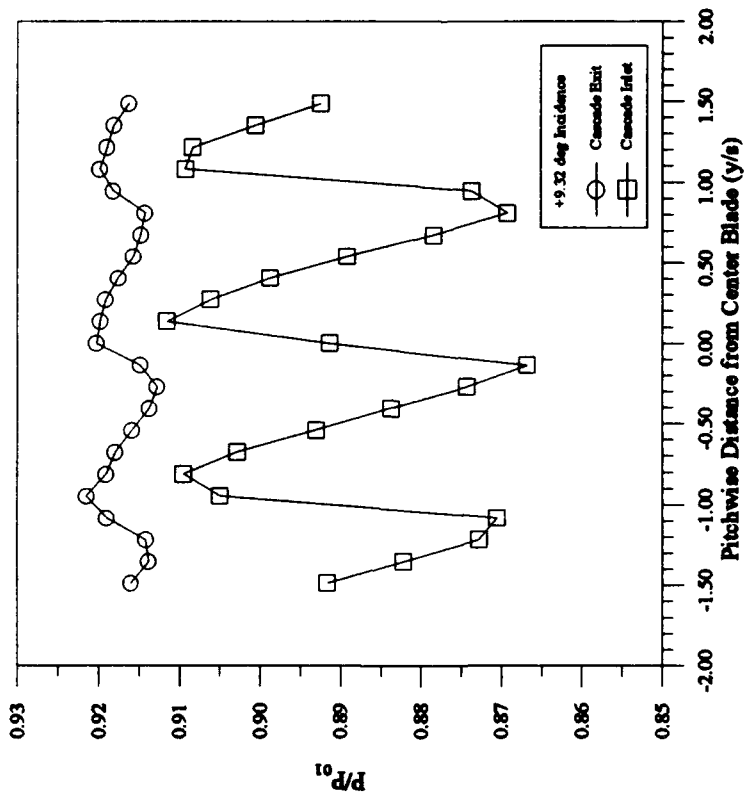
Figure 16d.

Figure 16c.

Figure 16 (cont.).   Inlet and Exit Static Pressure Periodicity
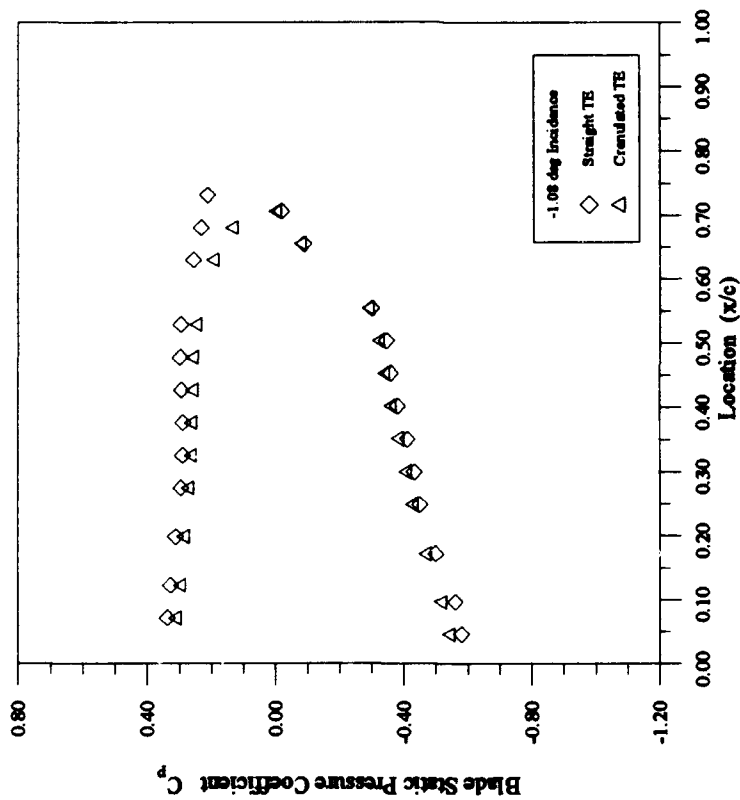
Figure 17a.
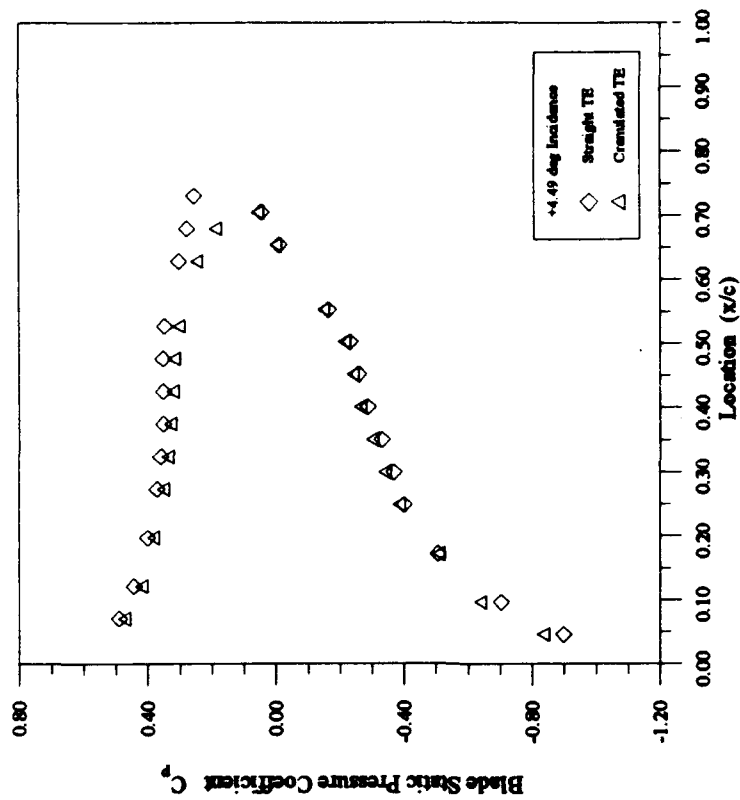
Figure 17b.

Figure 17. Blade Surface Static Pressure Distribution
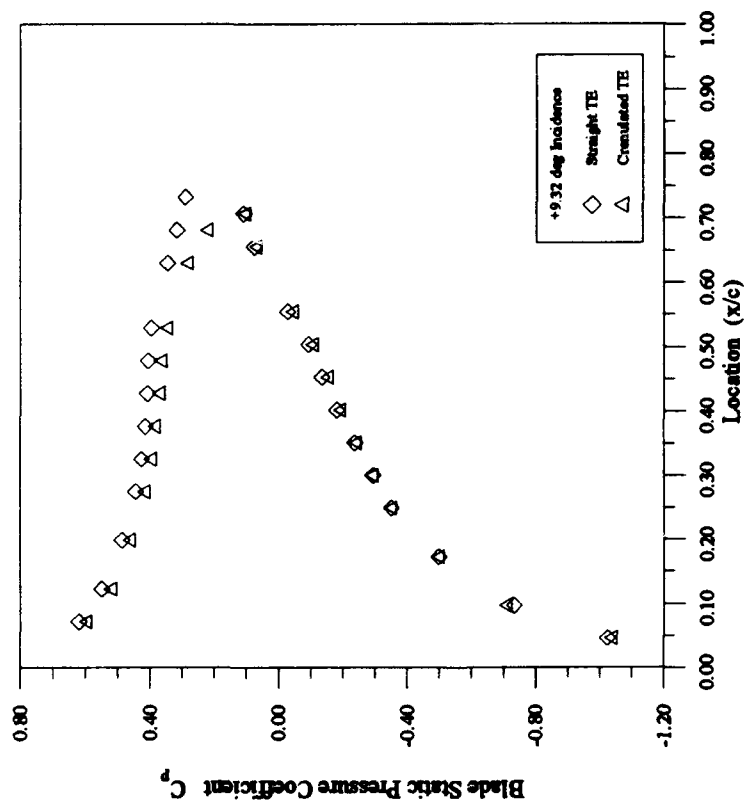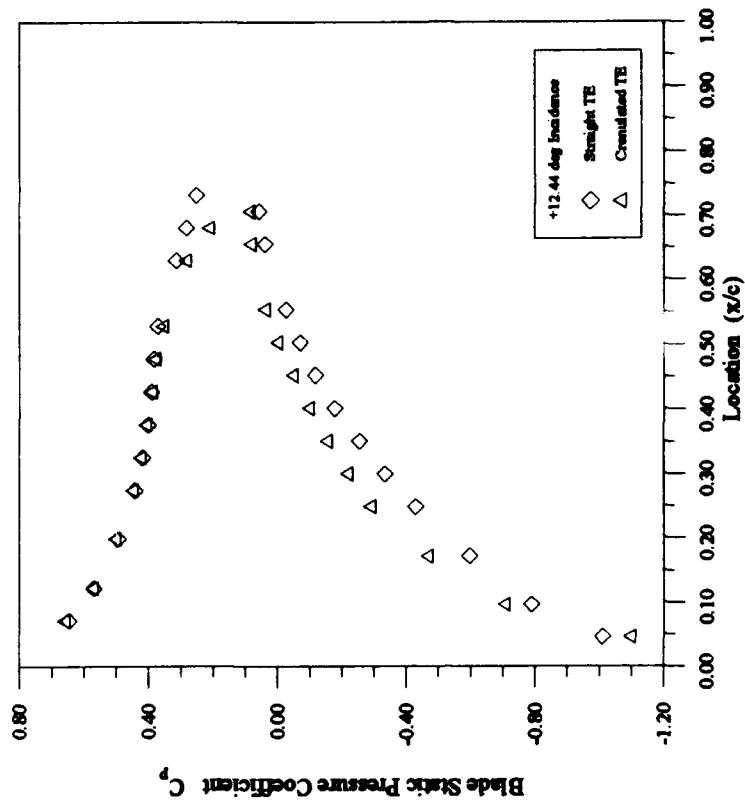
Figure 17 (cont.).   Blade Surface Static Pressure Distribution
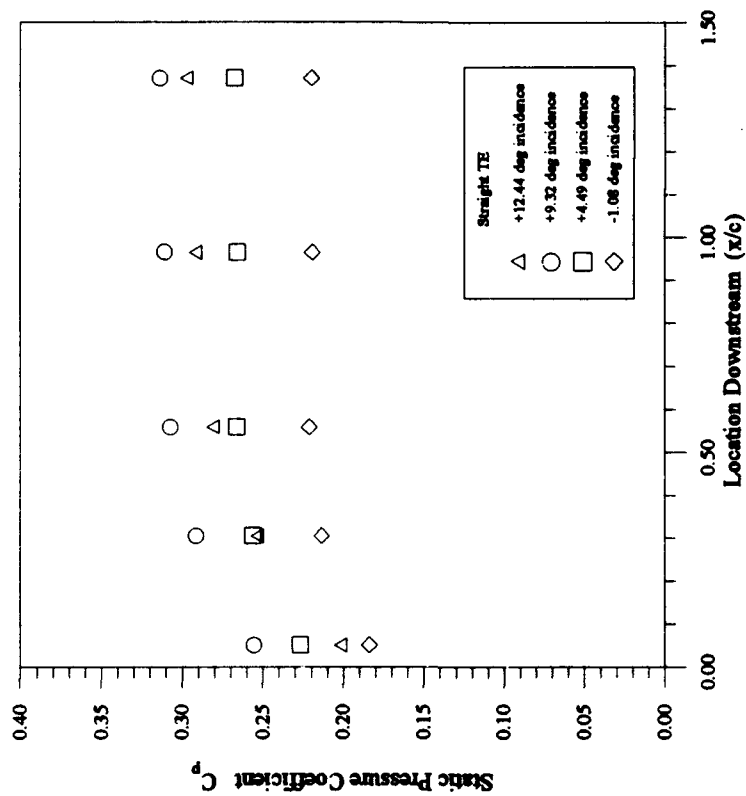
Figure 18a.
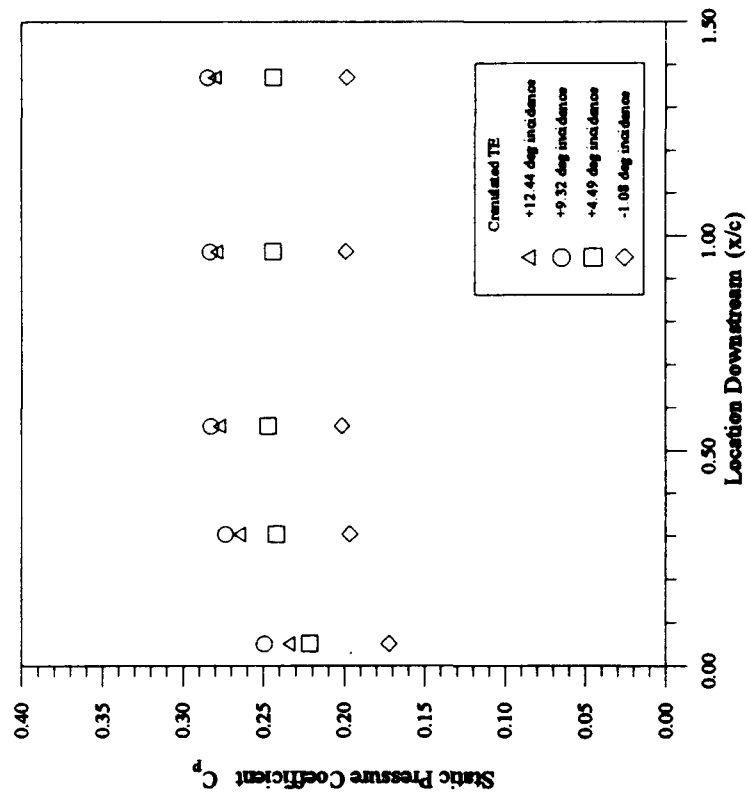
Figure 18b.

Figure 18.   Cascade Static Pressure Rise

82
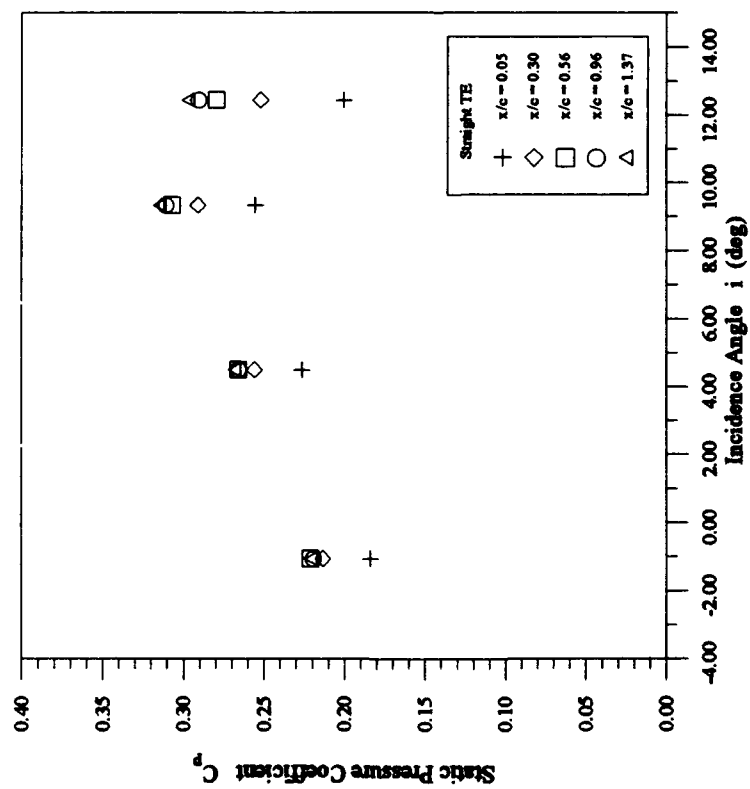
Figure 18c.

Figure 18d.

Figure 18 (cont.). Cascade Static Pressure Rise
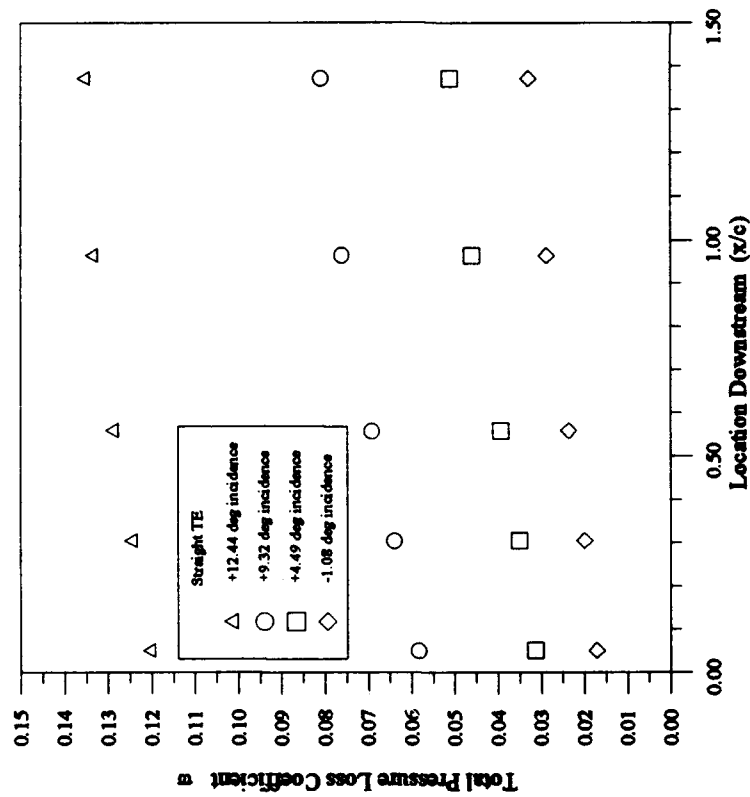
Figure 19a.
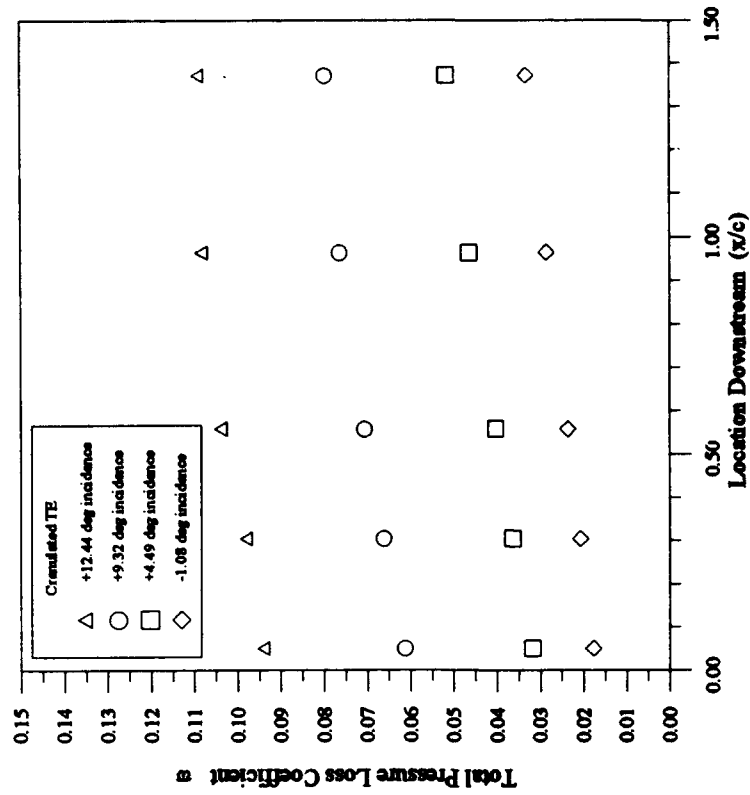
Figure 19b.

Figure 19. Total Pressure Losses (mass averaged)

84
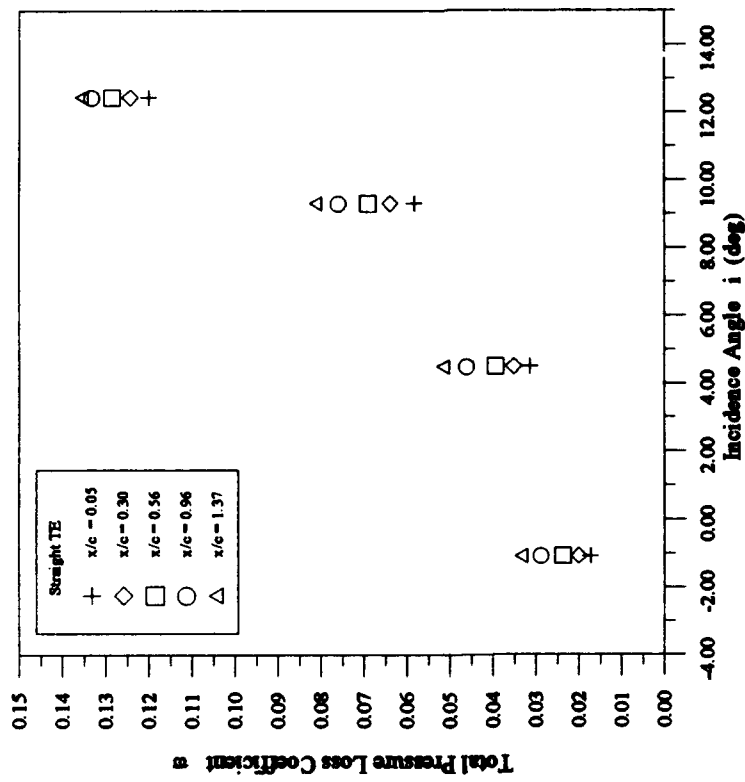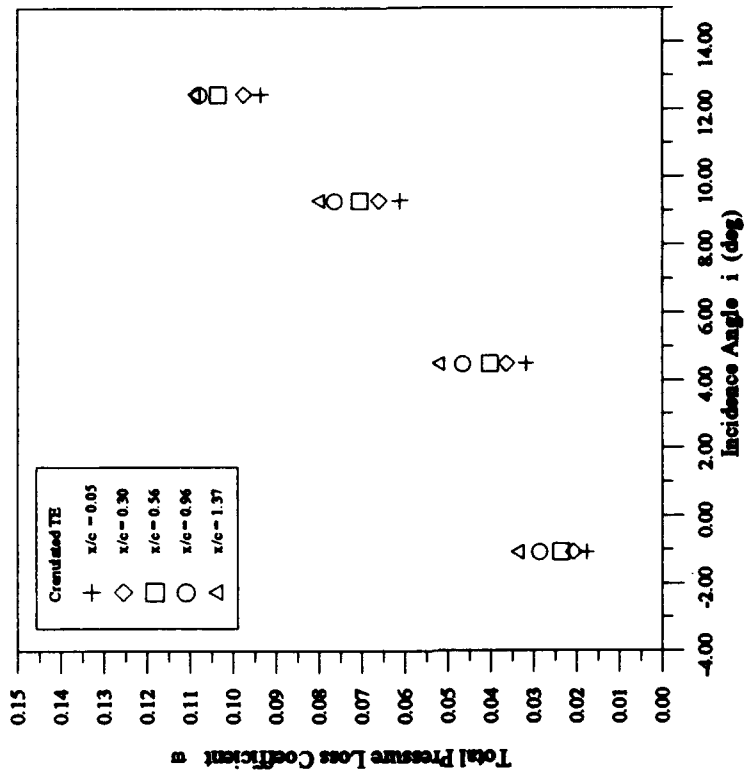
Figure 19c.

Figure 19d.

Figure 19 (cont.). Total Pressure Losses (mass averaged)

85
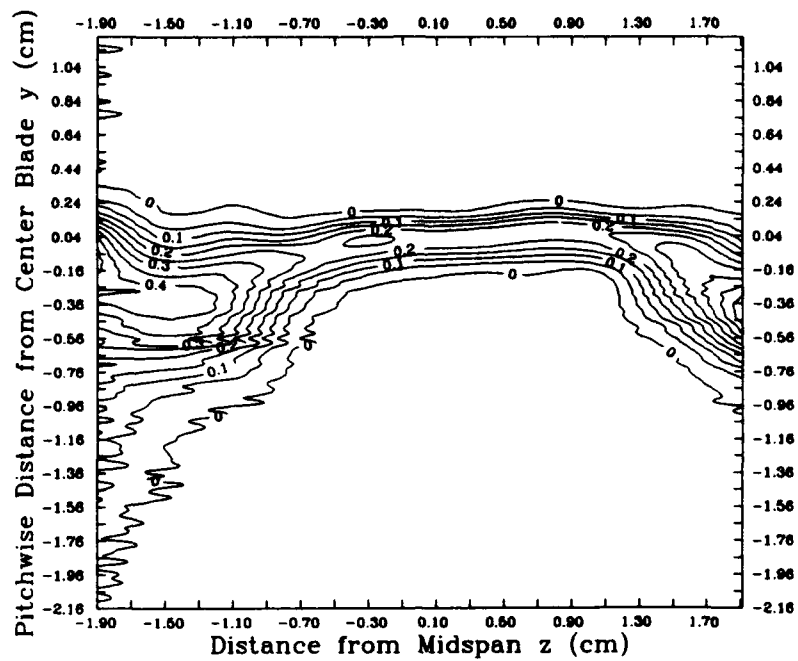
Figure 20a. Straight TE
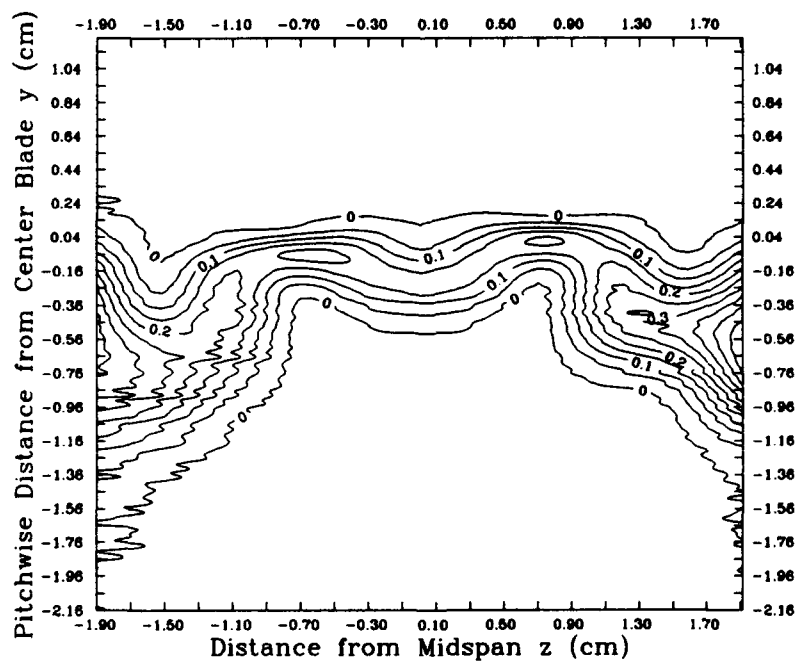
Figure 20b. Crenulated TE

Figure 20. Total Pressure Loss Distribution: $i = -1.08$ deg, $x/c = 0.56$

86
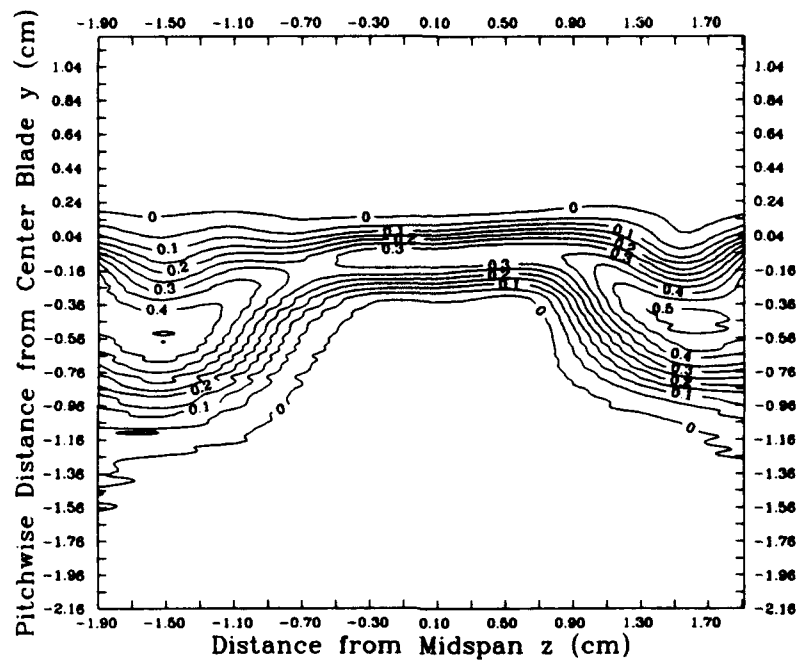
Figure 21a. Straight TE
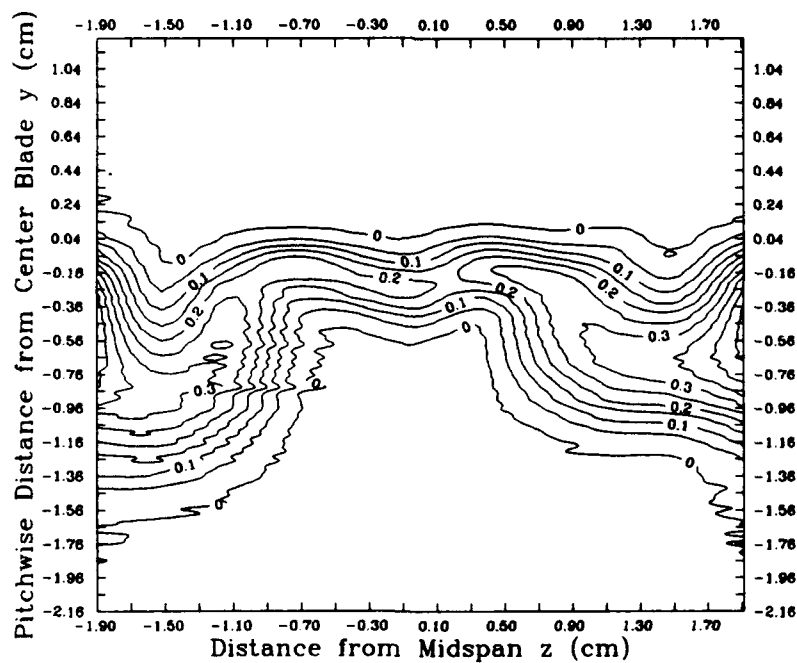
Figure 21b. Crenulated TE

Figure 21.   Total Pressure Loss Distribution: i = +4.49 deg,   x/c = 0.56
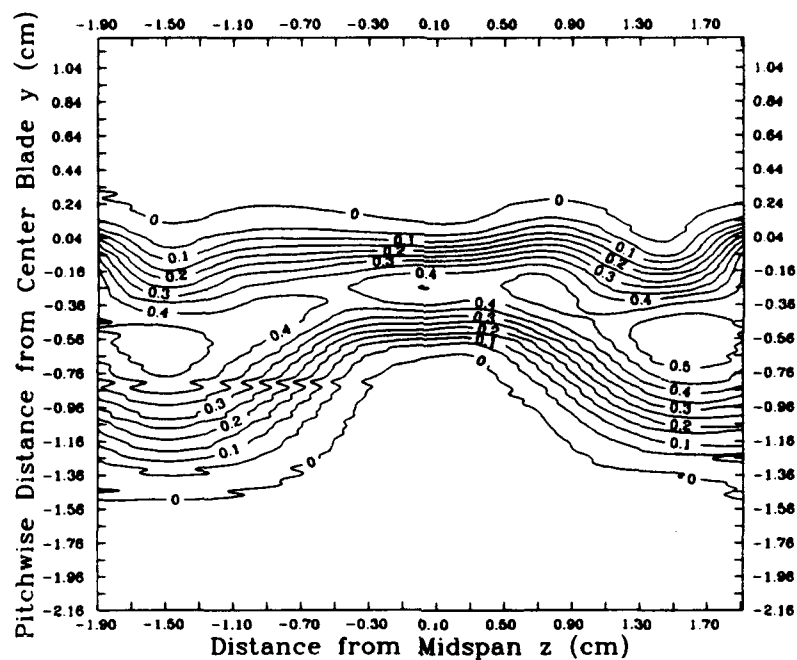
Figure 22a. Straight TE
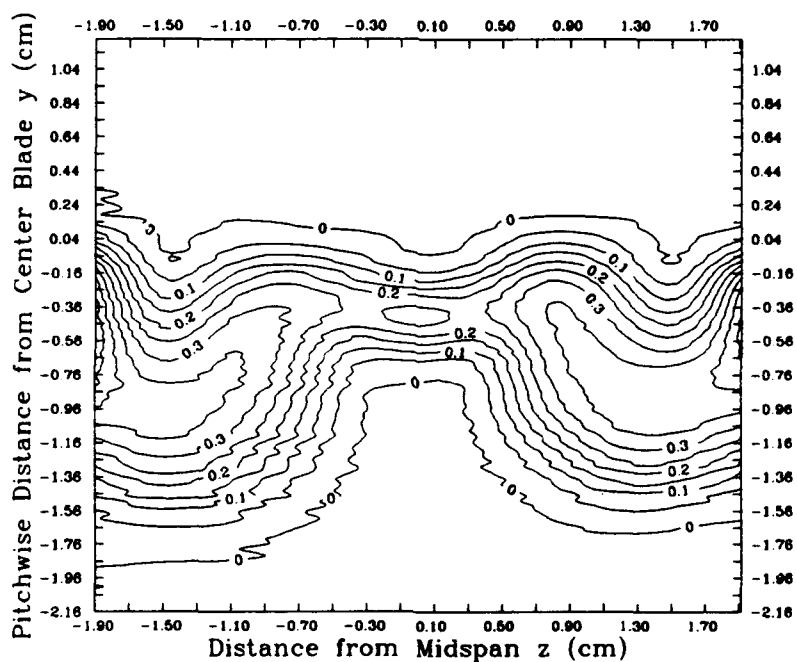
Figure 22b. Crenulated TE

Figure 22. Total Pressure Loss Distribution: $i = +9.32$ deg, x/c = 0.56
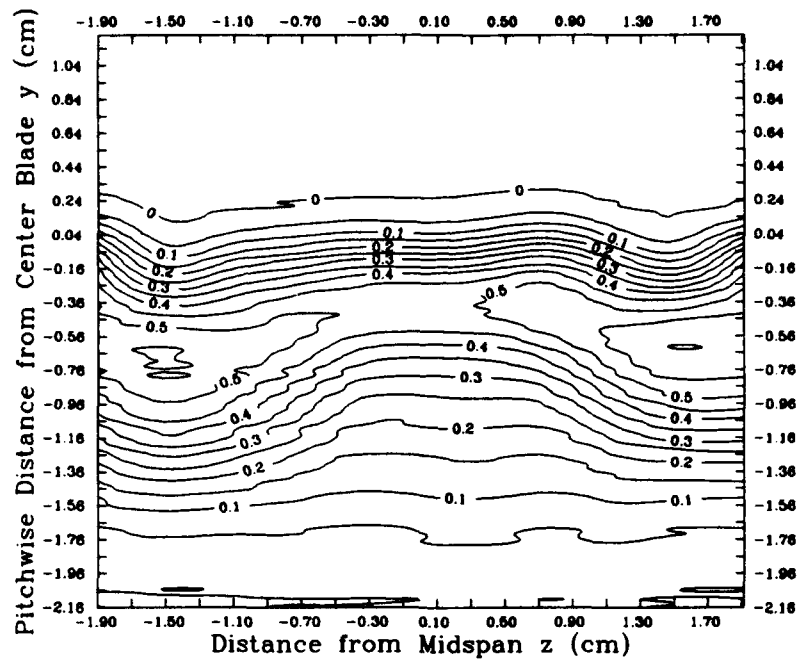
Figure 23a. Straight TE
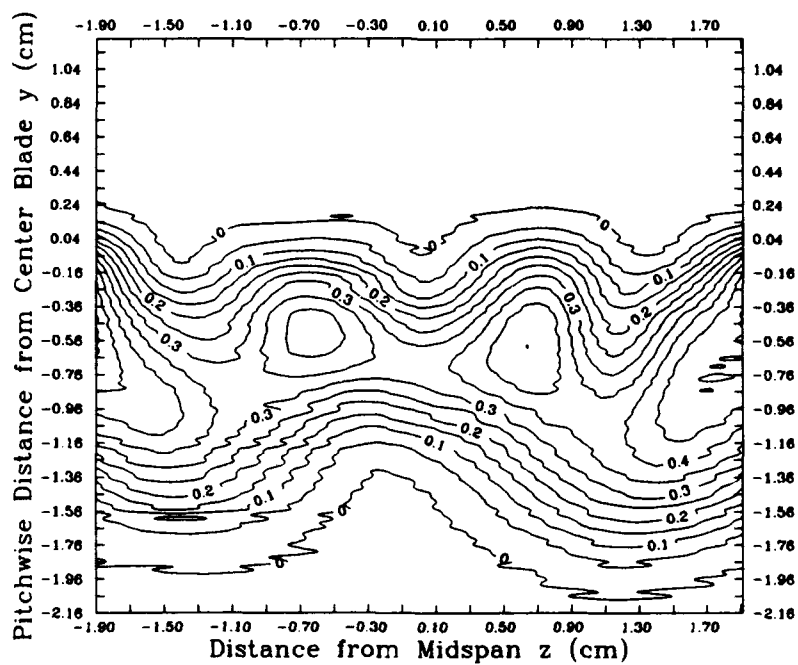
Figure 23b. Crenulated TE

Figure 23. Total Pressure Loss Distribution: *i* = +12.44 deg, x/c = 0.56
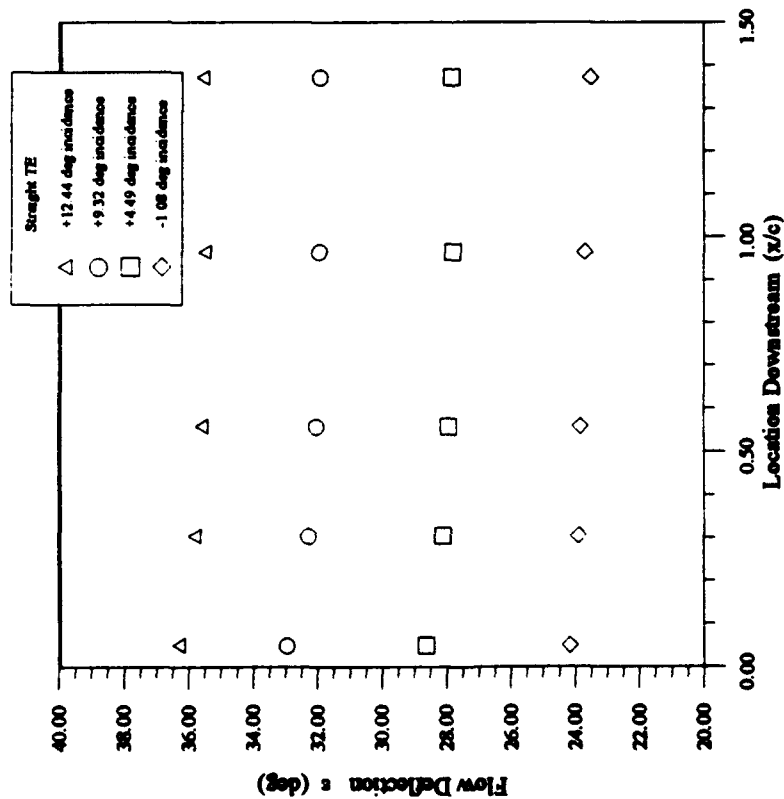
Figure 24a.
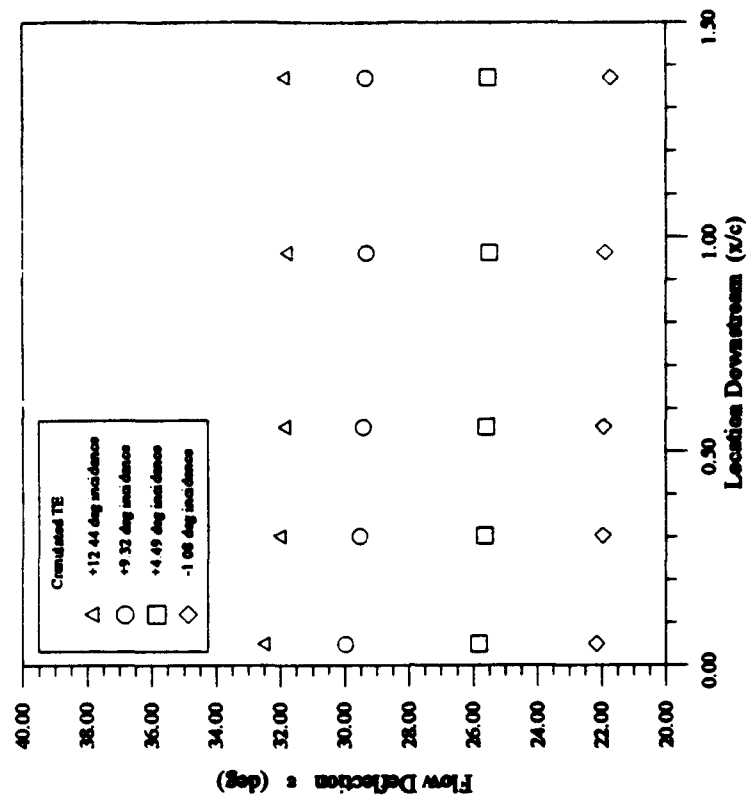
Figure 24b.

Figure 24. Flow Deflection (mass averaged)
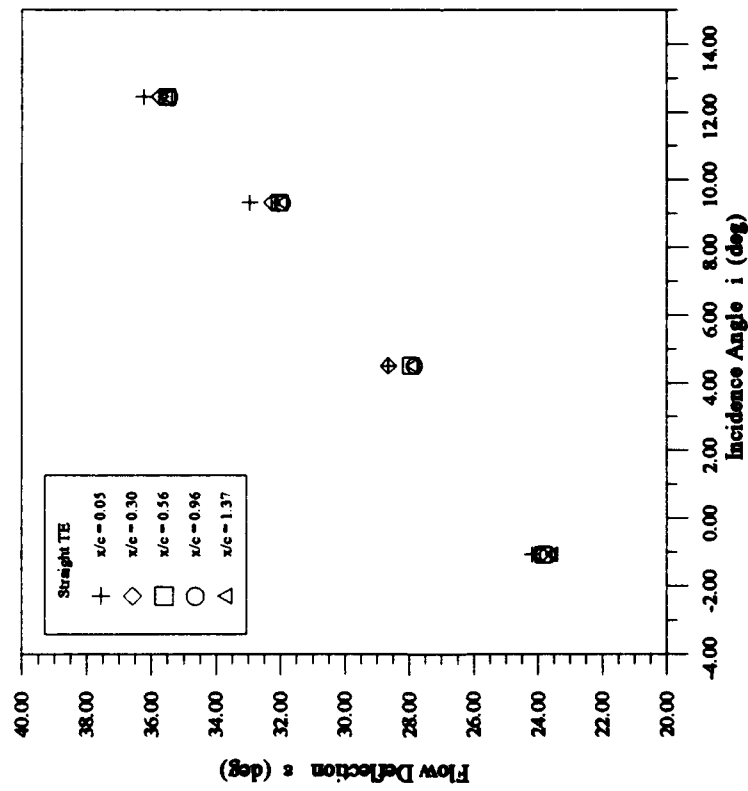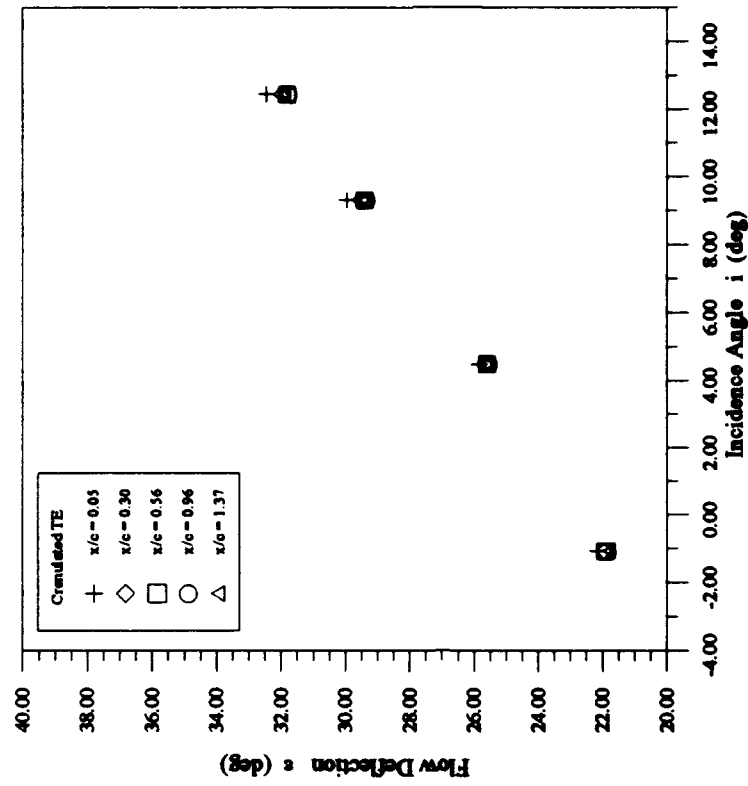
Figure 24d.

Figure 24c.

Figure 24 (cont.).   Flow Deflection (mass averaged)

91
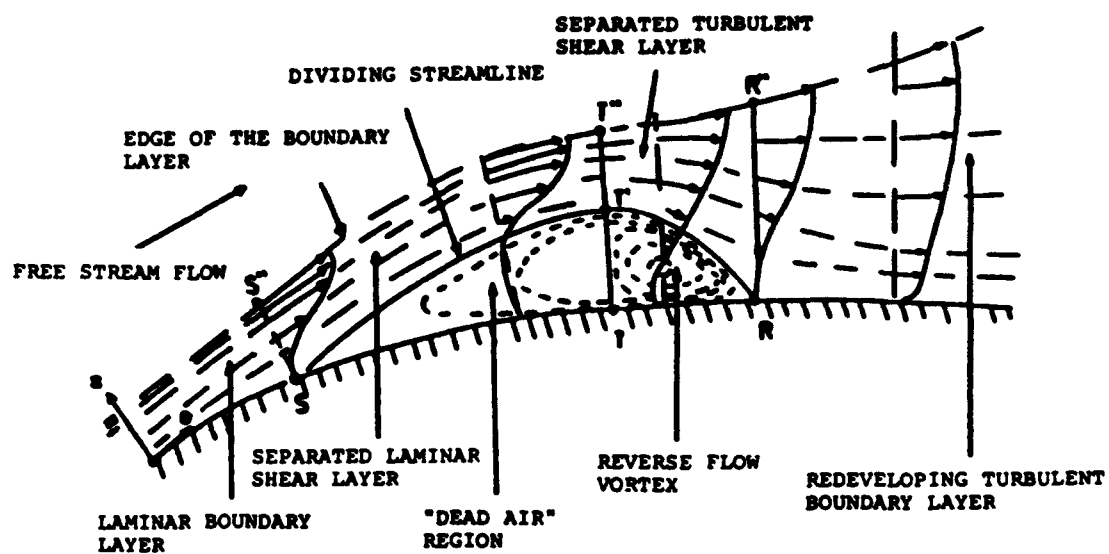
Figure 25. Transition Phenomena (Fottner, 1989)
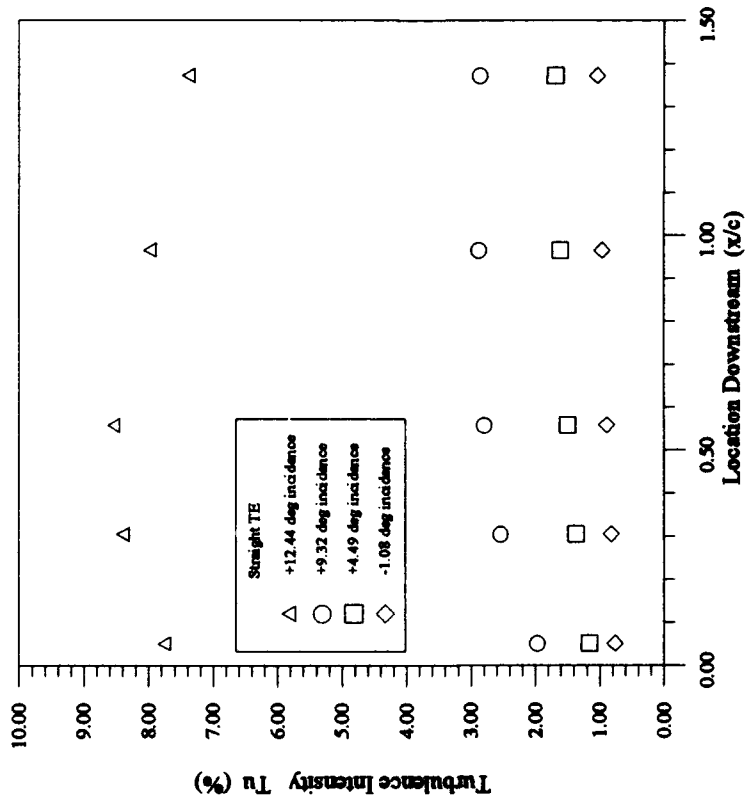
Figure 26a.
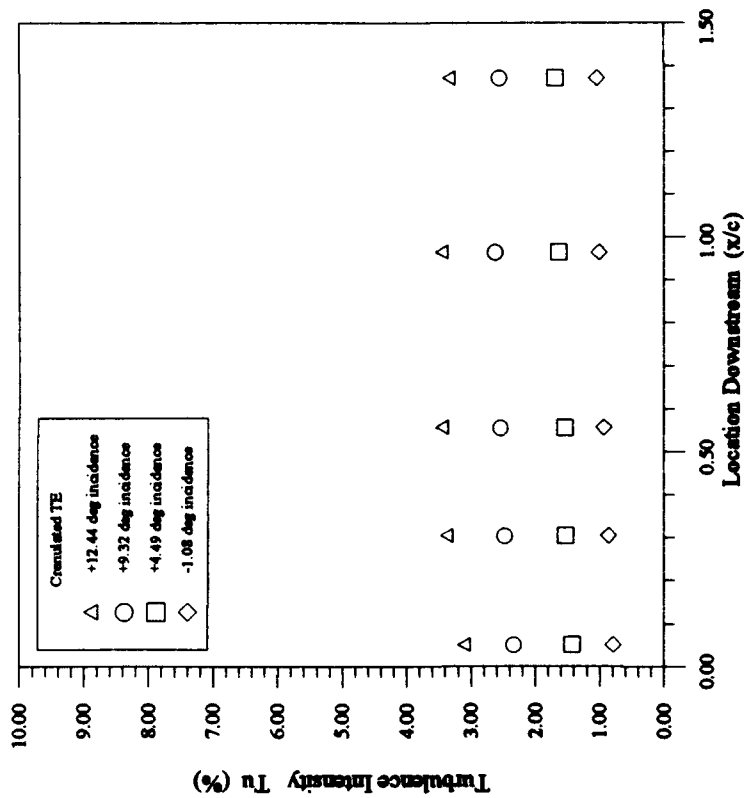
Figure 26b.

Figure 26. Outlet Turbulence Intensity (mass averaged)

93
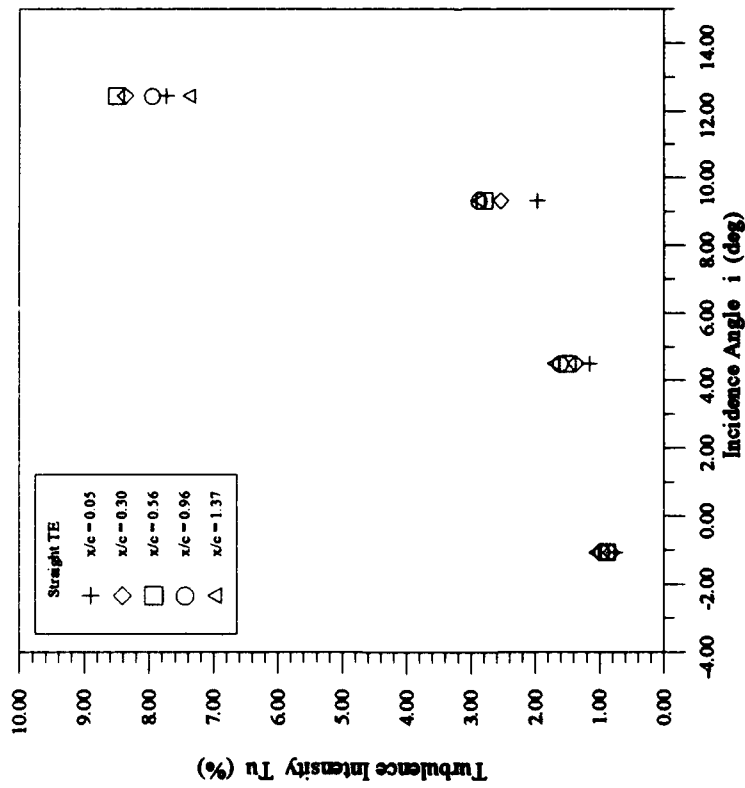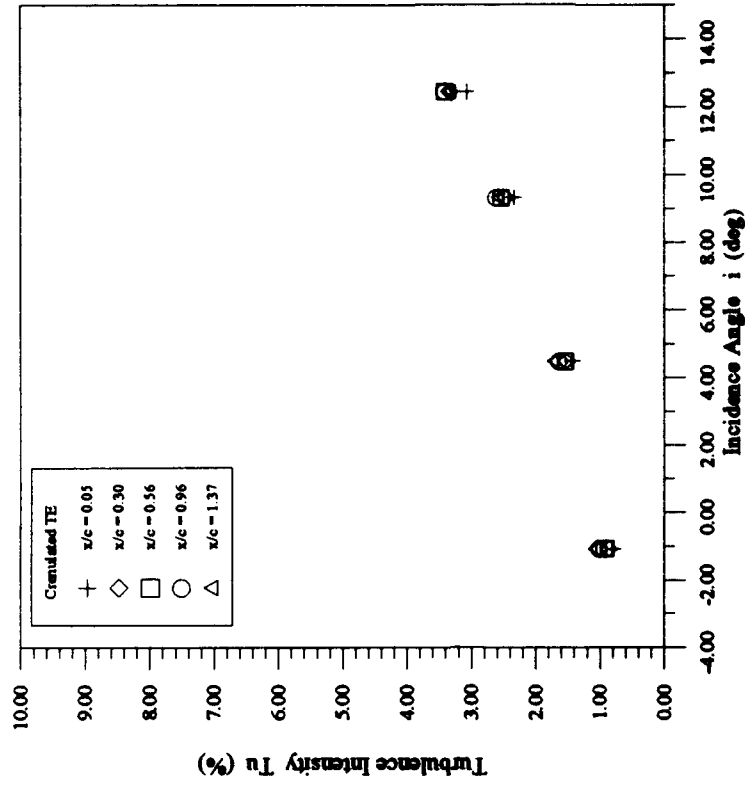
Figure 26c.

Figure 26d.

Figure 26 (cont.). Outlet Turbulence Intensity (mass averaged)
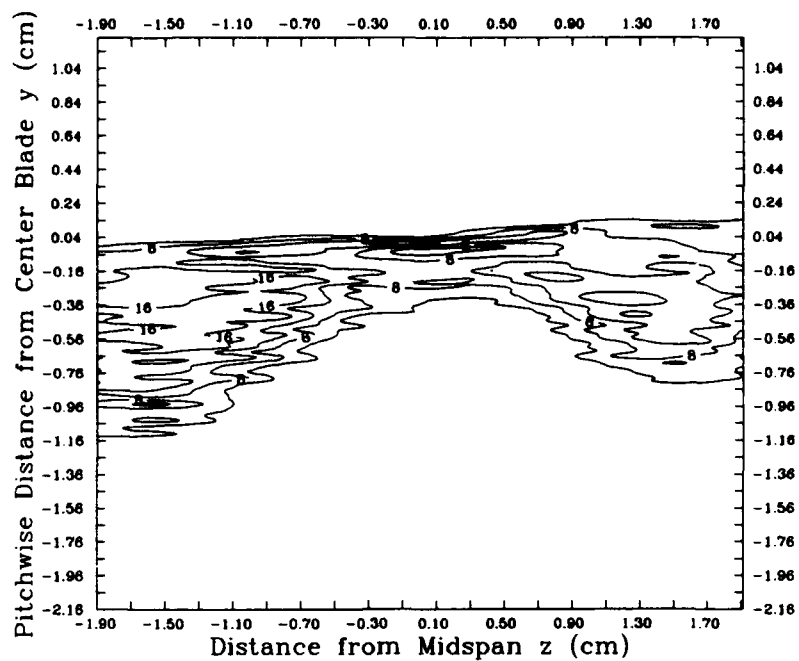
Figure 27a. Straight TE
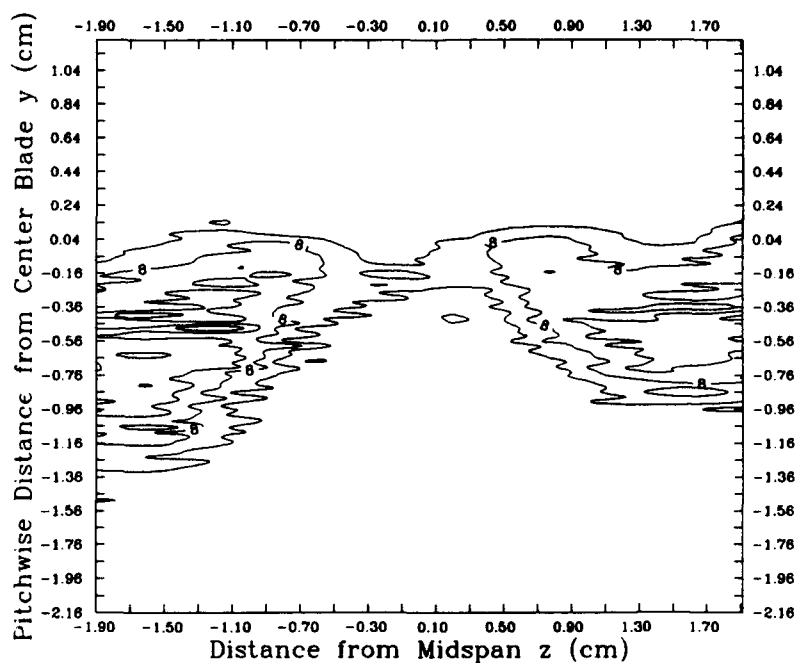
Figure 27b. Crenulated TE

Figure 27. Outlet Turbulence Intensity Distribution (%): i = +9.32 deg, x/c = 0.05
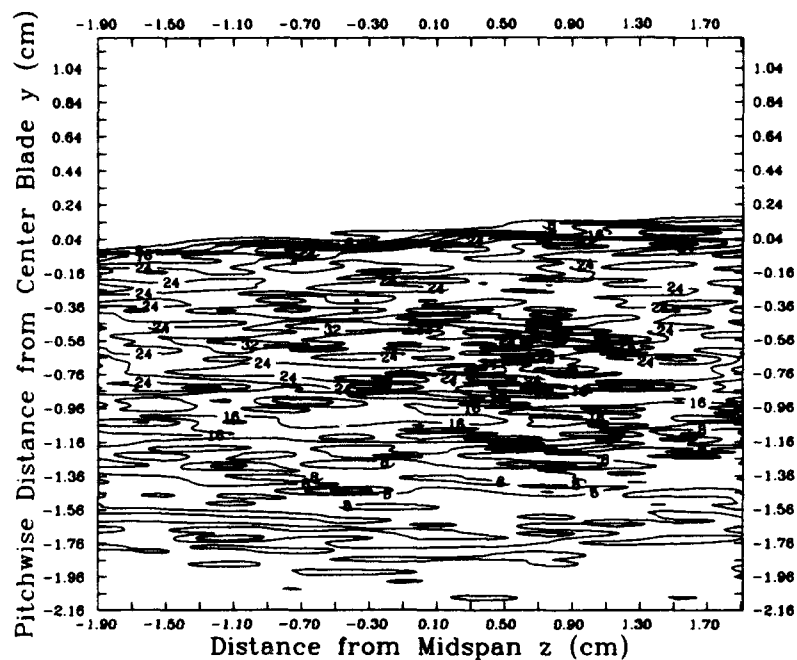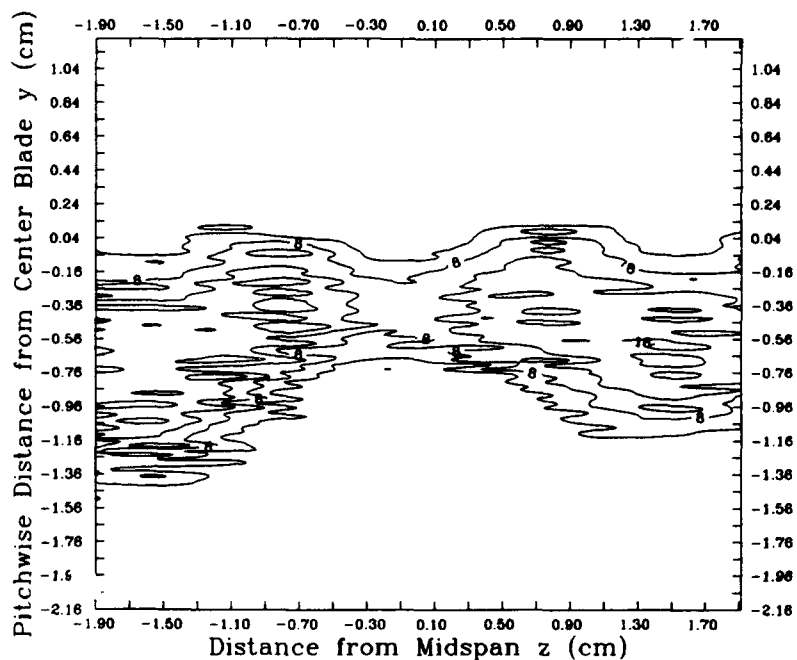
Figure 28a. Straight TE

Figure 28b. Crenulated TE

Figure 28. Outlet Turbulence Intensity Distribution (%): $i = +12.44$ deg, x/c = 0.05
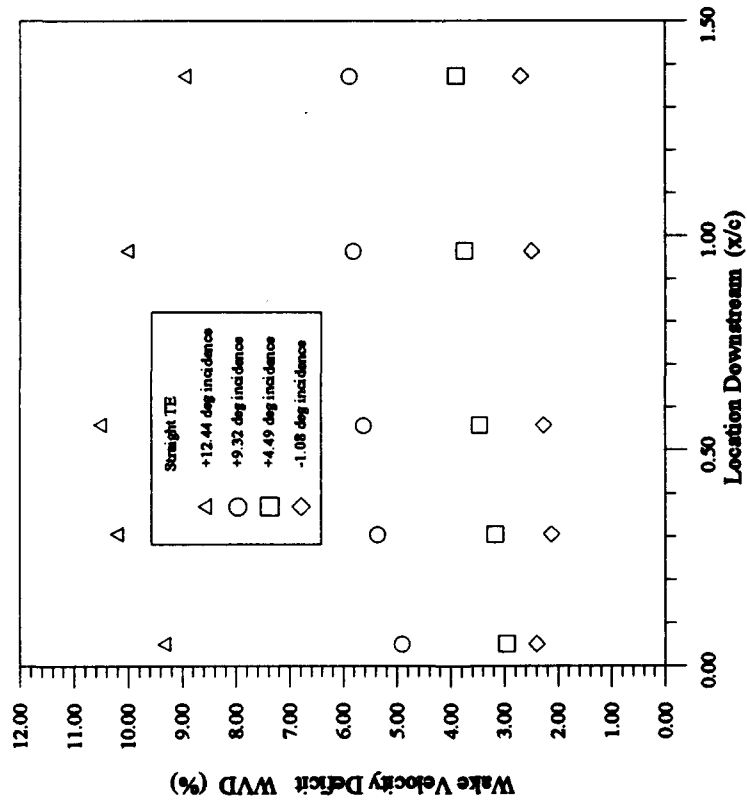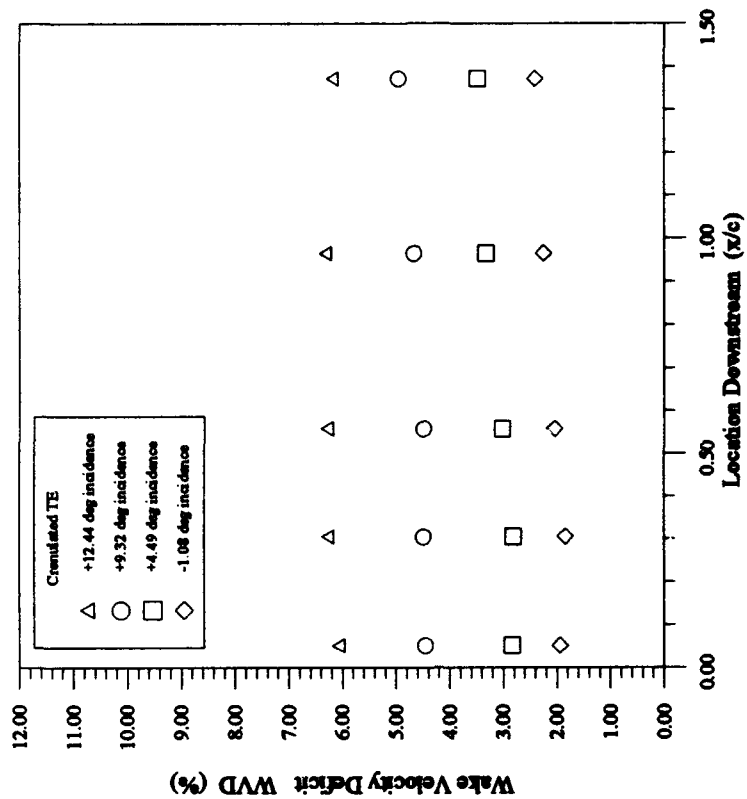
Figure 29a.

Figure 29b.

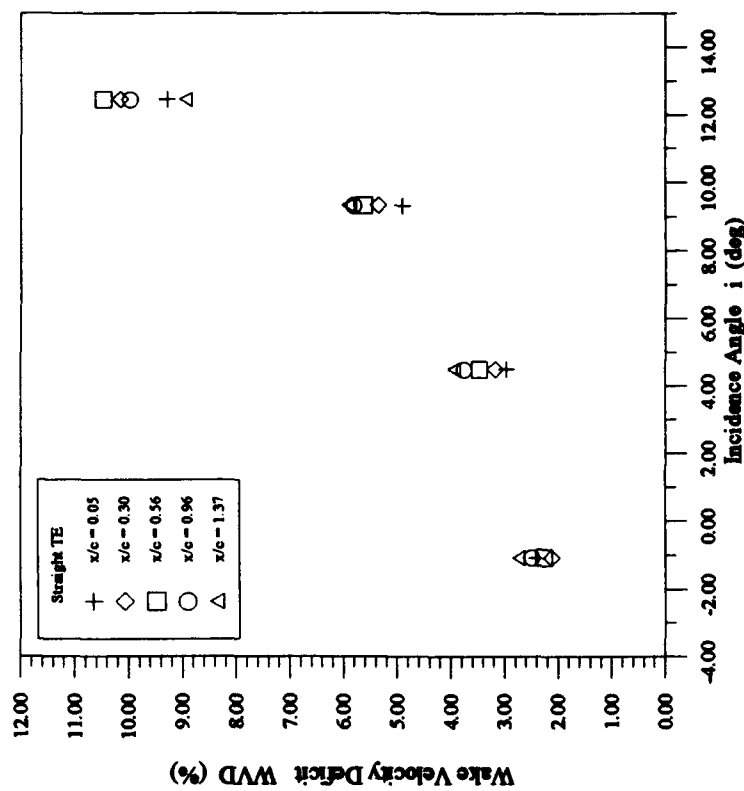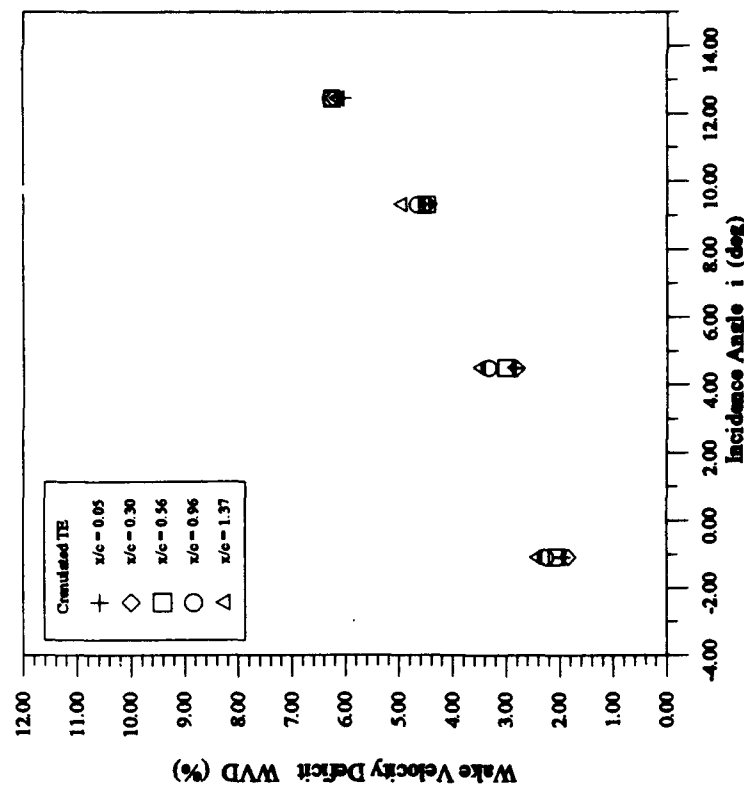Figure 29.   Wake Velocity Deficit

97

Figure 29d.

Figure 29c.
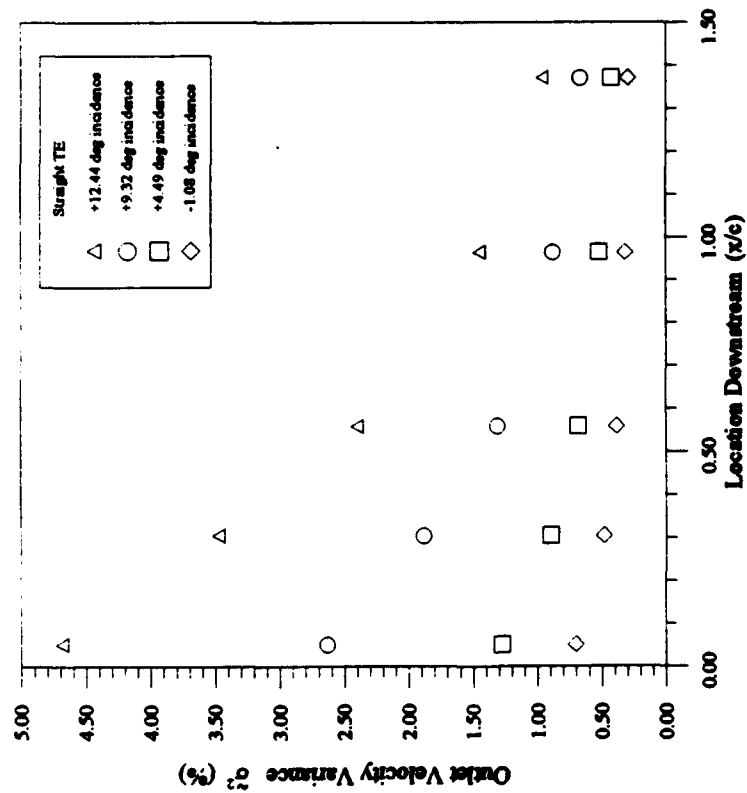
Figure 29 (cont.).   Wake Velocity Deficit
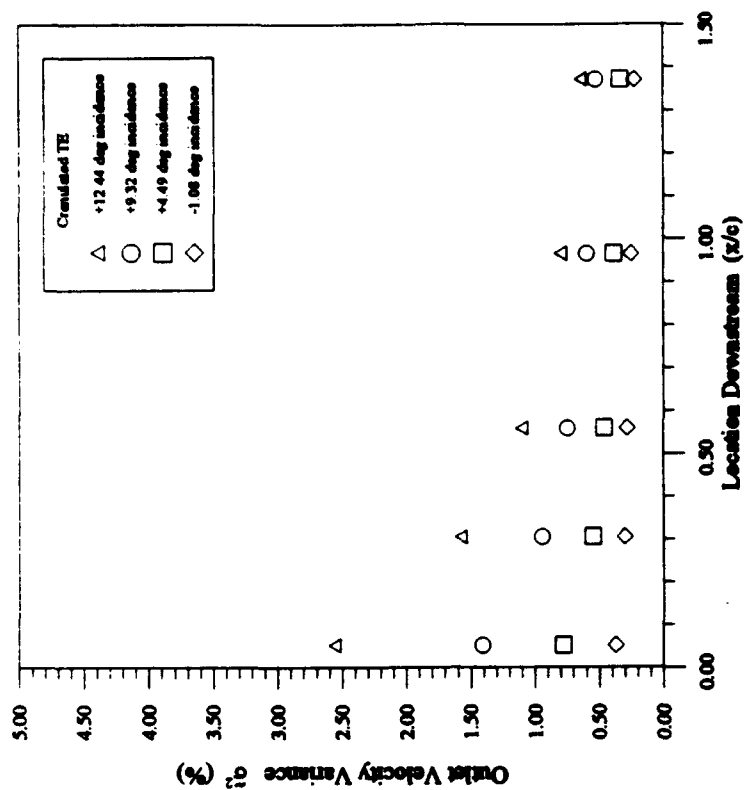
Figure 30a.

Figure 30b.

Figure 30. Outlet Velocity Variance (mass weighted)
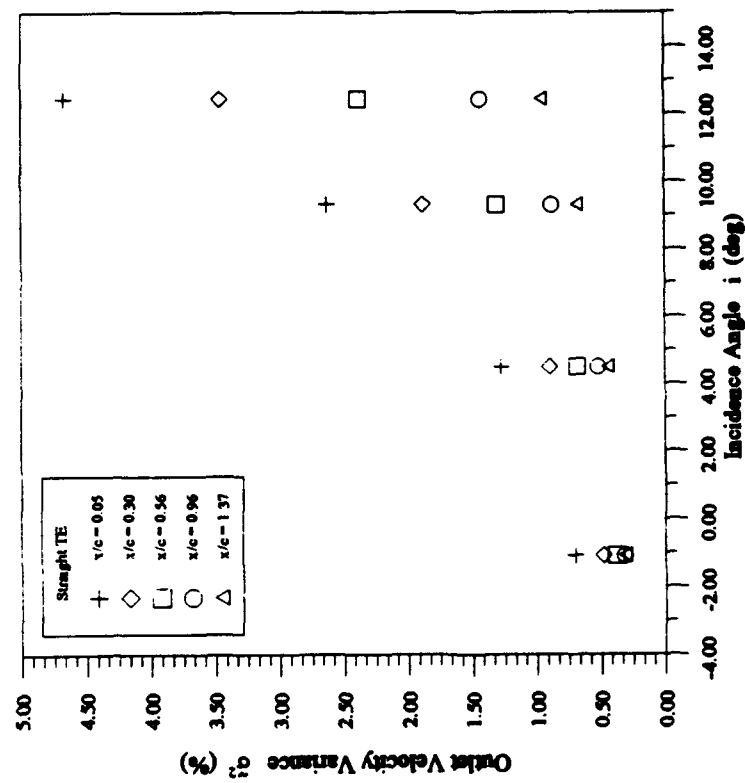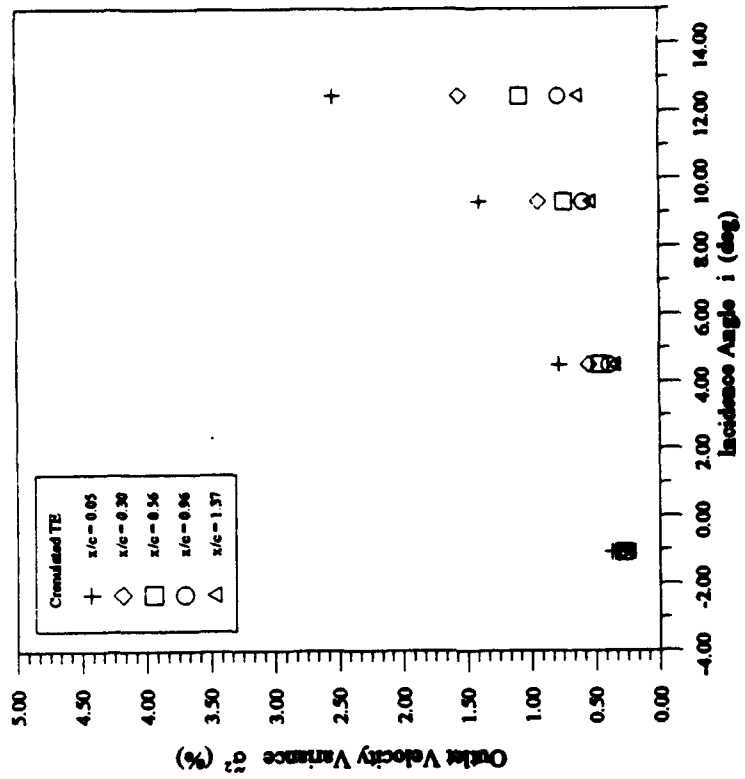
Figure 30d.

Figure 30c.

Figure 30 (cont.).   Outlet Velocity Variance (mass weighted)
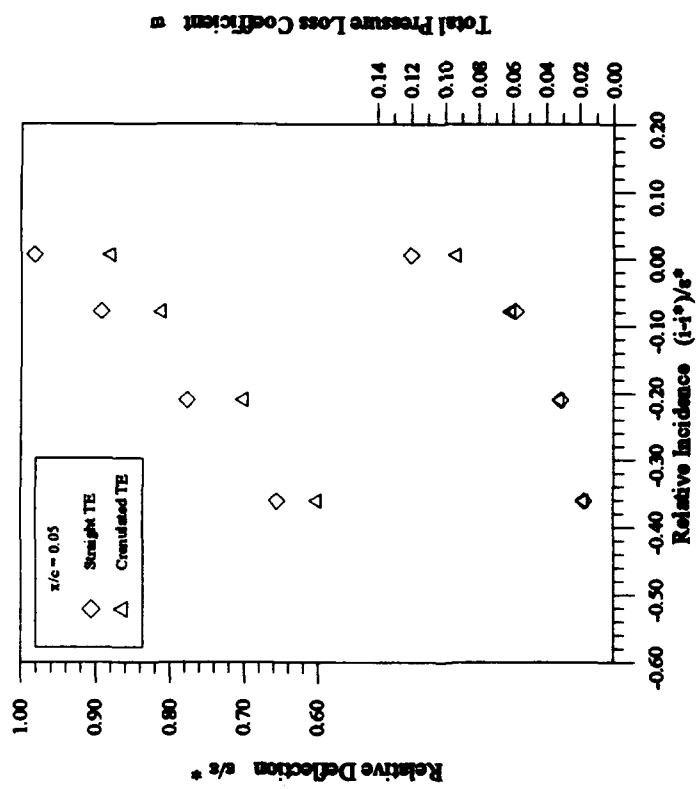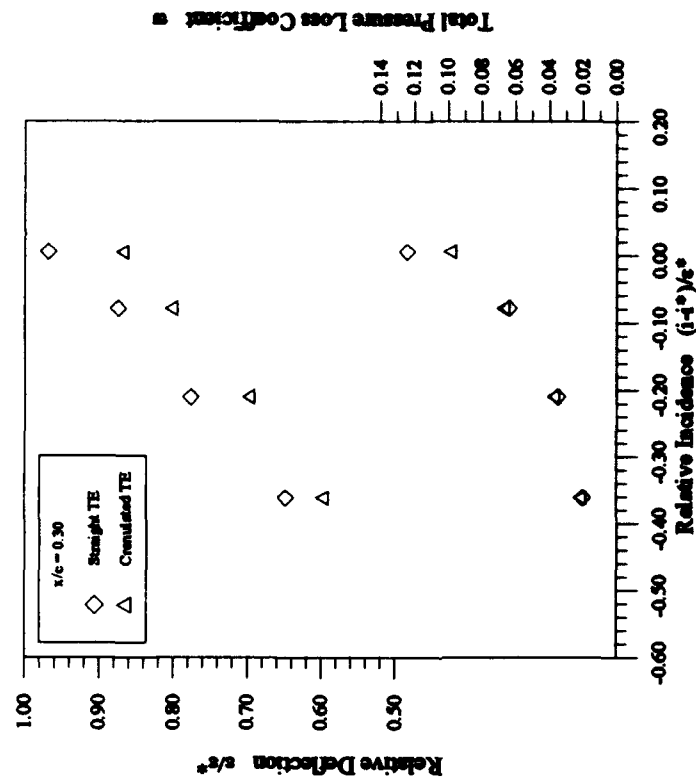
Figure 31a.

Figure 31b.

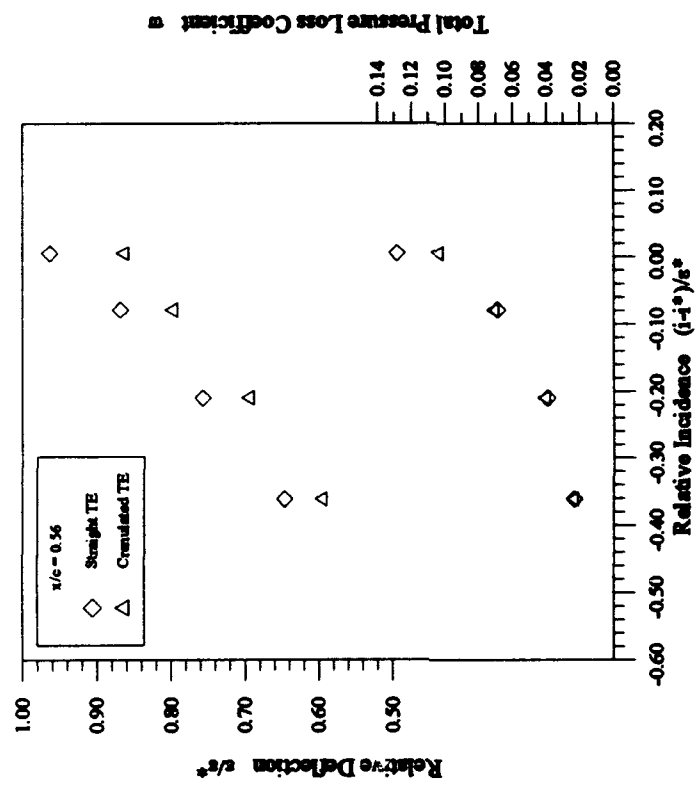Figure 31. Off-Design Performance Summary
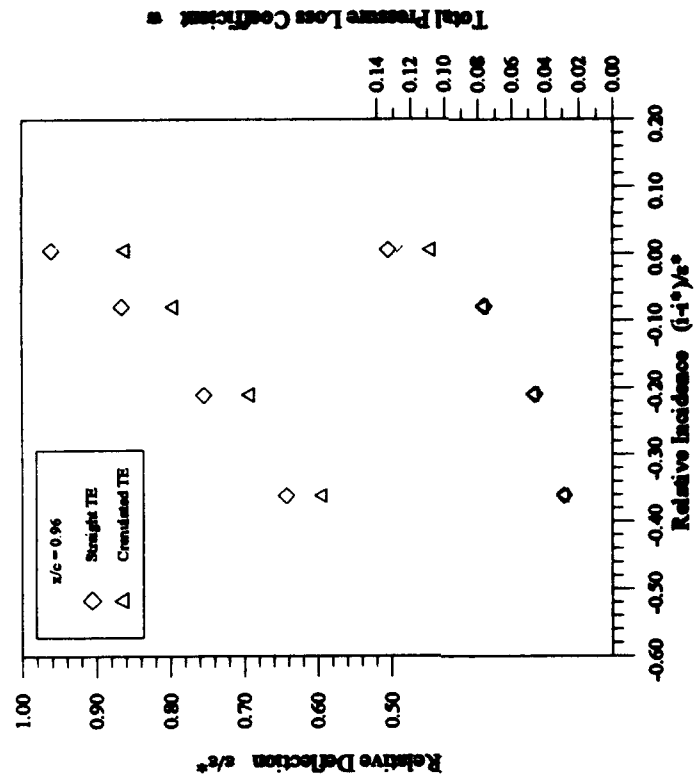
101

Figure 31c.

Figure 31d.

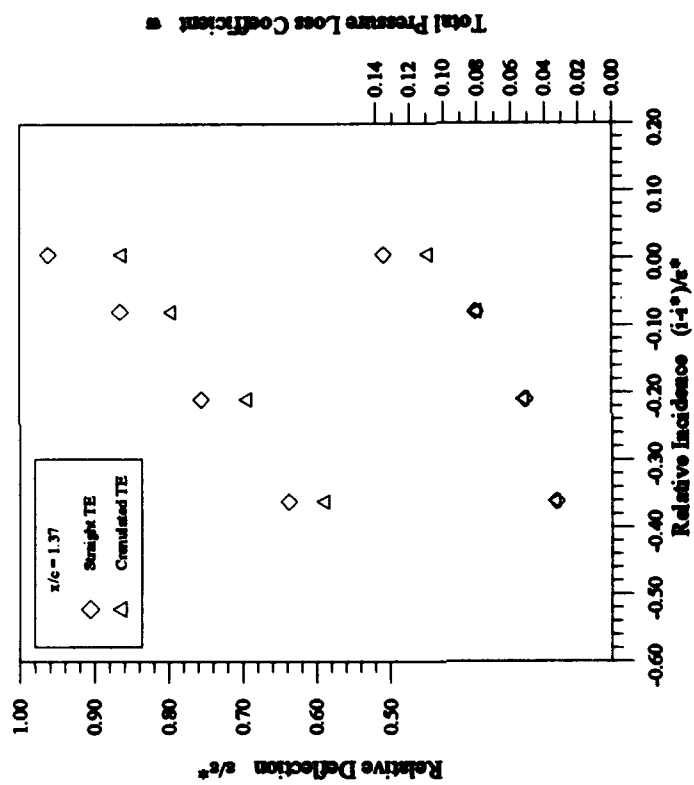Figure 31 (cont.). Off-Design Performance Summary

Figure 31e.

Figure 31 (cont.).   Off-Design Performance Summary

103

Appendix A. Determination of Blade Angles

The compressor blades used in this investigation were NACA 64-A905, a = 0.5 blades slightly modified to smooth the transition from the curved part of the suction surface to the straight tail section (reference Figure 8). The blades were locally manufactured out of aluminum using a computer-controlled milling machine programmed with the blade surface coordinates. The resulting blade was essentially a NACA 64-A905, a = 0.5 for the first 80 percent of its length. The modification to the last 20 percent of the blade caused changes in the blade angles.

The angles of interest to cascade investigations are the camber angle (θ), the blade inlet angle (α'_1), and the blade outlet angle (α'_2). These angles are shown in Figure 3. These angles are normally defined by tangents to the mean camber line at the leading and trailing edges of the blade. For NACA blades with a = 0.5, the mean camber line has infinite slope at the leading edge so the use of an alternate method was needed to determine the camber angle. The previously mentioned modification also needed to be examined to determine its impact on the angles of interest.

Several approaches were explored in the attempt to determine the blade angles. The method yielding the best results was a combination of physically measuring the slope of the training edge mean camber line on a computer generated plot of the blade profile, and approximating the blade profile with an equivalent circular arc. This method was a modification of the method outlined by Lieblein (1965) and entailed passing a circular arc through the leading edge, the trailing edge, and the point of maximum camber displaced to the mid-chord. This method was used only to determine the camber (θ) of the blade profile; it was not used to determine the other angles of interest. The use of this method to determine α'_1 led to unacceptable errors in estimating the deflection with the use of

Howell's correlation. Instead, α'_2 was measured and α'_1 was determined using the relationship

$$\alpha'_1 = \theta + \alpha'_2 \qquad (26)$$

The value of θ was determined by passing a circular arc through the leading edge, the trailing edge, and a point at the mid-chord displaced upward a distance equal to that of the maximum camber as shown in Figure 32. The coordinates for these 3 points were taken from the data file used to machine the blade. The coordinates of the these points were found to be (x, y)

Leading Edge = (0, 0)

Maximum Camber = (2.50 cm, 0.335 cm)

Trailing Edge = (5.00 cm, 0)

The equation for the circle passing through these three points was found to be

$$(x-2.50)^2 + (y+9.17)^2 \approx 90.34 \qquad (27)$$

The equation for the tangent to a circle at a point is given by Eschbach (1975) as

$$xx_1 + yy_1 + g(x+x_1) + f(y+y_1) + c = 0 \qquad (28)$$

The equation for the circle (Equation (27)) was put into the form of Equation (28) and was solved for the leading and trailing edge coordinates of the blade. The resulting angles between the respective tangents and the chord line were found to be

$$\phi_1 = 15.254 \text{ deg}$$

$$\phi_2 = -15.254 \text{ deg}$$

Which resulted in a camber angle of 30.51 deg. With this value calculated, the angle (ϕ_2) between the chord line and the mean camber line at the trailing edge was found. This angle was found by measuring it on a computer generated plot of the blade profile as shown in Figure 33. This angle was determined to be 11.5 deg. The value for α'_2 was then found using the equation

$$\alpha'_2 = \zeta - \phi_2 \tag{29}$$

The symbol ζ in Equation (29) is the stagger angle. The preceding series of computations were carried out and applied to a blade mounted in the configuration for $\alpha_1 = 31.00$ deg. The angles of interest were found to be

$$\theta = 30.51 \text{ deg}$$
$$\alpha'_2 = -4.00 \text{ deg}$$
$$\alpha'_1 = 26.51 \text{ deg}$$
$$i = 4.49 \text{ deg}$$

The accuracy of these angles was determined by using these angles in the equations for Howell's Generalized Performance Curves as outlined by Dixon (1978). This process was used to estimate the expected deflection angle for each incidence angle. In order to perform this evaluation, it was first necessary to calculate the required nominal values for deflection (ε^*) and incidence (i^*). The nominal deflection is defined as 80 percent of stall deflection and i^* is the incidence angle required to produce this deflection. These angles are defined as

$$\varepsilon^* = \alpha^*_1 - \alpha^*_2$$
$$i^* = \alpha^*_1 - \alpha'_1 \tag{30}$$

These values were computed by first finding the other nominal angles. Following Dixon (1978), these calculations were performed using

$$\alpha^*_2 - \alpha'_2 = m\theta\left(\frac{s}{c}\right)^{1/2} \tag{31}$$

$$\text{where } m = 0.23\left(2\frac{a}{c}\right)^2 + \frac{\alpha^*_2}{500} \tag{32}$$

Solving Equations (31) and (32) for α^*_2 yields

$$\alpha^*_2 = \frac{0.23\left(2\frac{a}{c}\right)^2 + \alpha'_2}{1 - \frac{\theta\left(\frac{s}{c}\right)^{1/2}}{500}} \tag{33}$$

α^*_1 was then found using

$$\alpha^*_1 = \tan^{-1}\left[\frac{1.55}{1 + 1.5\frac{s}{c}} + \tan\alpha^*_2\right] \tag{34}$$

which approximates Howell's low speed correlation and is applicable for $0 \le \alpha^*_2 \le 40$ deg. The preceding equations yielded the following nominal values:

$$\alpha^\bullet_2 = 1.86 \text{ deg}$$

$$\alpha^\bullet_1 = 38.75 \text{ deg}$$

$$\varepsilon^\bullet = 36.89 \text{ deg}$$

$$i^\bullet = 12.24 \text{ deg}$$

With the values of $i^\bullet$ and $\varepsilon^\bullet$ determined, the relative incidence is defined as

$$\text{Relative Incidence} \equiv \frac{i - i^\bullet}{\varepsilon^\bullet}$$

which was used along with Howell's Generalized Performance Curves to yield the relative deflection which is defined as

$$\text{Relative Deflection} \equiv \frac{\varepsilon}{\varepsilon^\bullet}$$

The deflection angles for the four incidence angles were estimated using the above definitions and Howell's Generalized Performance Curves. These were found to correlate fairly well with the measured deflection angles produced by the straight trailing edge blades. The results are summarized in Table 12.

Table 12. Measured and Predicted Flow Deflection Angles

α_1 (deg)	i (deg)	Measured ε (deg)	Predicted ε (deg)
25.43	-1.08	23.52	24.81
31.00	+4.49	27.86	30.31
35.83	+9.32	31.92	34.62
38.95	+12.44	35.49	37.40

It is important to note that Howell's correlation was intended to be applied to two dimensional flow while the cascade used in this study had strong three-dimensional effects. Considering this, differences ranging from 1.7 to 2.5 deg represented a reasonably good correlation between the measured and predicted values of deflection.
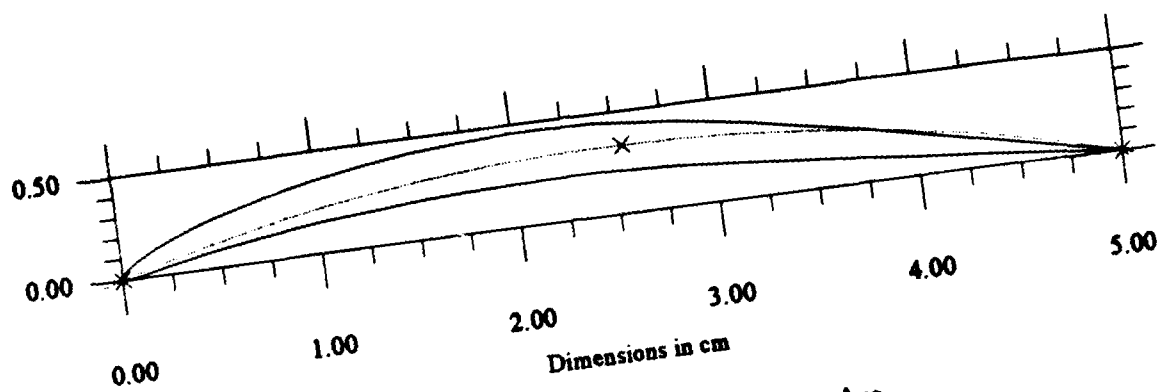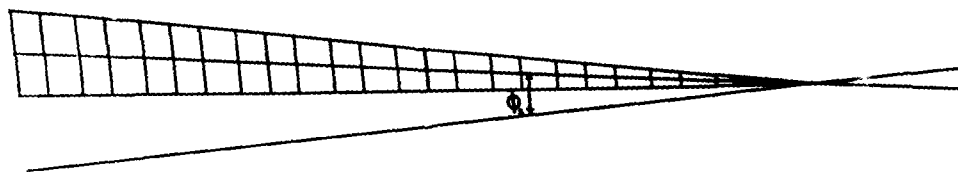
Figure 32. Blade Profile with Circular Arc

Figure 33. Tail Section of Blade Profile

110

Appendix B.   Equipment Listing

Subsystem

Model Number/Description

Pressure Measurement

Pressure Systems Inc. Model 8400 Pressure
  Scanner (20 kHz maximum sample rate)
    Model 8415 Scanner Interface Unit
    Model 8420 Scanner Digitizer Unit
    Model 8440 Analog Input Unit
    Model 8433 1 psid Pressure Calibration Unit
    Model 8433 5 psid Pressure Calibration Unit
    Certified Standard Transducer (0.2-18 psi
      range, ±0.00001 psi accuracy)

Transducer block P/N 32RG-0301
  (±1 psid range, ±0.0005 psi accuracy)

Transducer block P/N 3201B
  (±1 psid range, ±0.0005 psi accuracy)

Transducer block P/N 3205B
  (±5 psid range, ±0.0005 psi accuracy)

Pressure Rake (11 ports, spaced 0.381 cm,
  0.0635 cm ID, 0.0889 cm OD)

CEC Model 2500 Digital Barometer
  (13.00 psia - 15.51 psia range, ±0.005 psi
  accuracy)

Velocity and Temperature Measurement

TSI Model IFA 100 System Intelligent Flow
  Analyzer
    Model 140 Temperature Module
    Model 150 Anemometer Modules (2)
    Model 157 Signal Conditioner Module (3)

TSI Model IFA 200 System Multichannel
  Digitizer
    Model 252 Digitizers (3) (50 kHz maximum
      sample rate, ±5 V range, ±0.002 V
      accuracy)

Subsystem	Model Number/Description
Velocity and Temperature Measurement	TSI Model 1241-10 X-Film Sensor
	TSI Model 1241-20 X-Film Sensor
	TSI Model 1155-36 probe support (modified length to 24")
	TSI Model 1125 Probe Calibrator
	Omega T-type Thermocouple (copper-constantan, ±0.3°C accuracy)
Temperature Measurement	Hewlett-Packard Model 3455A Digital Voltmeter (±0.00002 V accuracy, 24 Hz maximum sample rate)
	Hewlett-Packard Model 3495A Scanner
	Omega T-type Thermocouples (2) (copper-constantan, ±0.3°C accuracy)
Traverse Control	New England Affiliated Technologies Model 310 Programmable Motion Controllers (2)
	Oriental Motor Company Stepper Motors (2) (400 steps/revolution resolution)
Central Computer	Zenith Model Z-248 (80286 processor with math coprocessor) National Instruments Model GPIB-PCII General Purpose Interface Board) TSI Model 6260 Parallel Interface Board
	Software (developed by AFIT/ENY, written in MS-QuickBasic 4.5)

Appendix C: Error Analysis

The equipment accuracies specified by the manufacturer or determined during calibration procedures are summarized in Table 13. These values are used in the following analysis to estimate the expected error for each of the calculated parameters. The method for determining the errors is demonstrated by example for the pressure loss coefficient. The errors for the other quantities are calculated in a similar manner.

Total Pressure Loss Coefficient

The error for ϖ was estimated by evaluating Equation (4) for a given set of data taken from an actual test run. The equation was then re-evaluated for the same data changed by the accuracy of the instrumentation used to measure each quantity. The instrument accuracies were either added to the measured reading or subtracted from it so as to create the largest error in the final answer. Once these calculations were made, the percent change in the final answer was calculated using

$$ERROR = \frac{\varpi + \varepsilon}{\varpi} - 1$$

where ε is the net error due to component accuracies. If this error is assumed to occur in the same direction at every point of the measurement plane, the largest error will be found in the mass averaging summation. This is a valid assumption since the quantity in the numerator of Equation (4) is a difference in pressures and does not vary much in relation to the size of the error associated with the pressure transducers. The quantities in the denominator, on the other hand, are all throat conditions and do not vary much over the period of the data run. These calculations resulted in an estimated error due to equipment

capabilities of 2 percent for ϖ. The errors that might be introduced by the density and velocity terms in the mass averaging process were found to be largely offsetting and assumed to be negligible.

Static Pressure Coefficient

An analysis of the equations for C_p revealed that the error would be the same as for ϖ. This is because the quantities in the numerator, of Equation (3), are again a difference in pressures that are of the same order of magnitude as for ϖ. The quantities in the denominator, on the other hand, are exactly the same as those for ϖ. This applies to both the blade surface static pressure distribution and the non-dimensional static pressure rise.

Wake Velocity Deficit

The wake velocity deficit error was calculated by determining the appropriate error for the two velocities in Equation (8). The velocity in the denominator is an arithmetic mean value and the velocity in the numerator is a mass averaged value. The velocities used to compute the freestream velocity were also used to compute the downstream axial velocity. These two facts make it impossible for the numerator to be in error in one direction (i.e., high or low) and the denominator to be in error in the opposite direction. Additional insight was gained when the nature of the error introduced by the hot-film probe was examined. The majority of the samples taken were at a negative angle and the errors found in the calibration process were all in the same direction for negative angles. From these two facts, it was determined that the errors should be in the same direction for both the numerator and denominator. The expected error was determined by adding 0.5 m/s to representative values for both of these. The representative values were taken from actual data runs and were 113 m/s for downstream axial velocity and 120 m/s for the

114

freestream velocity. These values resulted in an estimated error of 3 percent for values representative of those measured in the cascade.

Outlet Velocity Variance

The outlet velocity variance is similar to the wake velocity deficit but more complicated. If the mass averaging process is ignored, the quantity to be analyzed is

$$\sum_{j=1}^{n}\left(\frac{V_{2_j}}{\overline{V_2}}-1\right)^2$$

In this case it is possible to have a local exit velocity with a -0.5 m/s error while the mean exit velocity has a total error near +0.5 m/s. Since most of the local values must be near +0.5 m/s for the mean error to be +0.5 m/s, the errors are much more likely to be in the same direction by nearly the same amount once the summation process is completed. For error estimation purposes, an error value of 0.5 m/s was added to the representative values of the numerator and denominator. The values used for this evaluation were a mean velocity of 116 m/s and an individual value of 99 m/s which was one standard deviation below the mean value. This method resulted in an estimated error of 1 percent for the outlet velocity variance.

Outlet Turbulence Intensity

An analysis of the equation for Tu revealed that the error would be the same as for the outlet velocity variance. This is because both have individual velocities in the numerator of their respective equations and mean velocities in the denominator. Therefore the error for Tu was estimated to be 1 percent.

Axial Velocity Density Ratio

The basic approach to estimating the error in the *AVDR* was essentially the same as that followed for the other parameters. Equation (2) was evaluated term by term. In this case, the velocity in the denominator was calculated from upstream quantities. These quantities should have identical errors for each data point since the same instrument was used, in virtually the same conditions, to measure the quantities. This evaluation applies equally well to the densities. The errors for these values were calculated in the same way as those for the ϖ discussed above. The velocity in the numerator was evaluated in a manner similar to the outlet velocity variance and wake velocity deficit discussed above. In this case, since there is less vorticity at the center span for all configurations, virtually all of the velocities were taken at similar flow angles. When representative values were used for each quantity and then perturbed by the appropriate error, the resulting overall error was calculated to be 1 percent.

Table 13. Component Accuracies

Component	Accuracy
Pressure Transducers	0.0005 psid
Digital Barometer	0.005 psia
Thermocouples	0.3°C (meas)
Hot-film Velocity	0.5 m/s (meas)
Hot-film Angles	0.25 deg (meas)

Vita

Captain Michael John Costello was born on 30 January 1967 in Schenectady, New York. He graduated from Mohonasen High School, Schenectady, New York in 1985. In 1989, he earned a Bachelor of Science in Mechanical Engineering from Virginia Polytechnic Institute and State University and was commissioned a Second Lieutenant in the United States Air Force.

His initial active duty assignment was at the Ballistic Missile Organization, Norton AFB, CA where he managed the development of basing equipment for the Peacekeeper Rail Garrison ICBM Program. Captain Costello was assigned to the Air Force Institute of Technology, Wright-Patterson AFB, OH in 1992 to pursue a Master of Science in Aeronautical Engineering.

Permanent Address: 1184 Outer Drive
                      Schenectady, NY 12303

REPORT DOCUMENTATION PAGE

Public reporting burden for this collection of information is estimated to average 1 hour per response, including the time for reviewing instructions, searching existing data sources, gathering and maintaining the data needed, and completing and reviewing the collection of information. Send comments regarding this burden estimate or any other aspect of this collection of information, including suggestions for reducing this burden, to Washington Headquarters Services, Directorate for Information Operations and Reports, 1215 Jefferson Davis Highway, Suite 1204, Arlington, VA 22202-4302, and to the Office of Management and Budget, Paperwork Reduction Project (0704-0188), Washington, DC 20503.

1. AGENCY USE ONLY (Leave blank)	2. REPORT DATE 1 December 1993	3. REPORT TYPE AND DATES COVERED Final Master's Thesis

4. TITLE AND SUBTITLE

Off-Design Performance of Crenulated
Blades in a Linear Compressor Cascade

5. FUNDING NUMBERS

6. AUTHOR(S)

Michael J. Costello

7. PERFORMING ORGANIZATION NAME(S) AND ADDRESS(ES)

Air Force Institute of Technology, WPAFB, OH 45433-6583

8. PERFORMING ORGANIZATION REPORT NUMBER

AFIT/GAE/ENY/93D-9

9. SPONSORING / MONITORING AGENCY NAME(S) AND ADDRESS(ES)

10. SPONSORING / MONITORING AGENCY REPORT NUMBER

11. SUPPLEMENTARY NOTES

12a. DISTRIBUTION / AVAILABILITY STATEMENT

Approved for public release; distribution unlimited

12b. DISTRIBUTION CODE

13. ABSTRACT (Maximum 200 words)

The effects of using compressor blades with a crenulated (notched) trailing edge in a low aspect ratio ($AR = 1$) linear compressor cascade at four incidence angles (-1.08 deg, +4.49 deg, +9.32 deg, and +12.44 deg) were investigated. Blade performance and wake mixing characteristics for crenulated blades were compared with similar data for blades with a straight trailing edge. A seven-bladed cascade was operated with a flow Mach number of 0.4 and a blade chord Reynolds number of $4.1 (10)^5$. The diffusion factor ranged from 0.22 to 0.42 and strong three-dimensional flow effects were present. Total pressure losses were measured with a total pressure rake. Velocities and flow angles were measured using hot-film anemometry. Crenulated blades were found to enhance wake mixing from 20 to 50 percent depending on blade loading and downstream location. Crenulated blades were also found to reduce flow deflection by 1.9 deg at the lowest incidence and by 3.7 deg at the highest incidence. At the highest blade loading, crenulations were found to reduce total pressure losses by 20 percent and inhibit large scale flow degradation and vortex breakdown. At mild blade loadings, negligible differences in losses were observed.

14. SUBJECT TERMS
axial flow compressor blades, cascades, crenulations, secondary flow, vortices, trailing edges, airfoil, wake

15. NUMBER OF PAGES
131

16. PRICE CODE

17. SECURITY CLASSIFICATION OF REPORT Unclassified	18. SECURITY CLASSIFICATION OF THIS PAGE Unclassified	19. SECURITY CLASSIFICATION OF ABSTRACT Unclassified	20. LIMITATION OF ABSTRACT UL